

UNIVERSIDADE TECNOLÓGICA FEDERAL DO PARANÁ  
GRADUATE PROGRAM IN ELECTRICAL ENGINEERING

MARCO TÚLIO LOPES GUERREIRO

**FREQUENCY-DOMAIN ALGORITHMS FOR ULTRASONIC  
IMAGING BASED ON INTERPOLATION-FREE STOLT  
MIGRATION**

DISSERTATION

**PATO BRANCO  
2020**

MARCO TÚLIO LOPES GUERREIRO

**FREQUENCY-DOMAIN ALGORITHMS FOR ULTRASONIC  
IMAGING BASED ON INTERPOLATION-FREE STOLT  
MIGRATION**

Dissertation presented to the Graduate Program in Electrical Engineering at Universidade Tecnológica Federal do Paraná *Campus* Pato Branco as a partial requirement to obtain the “Master of Science” degree in Electrical Engineering.

Supervisor: Prof. Dr. Giovanni Alfredo Guarneri

**PATO BRANCO  
2020**

G934f Guerreiro, Marco Túlio Lopes.  
Frquency-domain algorithms for ultrasonic imaging based on  
interpolation-free stold migration / Marco Túlio Lopes Guerreiro. -- 2020.  
107 f. : il.

Orientador: Prof. Dr. Giovanni Alfredo Guarneri  
Dissertação (Mestrado) - Universidade Tecnológica Federal do Paraná.  
Programa de Pós-Graduação em Engenharia Elétrica. Pato Branco, PR,  
2020.

Inclui bibliografia.

1. Testes não-destrutivos. 2. Testes de ultrasson. 3. Processamento de  
imagens. 4. Interpolação. 5. Fourier, Transformadas de. I. Guarneri,  
Giovanni Alfredo. II. Universidade Tecnológica Federal do Paraná.  
Programa de Pós-Graduação em Engenharia Elétrica. III. Título.

CDD 22. ed. 621.3

Ficha Catalográfica elaborada por  
Suélem Belmudes Cardoso CRB9/1630  
Biblioteca da UTFPR Campus Pato Branco



---

## TERMO DE APROVAÇÃO

Título da Dissertação n.º 86

**“Frequency-Domain Algorithms for Ultrasonic Imaging Based on Interpolation-Free Stolt Migration”**

por

**Marco Túlio Lopes Guerreiro**

Dissertação apresentada - na modalidade remota – como medida à prevenção a Pandemia COVID-19 - às quinze horas, do dia 10 de julho de dois mil e vinte, como requisito parcial para obtenção do título de **MESTRE EM ENGENHARIA ELÉTRICA**. Programa de Pós-Graduação em Engenharia Elétrica, Universidade Tecnológica Federal do Paraná, Câmpus Pato Branco. O candidato foi arguido pela Banca Examinadora composta pelos professores abaixo assinados. Após deliberação, a Banca Examinadora considerou o trabalho APROVADO.

Banca examinadora:

---

**Prof. Dr. Giovanni Alfredo Guarneri**  
(Orientador)  
UTFPR/PB

---

**Prof. Dr. Dalcimar Casanova**  
UTFPR/PB

---

**Prof. Dr. Daniel Rodrigues Pipa**  
UTFPR/CT

---

**Prof. Dr. Marcelo Victor Wust Zibetti**  
New York University (Langone Health) -  
Membro Externo

Homologado por:

---

**Prof. Dr. Gustavo Weber Denardin**  
Coordenador do Programa de Pós-Graduação em  
Engenharia Elétrica - PPGEE/UTFPR

## AGRADECIMENTOS

Esse trabalho não poderia ter sido concluído sem a orientação do Prof. Giovanni Guarneri. O Prof. Giovanni nunca mediu esforços para orientar e sempre foi uma fonte de motivação nos momentos difíceis. Sou grato por toda as discussões e pela oportunidade de poder participar nesse projeto em conjunto com a UTFPR em Curitiba. Também agradeço o Prof. Giovanni e o Prof. Daniel Pipa pela oportunidade de poder participar do projeto e fornecer os meios financeiros para isso. Sou grato também pelos órgãos e instituições que fomentam o desenvolvimento da educação e pesquisa no Brasil, como a UTFPR, o PPGEE, a Petrobras, a CAPES, o CNPq, a Fundação Araucária e muitos outros. Gostaria também de agradecer a Silmara por sempre estar disposta a ajudar e esclarecer dúvidas sobre requerimentos e formulários do PPGEE.

Tanto na qualificação quanto na defesa final, a banca examinadora contribuiu com comentários e sugestões muito valiosas, que contribuíram de forma significativa para esse trabalho. Dessa forma, gostaria de agradecer ao Prof. Dalcimar Casanova, Prof. Daniel Pipa e Prof. Marcelo Zibetti, por terem participado da banca e revisado o trabalho.

Agradeço também aos colegas do Campus de Curitiba: Vitor, Hector, Tatiana e Prof. Thiago. Agradeço especialmente o Vitor e o Hector, por sempre estarem a disposição para ajudar, realizar experimentos e esclarecer dúvidas.

O ambiente de trabalho aqui no Campus de Pato Branco favoreceu muito o desenvolvimento do trabalho; por isso, gostaria de agradecer aos colegas e amigos que passaram pelo laboratório daqui: Andréa, Tatiana, Andréia e César. Em especial, agradeço a Andréa, que se tornou uma grande amiga e sempre esteve disposta a ajudar, além de compartilhar comidas a tarde, momentos de descontração, risadas e apoio em momentos difíceis.

Gostaria de agradecer, também, aos meus grandes amigos Yascara, Augusto, Marlon, Raphael e Isadora que sempre me apoiaram durante o desenvolvimento deste trabalho e sempre forneceram momentos de descontração e apoio.

Por fim, nada disso seria possível se não fosse por todo o apoio que tive da minha família. Tenho uma enorme e eterna gratidão à todos da minha família, em especial à minha mãe, Aneli, meu pai, Marco, minhas irmãs Laura e Rafaela, minhas tias Izaura, Laura e Adriana, meus tios Adauto e Ralph e meus avós, Lola, Natália e Alencar. Todos tiveram uma grande contribuição para o meu desenvolvimento pessoal e acadêmico e por isso, sou eternamente grato.

## ABSTRACT

GUERREIRO, Marco T. L.. FREQUENCY-DOMAIN ALGORITHMS FOR ULTRASONIC IMAGING BASED ON INTERPOLATION-FREE STOLT MIGRATION. 108 f. Dissertation – Graduate Program in Electrical Engineering, Universidade Tecnológica Federal do Paraná. Pato Branco, 2020.

A class of algorithms for the post-processing of ultrasonic data in the frequency-domain are based on Stolt's migration, which requires sampling the spectral data at non-uniformly spaced frequency points. Usually, the resampling of the frequency-domain data is obtained by using an oversampled Fast Fourier Transform and piecewise linear interpolation of the resulting frequency spectrum. This study proposes the use of frequency shifts to replace the interpolation step required by Stolt's migration. An algorithm from synthetic aperture radar using the frequency shifting method is adapted and extended to ultrasonic imaging with frequency-domain algorithms. The proposed method is evaluated with experimental data, and it is demonstrated that migration by frequency shifts can present advantages over piecewise linear interpolation. In terms of reconstruction quality, algorithms using frequency shifts can achieve contrast-to-noise ratio similar to or superior than algorithms using piecewise linear interpolation. The computational load of algorithms using frequency shifts and piecewise linear interpolation is evaluated and algorithms using frequency shifts show at least a 1.5 times reduction in execution time, when the height of the imaging region under 30 mm. In addition, compared to piecewise linear interpolation, algorithms using frequency shifts presents advantages in CNR and execution time when the reconstructed image contains the bottom of the object.

**Keywords:** Nondestructive testing, Ultrasonic imaging, Stolt's migration, Oversampled FFT, Interpolation

## RESUMO

GUERREIRO, Marco T. L.. FREQUENCY-DOMAIN ALGORITHMS FOR ULTRASONIC IMAGING BASED ON INTERPOLATION-FREE STOLT MIGRATION. 108 f. Dissertation – Graduate Program in Electrical Engineering, Universidade Tecnológica Federal do Paraná. Pato Branco, 2020.

Uma classe de algoritmos para o pós-processamento de dados ultrassônicos no domínio da frequência são baseados na migração de Stolt, que requer a amostragem dos dados do espectro em pontos de frequência espaçados não-uniformemente. Geralmente, a reamostragem dos dados do domínio da frequência é obtida com o uso de uma Transformada Rápida de Fourier sobreamostrada e interpolação linear por partes do espectro resultante. Este estudo propõe o uso de deslocamentos de frequência para substituir o passo de interpolação necessário pela migração de Stolt. Um algoritmo de radar de abertura sintética que utiliza o método de deslocamentos de frequência é adaptado e estendido para imageamento ultrassônico com algoritmos do domínio da frequência. O método proposto é avaliado com dados experimentais, e é demonstrado que migração por deslocamentos de frequência pode apresentar vantagens em relação a interpolação linear por partes. Em termos de qualidade de reconstrução, algoritmos utilizando deslocamentos de frequência podem atingir relação contraste-ruído similar ou superior a algoritmos utilizando interpolação linear por partes. A carga computacional de algoritmos utilizando deslocamentos de frequência e interpolação linear por partes é avaliada e algoritmos utilizando deslocamentos de frequência mostram uma redução de pelo menos 1.5 vezes no tempo de execução, quando a altura da região imageada é menor que 30 mm. Além disso, comparado com interpolação linear por partes, algoritmos utilizando deslocamentos de frequência apresentam vantagens em CNR e tempo de execução quando a imagem reconstruída contém o fundo objeto.

**Palavras-chave:** Ensaios não-destrutivos, Imageamento ultrassônico, Migração de Stolt, FFT sobreamostrada, Interpolação

## LIST OF FIGURES

FIGURE 1	– Ultrasound inspection using pulse-echo mode	17
FIGURE 2	– Typical A-scan signal produced by a transducer	18
FIGURE 3	– Sweeping inspection and acquisition data	19
FIGURE 4	– Gating of B-scan images	19
FIGURE 5	– Effect of transducer aperture	20
FIGURE 6	– Constructive details and beam pattern of monostatic transducers	21
FIGURE 7	– Linear array transducer	22
FIGURE 8	– Elements arrangement for a linear array transducer	23
FIGURE 9	– 2-D and circular phased array transducer.	23
FIGURE 10	– Immersion testing using pulse-echo measurements	25
FIGURE 11	– Sweeping capture mode	25
FIGURE 12	– FMC mode with linear arrays	26
FIGURE 13	– Data set from a FMC acquisition	27
FIGURE 14	– Inspection using plane-wave with and without inclination	28
FIGURE 15	– Sweeping inspection simulation in CIVA	30
FIGURE 16	– Sweep inspection simulation results with CIVA	30
FIGURE 17	– Ultrasonic data before and after processing	31
FIGURE 18	– Specimen used for simulation of ultrasonic data	32
FIGURE 19	– Pulse echo and ERM	34
FIGURE 20	– Graphical representation of Stolt's migration	36
FIGURE 21	– B-scan image and image obtained with $\omega k$ -SAFT	39
FIGURE 22	– Representation of transducer and flaw	40
FIGURE 23	– B-scan and image obtained with Wavenumber	43
FIGURE 24	– B-scan image and image obtained with $\omega k$ -CPWC	47
FIGURE 25	– Effect of zero-padding on an A-scan signal	49
FIGURE 26	– Effect of zero-padding on an A-scan signal	49
FIGURE 27	– Sequence $x(n)$ and its spectrum $X(\Omega)$	51
FIGURE 28	– Sequences $x(n)$ and $\hat{x}(n)$ and its spectra $X(\Omega)$ and $\hat{X}(\Omega)$	51
FIGURE 29	– Frequency shift as a two-step operation	53
FIGURE 30	– Shifting closest points	54
FIGURE 31	– Specimen used acquisition of ultrasonic data	58
FIGURE 32	– Amplitude envelope of a signal	61
FIGURE 33	– Ultrasound image before and after post-processing	62
FIGURE 34	– CNR mask	63
FIGURE 35	– Effect of spatial resolution for the $\omega k$ -SAFT algorithm	66
FIGURE 36	– Effect of spatial resolution for the Wavenumber algorithm	66
FIGURE 37	– Effect of spatial resolution for the $\omega k$ -CPWC algorithm	67
FIGURE 38	– Effect of oversampling for the $\omega k$ -SAFT algorithm	68
FIGURE 39	– CNR as a function of oversampling, for the $\omega k$ -SAFT algorithm	69
FIGURE 40	– Effect of oversampling for the Wavenumber algorithm	70
FIGURE 41	– CNR as a function of oversampling, for the Wavenumber algorithm	70
FIGURE 42	– Effect of oversampling for the $\omega k$ -CPWC algorithm	71

FIGURE 43	– CNR as a function of oversampling, for the $\omega k$ -CPWC algorithm	72
FIGURE 44	– Execution time of the $\omega k$ -SAFT and NNS- $\omega k$ -SAFT algorithms	74
FIGURE 45	– Execution time of the Wavenumber and NNS-Wavenumber algorithms	76
FIGURE 46	– Execution time of the $\omega k$ -CPWC and NNS- $\omega k$ -CPWC algorithms	77
FIGURE 47	– Basic concept of the DAS algorithm	94
FIGURE 48	– Distance between the transducer and a point on the object	95
FIGURE 49	– B-scan image and image obtained with SAFT	96
FIGURE 50	– Distance between an emitter, a receptor and point on the object (FMC)	97
FIGURE 51	– B-scan and reconstructed images with SAFT and TFM	99
FIGURE 52	– Distance between an emitter, a receptor and point on the object (PWI)	100
FIGURE 53	– B-scan image and image obtained with CPWC	102
FIGURE 54	– Spectra of processed A-scan signals from flaw and bottom	105
FIGURE 55	– Spectra of processed A-scan signals from flaw and oversampling factor	106
FIGURE 56	– Spectra of processed A-scan signals from bottom and varying zero-padding	107
FIGURE 57	– Spectra of processed A-scan signals from flaw and bottom	108

## LIST OF TABLES

TABLE 1 – Classical time-domain and frequency-domain algorithms for the sweep, FMC and PWI capture modes. ....	32
TABLE 2 – Estimated number of floating point operations for each algorithm .....	77
TABLE 3 – CNR and execution time of the $\omega k$ -SAFT and NNS- $\omega k$ -SAFT algorithms, for a varying ROI height. The starting value of the ROI is kept constant and the final value is varied. Execution time and standard deviation are in milliseconds. ....	78
TABLE 4 – CNR and execution time of the (NNS)- $\omega k$ -SAFT algorithms for a varying ROI depth (constant $z_f$ ). ....	79
TABLE 5 – CNR and execution time of the (NNS)-Wavenumber algorithms for a varying ROI depth (constant $z_i$ ). ....	80
TABLE 6 – CNR and execution time of the (NNS)-Wavenumber algorithms for a varying ROI depth (constant $z_f$ ). ....	80
TABLE 7 – CNR and execution time of the (NNS)- $\omega k$ -CPWC algorithms for a varying ROI depth (constant $z_i$ ). ....	81
TABLE 8 – CNR and execution time of the (NNS)- $\omega k$ -CPWC algorithms for a varying ROI depth (constant $z_i$ ). ....	81

## LIST OF ACRONYMS

NDT	Nondestructive testing
DAS	Delay-and-sum
A-scan	Amplitude-scans
B-scan	Brightness-scan
B-mode	Brightness-mode
FMC	Full matrix capture
PWI	Plane-wave imaging
SAFT	Synthetic aperture focusing technique
TFM	Total focusing method
CPWC	Coherent plane-wave compounding
SDH	Side-drilled hole
FFT	Fast Fourier transform
ERM	Exploding reflector model
DFT	Discrete Fourier transform
NUFFT	Non-uniform fast Fourier transform
CNR	Contrast-to-noise ratio
ROI	Region-of-interest
SNR	Signal-to-noise ratio

## CONTENTS

<b>1 INTRODUCTION</b>	<b>13</b>
1.1 OBJECTIVES	15
1.2 DISSERTATION STRUCTURE	15
<b>2 THEORETICAL BACKGROUND</b>	<b>16</b>
2.1 ULTRASONIC NONDESTRUCTIVE TESTING	16
2.1.1 Operating principle	17
2.1.2 Transducers	20
2.1.3 Testing methods	24
2.1.4 Capture modes	25
2.1.5 CIVA	29
2.2 PROCESSING TECHNIQUES	30
2.2.1 $\omega k$ -SAFT	33
2.2.2 Wavenumber	40
2.2.3 $\omega k$ -CPWC	44
2.3 REVIEW	47
<b>3 INTERPOLATION-FREE STOLT MIGRATION</b>	<b>48</b>
3.1 INTERPOLATION BY FREQUENCY SHIFTS	50
3.2 STOLT'S MIGRATION BY FREQUENCY SHIFTS	52
3.3 EXTENSION TO ULTRASONIC IMAGING	54
3.4 REVIEW	57
<b>4 MATERIALS AND METHODS</b>	<b>58</b>
4.1 EXPERIMENTS	58
4.2 IMPLEMENTATIONS	59
4.3 PRE-PROCESSING	60
4.4 POST-PROCESSING	61
4.5 METRICS	61
4.6 REVIEW	62
<b>5 RESULTS AND DISCUSSION</b>	<b>64</b>
5.1 SPATIAL RESOLUTION	65

5.2 EFFECT OF THE OVERSAMPLING FACTOR .....	67
5.3 NUMBER OF FLOATING POINT OPERATIONS .....	72
5.4 RECONSTRUCTION QUALITY AND ROI HEIGHT .....	78
5.5 REVIEW .....	82
<b>6 CONCLUSIONS .....</b>	<b>83</b>
<b>REFERENCES .....</b>	<b>86</b>
<b>APPENDIX A – TIME-DOMAIN PROCESSING TECHNIQUES .....</b>	<b>93</b>
A.1 SAFT .....	93
A.2 TFM .....	96
A.3 CPWC .....	100
<b>APPENDIX B – EFFECT OF OVERSAMPLING ON STOLT’S MIGRATION .</b>	<b>104</b>

## 1 INTRODUCTION

Currently, petroleum is the main raw material in different products, ranging from plastic, fabric and other derivatives to fuel for transportation. In national territory, the production of petroleum expanded with the discovery of reservoirs in Bacia de Campos in 1974, which is situated in an area extending from the northern coast of the state of Rio de Janeiro to the southern coast of the state of Espírito Santo. Offshore production and exploration of petroleum presents several technological challenges and has driven the Brazilian research and development sector (SCHIAVI; HOFFMANN, 2015). Brazil invests heavily in the development of new technologies for offshore production and is world leader in deep and ultra deepwater petroleum production and exploration (MORAIS, 2013).

In offshore production, petroleum extracted from beneath the seafloor is transported to platforms on the surface via a piping system. This piping system is exposed to an extremely aggressive environment and corrosion can compromise its physical integrity. While new technologies and advances in material engineering have allowed production of steel alloys of higher resistance, monitoring these structures is of fundamental importance to assure its integrity and operation (GOUVEIA, 2010).

One approach to inspect the integrity of the piping system is with nondestructive testing (NDT). NDTs are methods to test an object without compromising its integrity or future use (BLITZ; SIMPSON, 1995). There are several NDT techniques, such as magnetic, ultrasonic, acoustic, liquid and optical methods (SHULL, 2002).

Ultrasonic methods for NDT are widely adopted in industry, due to its facilitated implementation, portability and ability to detect and characterize defects in the internal structure of solid objects (SCHMERR, 2016). In ultrasonic techniques, ultrasound waves are emitted into the inspected object and echo signals are generated when the waves encounter defects. Location and dimension of flaws can be determined from the detection and processing of the echo signals generated by the object. Transducers, built from piezoelectric materials, are responsible for conversion of high-voltage pulses into acoustic waves, as well as detecting echo signals from the object, converting acoustic waves into electric signals.

In the method considered as standard for ultrasonic NDT in industry, sound waves are emitted in the object under test by a transducer composed of several individual piezoelectric elements, where devices with 32, 64 and 128 elements are the most common for inspections (HOLMES et al., 2005; FAN et al., 2014). In this case, each element of the transducer emits a sound wave into the object, while all elements receive echo signals, with this process being repeated for all elements. However, acquisition time and data volume generated by inspections with this method are usually large. This leads to a long operational time of the equipment used to perform the inspection of submarine structures, increasing costs (SUTCLIFFE et al., 2012). Since data acquired from inspections must be processed to obtain images representing the internal structure of objects, a high volume of data converts into long processing time.

In the last decade, alternative methods for acquisition and processing of ultrasonic data have been proposed (MONTALDO et al., 2009; BANNOUF et al., 2013; BERNARD et al., 2014; PENG et al., 2014; YANG et al., 2014b; DAVID et al., 2015; BESSON et al., 2016b; MOGHIMIRAD et al., 2016; MATRONE et al., 2016; BESSON et al., 2016a; HU et al., 2017; LIU et al., 2017; SCHIEFLER et al., 2018). New acquisition methods, as well as processing techniques, have been proposed to decrease acquisition time, data volume, and processing time.

The focus of this research is to develop fast algorithms, in order to reduce the processing time to obtain an image from the ultrasonic data. Ultrasonic data can be processed directly in the time-domain, with algorithms based on the well-known delay-and-sum (DAS) technique. Frequency domain algorithms have been used due to their lower computational complexity compared to DAS-based approaches. (HUNTER et al., 2008; GARCIA et al., 2013). Common implementations of frequency-domain algorithm for ultrasonic imaging are based on Stolt's migration, which requires interpolation on the frequency spectrum of the echo data. This interpolation is usually achieved by oversampling of the frequency spectrum, via zero-padding of the echo data, and piecewise-linear interpolation of the resulting frequency spectrum. Since the oversampling factor usually needs to be high, the performance of frequency-domain algorithms based on Stolt's migration is degraded.

In this research, we investigate an alternative method to the oversampling and piecewise linear interpolation employed to complete Stolt's migration. This interpolation-free method is based on the time/frequency shifting property of the Fourier transform and consists of shifting the frequency spectrum to obtain the samples required by Stolt's migration. The resulting frequency shifting algorithm was first conceived to focus radar images (LI et al., 2014) and is extended to ultrasonic imaging in this study. We show that migration by

frequency-shifts is able to replace piecewise linear interpolation for three common frequency-domain algorithms, and we compare the results obtained by each method in terms of image quality and number of floating point operations. Compared to the combination of oversampling and piecewise linear interpolation, migration by frequency shifts presents a lower number of floating point operations depending on the height of the inspected region, while preserving image quality. This leads to similar images with a shorter execution time. In addition, if the ultrasonic data contains echo signals from the bottom of the object, or from a flaw with large lateral dimension, algorithms using frequency shifts presents equal or superior reconstruction quality at lower execution times, when compared to algorithms using oversampling and piecewise linear interpolation.

## 1.1 OBJECTIVES

This work aims to extend an interpolation-free migration algorithm, first proposed for radar imaging, to three common frequency-domain ultrasonic imaging algorithms, which are based on Stolt's migration. Specific objectives consists of:

- Review and implementation of frequency-domain algorithms based on Stolt's migration for ultrasonic imaging;
- Review, implementation and adaptation of interpolation-free algorithm for ultrasonic imaging;
- Evaluation and comparison of conventional piecewise linear interpolation and interpolation-free method for frequency-domain algorithms.

## 1.2 DISSERTATION STRUCTURE

This dissertation is structured as follows. Chapter 2 presents an overview of ultrasonic NDT, presenting the theoretical principles of pulse-echo ultrasound, types of transducers, schemes for data acquisition and processing techniques. Chapter 3 discusses, the interpolation-free algorithm for Stolt's migration, as well as its adaptation and extension to ultrasonic imaging. Materials and methods are presented in Chapter 4. The results obtained with the frequency-domain algorithms using piecewise linear interpolation and the interpolation-free scheme are compared and discussed in Chapter 5, while the concluding remarks of this dissertation are presented in Chapter 6.

## 2 THEORETICAL BACKGROUND

This chapter outlines the theoretical background of this study and is divided in two parts. The first part reviews the ultrasonic NDT technique. In this part, the operating principles of ultrasonic NDT are discussed, first with monostatic transducers and subsequently with phased arrays. Next, in the second part, classic processing methods for ultrasonic image reconstruction are discussed and the classic frequency domain algorithms are presented.

### 2.1 ULTRASONIC NONDESTRUCTIVE TESTING

Ultrasonic NDT has prevalent use in industry, due to characteristics such as portability, ease of implementation and ability to detect flaws of reduced dimension (GUARNERI, 2015; SHULL, 2002; BLITZ; SIMPSON, 1995). Among several structural and integrity testings, ultrasonic inspections can be applied for location of defects in maritime structures, detection of cracks in components of nuclear plants and testing of pipeline welds (SHULL, 2002; ANDREUCCI, 2011). Ultrasound is also commonly used in the medical field, where ultrasound imaging is applied in the detection and diagnosis of diseases and lesions, as well as in the study of blood flow (HOSKINS et al., 2010).

Ultrasonic applications for NDT were initially developed between 1920 and 1940 (COBOLD, 2006; SHULL, 2002; WADE, 1975). In the late 1920s, Sergei Y. Sokolov proposed a method for the detection of flaws in materials using ultrasonic waves. Later, in the early 1930s, Muhlhauser patented a system which used two transducers to examine a test piece. The proposed method, denoted nowadays as *through-transmission*, uses the two transducers placed on opposite sides of the object under inspection, where one transducer is used to emit acoustic waves and the other transducer is used to receive the acoustic waves. However, the major breakthrough came in the yearly 1940s, when Floyd Firestone proposed a system called "Ultrasonic Reflectoscope", which employs the method now denoted as *pulse-echo* and constitute the basic operating principle of the vast majority of modern ultrasound scanners. The system developed by Firestone required only a single transducer and consisted of emitting short, pulsed waves into the object and subsequently detecting echo signals from the object.

Although ultrasonic NDT has widespread adoption in industry and in the medical field, its use presents some challenges. Conduction of testings and analysis of data must be performed by qualified personnel. Since ultrasonic transducers are of small dimensions, only small portions of the testing object can be inspected at a time. In addition, for contact testing, coupling gels or liquids may need to be applied to the surface of the testing object. These couplants may cause the inspection of large areas to become infeasible and, if not properly removed, these coupling elements can damage the object. In this section, the main concepts of the pulse-echo ultrasound technique will be presented, discussing testing modes, common types of transducers and common capture modes.

### 2.1.1 Operating principle

Ultrasound inspection is based on the concept of propagation and reflection of acoustic waves, as shown in Figure 1 (SCHMERR, 2016; SHULL, 2002; BLITZ; SIMPSON, 1995). A transducer is responsible for emitting an acoustic wave which propagates through the object under test, assumed to be homogeneous, as illustrated in Figure 1a. Upon encountering a flaw, a portion of the emitted wave is reflected, generating an echo signal, as shown in Figure 1b. The echo signal travels back to the surface and can be detected by the transducer, as indicated in Figure 1c. This is known as pulse-echo mode, since a single transducer generates acoustic waves that are transmitted to the object and records echo signals produced by flaws from within the object. In the setting shown in Figure 1, the transducer is in direct contact with the object under test. However, it is common to apply a coupling gel or liquid between the face of the transducer and the area of contact. This facilitates penetration of the waves generated by the transducer into the object.

After emission of the ultrasonic pulse, the transducer becomes a receiver, converting acoustic waves into electric signals (SCHMERR, 2016). An electronic circuit is responsible for acquisition, sampling and digitization of the electric signals generated by the transducer.

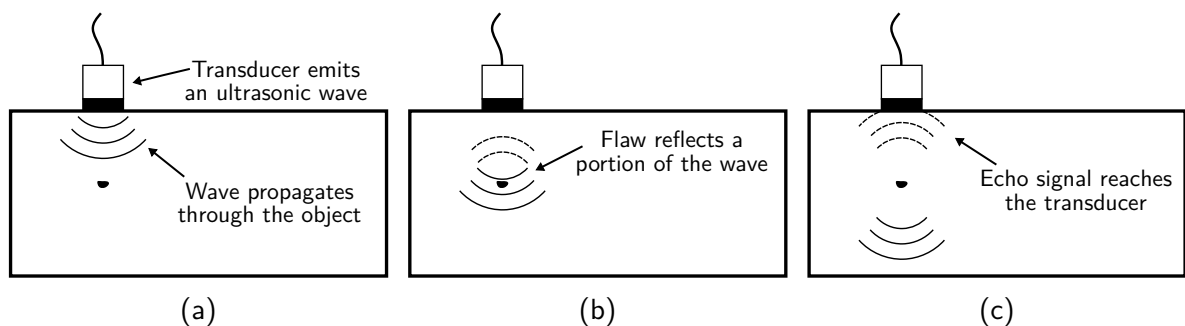


**Figure 1: Ultrasound inspection using pulse-echo mode. (a) The transducer emits an ultrasonic wave, which propagates through the object and (b) is reflected by flaws within the object, (c) generating echo signals that reaches the transducer at the surface.**

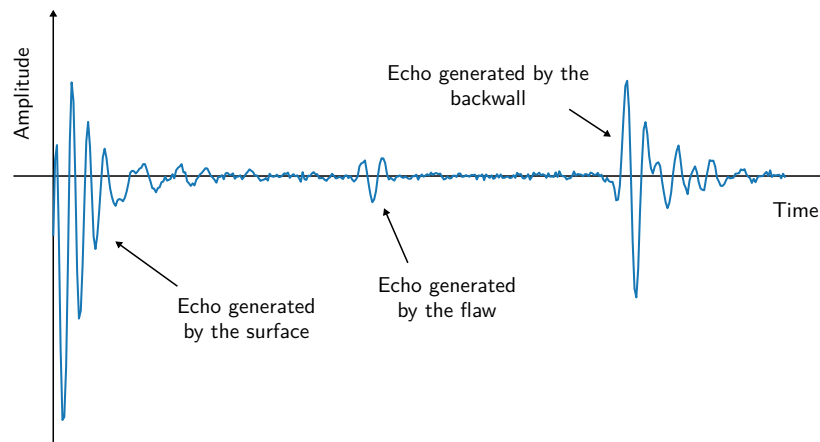


**Figure 2: Typical A-scan signal produced by a transducer. This example shows three echo signals, originated from the flaw, surface and backwall of the object under test.**

Figure 2 shows a signal produced by a transducer from testing of a solid object containing a single flaw. In this case, three echo signals were detected by the transducer. When the ultrasonic pulse is first emitted by the transducer, the wave penetrates the object through its exterior surface (or frontwall). A portion of the wave is reflected by the surface, generating the first echo signal detected by the transducer, which has a higher amplitude due to the strong reflection of the wave. The second echo signal has a lower amplitude, and corresponds to the wave reflected by the flaw within the object under test. In this case, the flaw is small, and the echo signal detected by the transducer has a lower amplitude. The third echo signal shown in Figure 2 corresponds to the bottom (or backwall) of the object under test. The backwall also presents a strong reflection of the ultrasonic wave and the echo signal detected by the transducer has a higher amplitude. However, depending of the size and shape of the flaws within the object, as well as on the attenuation of the material, echo signals from the backwall may be weak or not even be detected.

Signals produced by the transducer are known as *Amplitude-scans* (A-scan), and these signals contain information with respect to the internal structure of the object under test. In the example illustrated in Figure 2, it is possible to identify the signals with higher amplitude as resulting from the surface and bottom of the object, whereas the smaller amplitude signal indicates an echo signal produced by a flaw. If the propagation velocity of the wave on the object is known, it is possible to estimate the location of the flaw.

The A-scan signal shown in Figure 2 corresponds to the transducer scanning in a fixed position on the object, as illustrated in Figure 1. It is possible to move the transducer to inspect other areas of the object, as shown in Figure 3 (HANGIANDREOU, 2003; ALOBAIDI et al., 2015). In this case, indicated in Figure 3a, the transducer is moved laterally on the object under test and A-scan signals are recorded on each position. This is also known as a sweeping inspection. The acquired signals can be stored in a matrix, where each column represents

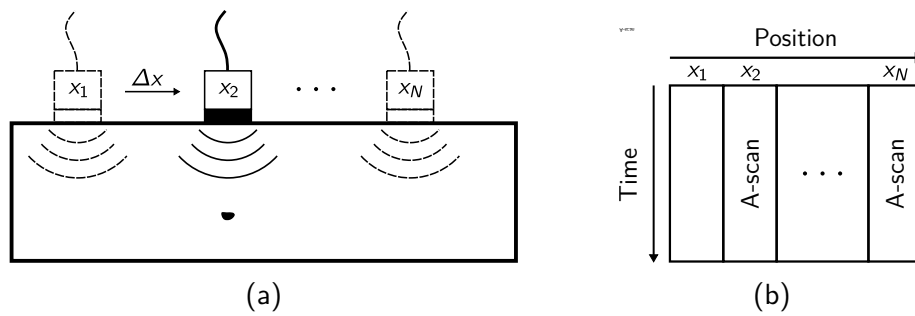


**Figure 3: Sweeping inspection. (a) The transducer moves laterally on the object, acquiring one A-scan signal for each position. (b) The set of A-scan signals obtained for all positions can be stored in a matrix, where each column represents one position of the transducer.**

one position of the transducer and each position of each column is one digital sample of the A-scan signal, as shown in Figure 3b. An image can be formed from this matrix, where the intensity of each pixel represents the amplitude of the A-scan signal for that position. The image formed from several A-scans is denoted *Brightness-scan* or *Brightness-mode* (B-scan or B-mode) and can also be used as a initial diagnosis of the testing object.

Figure 4 shows a B-scan image, obtained from data of a sweeping testing. In Figure 4a, it is possible to identify the surface and backwall of the object under test, which appear with higher amplitude (brightness) on the image. A flaw can also be identified, but with reduced brightness. Since echo signals generated by the object's surface and backwall have a higher amplitude, it is common to process the A-scan signals to remove these portions of the echo signals. This processing can be performed by the equipment acquiring the A-scan signals, where a time window for acquisition, denoted *gate*, can be defined. Gating can also be performed after acquisition of the A-scan signals, removing digital samples of the recorded signal. Figure 4b shows a B-scan image with gating. Since surface and backwall signals are omitted, the signal corresponding to the flaw appears brighter.

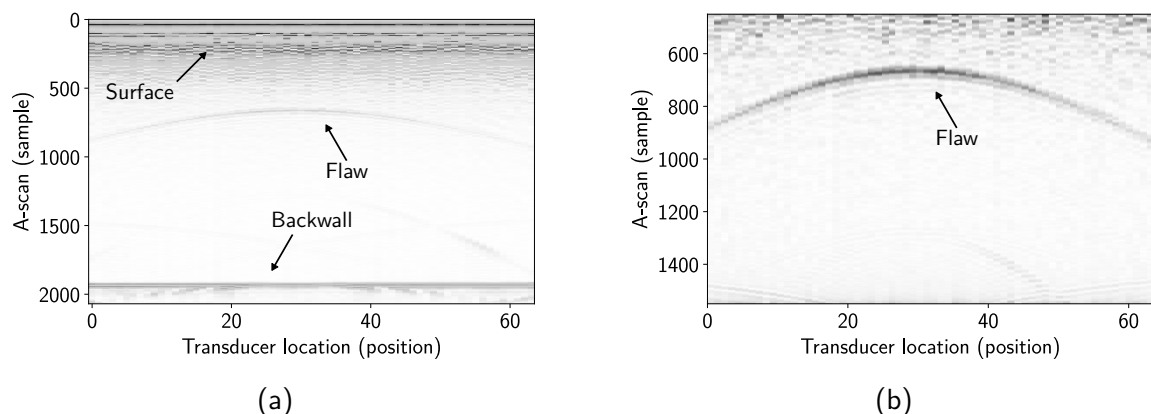


**Figure 4: Gating of B-scan images. (a) In a B-scan without gate, the surface and backwall appear brighter than the flaw. (b) In a B-scan after gating, the surface and backwall echo signals are removed and the flaw appears brighter on the image.**

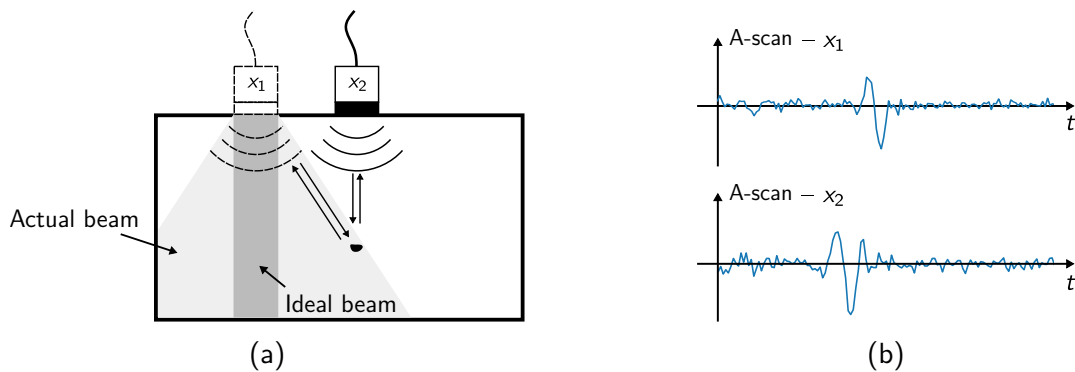


**Figure 5: Effect of transducer aperture. (a) Due to the aperture of real transducers, flaws nearby the transducer generate echo signals. (b) These echoes appear in the A-scan signals acquired with the transducer on different locations.**

Ideally, the ultrasound beam produced by the transducer does not diverge and, as a consequence, received echo signals are generated only by flaws directly under the transducer. However, wavefronts emitted by the transducer diverge in the far field, such that the wavefronts are able to reach flaws nearby, which generate echo signals, as shown in Figure 5 (ANDREUCCI, 2011). Due to this beam aperture, echo signals generated by the same flaws appear in A-scan signals obtained with the transducer in different positions. In the example illustrated in Figure 5a, although the flaw is directly below the transducer in position  $x_2$ , the transducer positioned in  $x_1$  also receives an echo signal, even though there is no flaw directly below position  $x_1$ . In this case, the echo generated by the flaw appears in the A-scan of position  $x_1$  with a delay with respect to the A-scan signal of position  $x_2$ , as shown in Figure 5b. Real transducers have a certain aperture and only A-scan signals and B-scan images may be insufficient to determine the internal structure of the object under inspection, and signal processing techniques are necessary to construct more accurate representations.

### 2.1.2 Transducers

Transducers are made with piezoelectric elements, which are responsible for the emission and reception of acoustic waves (DRINKWATER; WILCOX, 2006; MANTHEY et al., 1992; SHUNG; ZIPPURO, 1996). Piezoelectric crystals allow the conversion of electric pulses into acoustic waves, as well as to convert acoustic waves into electric signals. Transducers can be classified according to number of elements and their arrangement.

In the early development of ultrasonic techniques, spanning from the early 1930s to the late 1960s, the transducers containing a single crystal element (monostatic transducer) were employed for generation and reception of acoustic waves and were successfully applied for detection of flaws in solid materials (COBBOLD, 2006; SHULL, 2002; WOO, 2002). However, monostatic transducers cannot produce images without being physically displaced along the surface of the object under test, which was a limitation for medical applications and motivated

the design of new types of transducers. In the late 1960s and early 1970s, several research groups proposed phased and linear array transducers, which are transducers consisting of several crystal elements capable of generating and detecting ultrasonic waves. Commercial ultrasonic systems with array transducers were first developed for medical applications and made available in 1972. Ultrasonic systems with array transducers directed at industrial applications came much later, in the 1980s.

Nowadays, both in industry and in the medical field, the use of array transducers is commonplace. Monostatic transducers are still used in portable systems and recent research for NDT still focus on systems employing monostatic elements (QIN et al., 2014; GUARNERI et al., 2015; WU et al., 2015; JIN et al., 2017b, 2017a). This sections describes monostatic, linear and phased array transducers.

#### 2.1.2.1 Monostatic

A monostatic transducer consists of a single piezoelectric element, and its basic components, as well as its beam pattern, are shown in Figure 6 (NASCIMENTO, 2013; NAKAMURA, 2012). The essential components of a monostatic transducer are the piezoelectric crystal, electrodes, backing and matching layers, conductors and connectors, as illustrated in Figure 6a. The piezoelectric element is responsible for the generation and reception of acoustic waves. Due to the piezoelectric effect, the piezoelectric crystal is deformed when an electric potential difference is applied across the electrodes plated on its parallel faces, which allows to control the generation of acoustic waves with electric pulses. In addition, the piezoelectric crystal generates an electric potential difference across the electrodes when the crystal is mechanically deformed, which allows to detect acoustic waves. A matching layer is used to protect the piezoelectric crystal against mechanical wear, in addition to match the acoustic impedance between the crystal and the outside medium. The backing layer provides mechanical

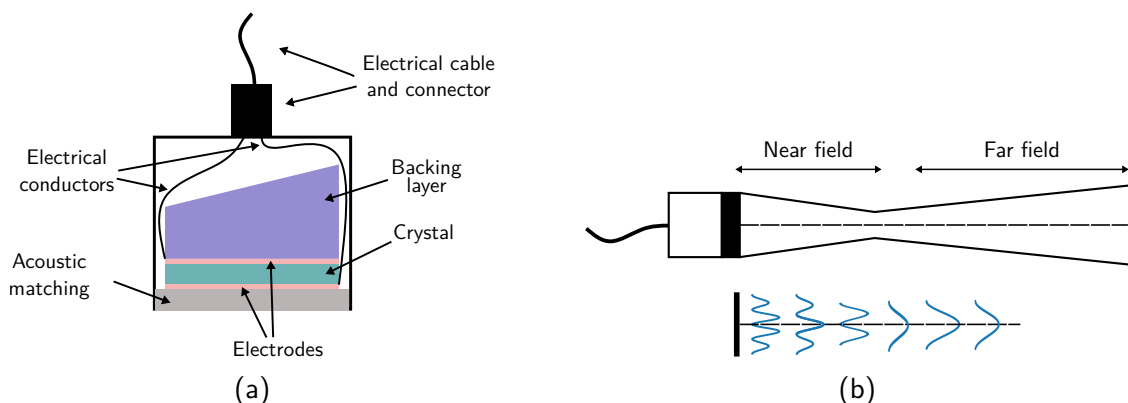


**Figure 6: Constructive detail of monostatic transducer (left) and beam pattern (right).**  
**Source: Adapted from Nascimento (2013) and Cheeke (2012).**

support for the crystal, as well as attenuation of acoustic waves and to avoid reverberations, which is the effect caused by the successive reflection of the same wave by two highly reflective surfaces.

The wave emitted by the transducer can be considered as a planar wavefront only in the region denoted as the far field (CHEEKE, 2012; SHUNG; ZIPPURO, 1996). In the region near the face of the transducer, denoted as the near field, the emitted wave shows an oscillatory interference pattern which does not correspond to a planar wavefront, as illustrated in Figure 6b. The interference pattern generates a planar wavefront only after a certain distance from the face of the transducer, with an amplitude which exponentially decreases with increasing distance. As shown in Figure 6b, the maximum intensity of the wave in the far field occurs in the main axis of the transducer and the maximum absolute value is known as the focus of the transducer. Since in the focus region the intensity of the wave is higher, echo signals will also have higher amplitudes, which benefits inspections in that region.

#### 2.1.2.2 Linear arrays

Linear array transducers are transducers that contains more than one element capable of emitting and receiving acoustic waves (DRINKWATER; WILCOX, 2006). Control of each individual element allows a greater flexibility in the emission and reception of acoustic waves, and ultrasonic transducers with 32, 64 and 128 elements are the most common, although transducers with 256 elements are also manufactured.

Figure 7 shows a linear array transducer used to generate different ultrasonic waves. In Figure 7a, all individual elements are simultaneously excited with an electric pulse and interference from the waves generated by each element results in a single, planar wavefront. In this case, the resulting wave has energy higher than the wave generated by each element,

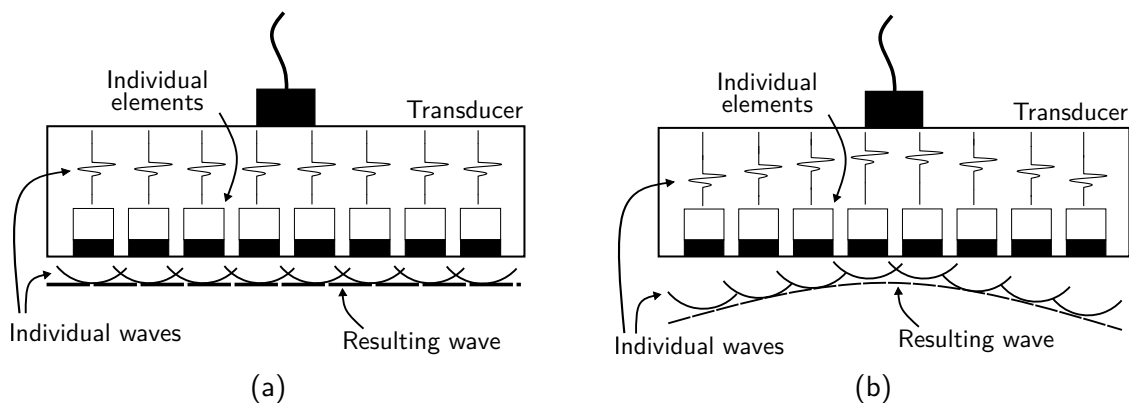


**Figure 7: Linear array transducer, with different delay laws. (a) When all elements are simultaneously excited with electric pulses, waves generated by each element show an interference pattern that results in a single, planar wavefront. (b) The elements can also be excited at different time instants, which can result in a focused beam (right).**

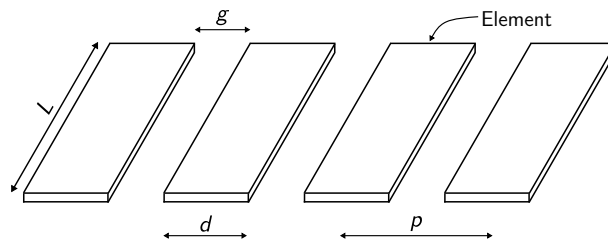


**Figure 8: Elements arrangement for a linear array transducer.**

which allows the resulting wave to penetrate deeply into the object. In Figure 7b, the individual elements are excited with electric pulses at different time instants, such that the resulting wave is focused. In this case, the resulting ultrasonic beam generated by the transducer can have a small overall aperture and the focal point can be electronically controlled by the pulse sequence, also referred to as the *delay law*.

The individual elements of the linear array transducer are arranged as illustrated in Figure 8. Each element has a rectangular shape, with length  $L$  and width  $d$ . The elements are spaced equally, by a distance (gap)  $g$ . It is common to specify a transducer by its *pitch*  $p$ , which is the center-to-center distance between two adjacent elements.

Currently, linear array transducers are the most commonly used type of transducers in industry and in the medical field, due to its flexibility and possibility to produce real-time images of the testing object. This is in contrast with monostatic transducers, which requires physical displacement of the transducer to generate an image.

### 2.1.2.3 Phased arrays

Linear array transducers are a sub-class of phased array transducers. While the elements of a linear array are rectangular and arranged side-by-side, there are several other possible shapes and arrangements for the elements (DRINKWATER; WILCOX, 2006; SHUNG; ZIPPURO, 1996). Figure 9 shows two common arrangements. The arrangement with square elements laid out in a matrix allows to capture 3-D images of the testing object (Figure 9a), while the circular arrangement allows different focal points (Figure 9b).

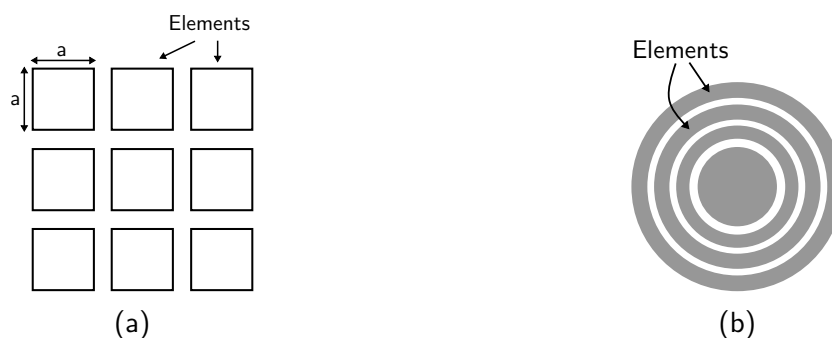


**Figure 9: (a) 2-D and (b) circular phased array transducer.**

### 2.1.3 Testing methods

The ultrasonic waves generated by the transducer must be properly transmitted to the test piece, which is achieved by coupling the transducer with the surface of the object. Two common coupling methods are by applying a thin layer of couplant between the the face of the transducer and the surface of the object or by placing both the transducer and the object in a coupling medium, which are known as contact testing and immersion testing, respectively.

In contact testing, the transducer is placed in contact with the object by means of a thin layer of a couplant. The couplant is responsible for the acoustic matching between the transducer and the material of the object under inspection, such that the wave emitted by the transducer is able to penetrate into the object (NASCIMENTO, 2013; ANDREUCCI, 2011). The couplant is chosen based on the material and roughness of the surface of the object. In general, the couplant is a gel or a liquid, with oil, water and glycerin the most commonly used substances. In addition, there are synthetically produced couplants, developed for specific applications, having superior coupling performance.

The main advantage of contact testing is that waves are transmitted to the object with higher intensities, since the coupling layer minimizes losses at the transducer-object interface. Moreover, the majority of ultrasound signal processing algorithms were developed considering a direct contact between the transducer and the test piece. A disadvantage of contact testing is that the couplant must be chosen carefully, to avoid damage to the object, caused by chemical reactions. For instance, glycerin can lead to water accumulation of the surface of the object, which in turn can lead to corrosion or even the accumulation of mold. This can compromise the integrity of the test piece. In addition, inspection of large areas may become inconvenient, due to the need to apply couplant to a large area (COLLINGWOOD, 1987).

In immersion testing, the transducer and the object are immersed in a coupling medium (usually water) and are not in direct contact, as shown in Figure 10. Waves emitted by the transducer are conducted by the coupling medium and penetrate into the object, producing echo signals based on its internal structure, surface and backwall (ANDREUCCI, 2011).

The coupling between transducer and object in immersion testings has a more homogeneous distribution when compared to contact testing, which allows a better control of the energy that is transmitted to the object (SCHMERR, 2016). Although the coupling is more homogeneous, the intensity of the emitted wave that penetrates into the object is much lower than the case where there is a direct contact between transducer and object. Algorithms also become more complex for processing data from immersion inspections, since the wave propagates through different media with different propagation speeds, leading to increased refraction in the coupling/object interface.

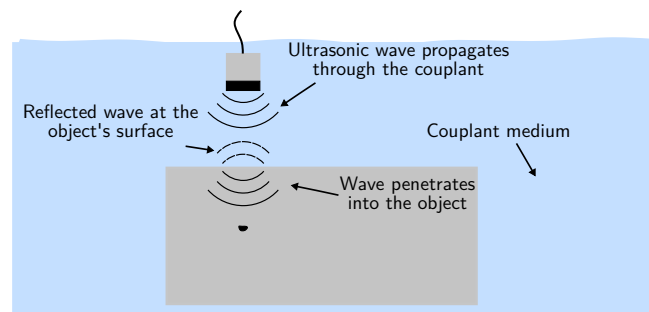


**Figure 10: Immersion testing using pulse echo measurements. The transducer and the test piece are immersed in a couplant medium. The transducer emits an ultrasonic wave, which first propagates through the coupling medium before penetrating into the object.**

#### 2.1.4 Capture modes

Capture mode refers to how the waves are emitted and how the echo signals are acquired. In the early development of ultrasonic techniques, monostatic transducers and sweeping inspections were the most common. Currently, linear array transducers are most commonly used in both industry and in the medical field, along with the Full Matrix Capture (FMC) mode. Although considered standard practice, the FMC mode for linear arrays has a few drawbacks, such as the time to acquire all sets of signals and the volume of data. Recent studies have been directed to overcome the main disadvantages of the FMC mode, with plane-wave image (PWI) one of the proposed methods.

##### 2.1.4.1 Sweeping

In sweeping inspections, a monostatic transducer is laterally displaced along the surface of the testing object, as illustrated in Figure 11. The lateral movement is dictated by a step  $\Delta x$ , which must be constant, and at each step, the transducer emits acoustic waves and receives echo signals. After the transducer sweeps all lateral positions, a B-scan image can be formed from the acquired data. However, only the B-scan image may be insufficient to characterize the internal structure of the object, owing to the aperture of the transducer. The B-scan image can be processed using the Synthetic Aperture Focusing Technique (SAFT), to produce a more accurate representation of the object (LINGVALL; STEPINSKI, 2001).

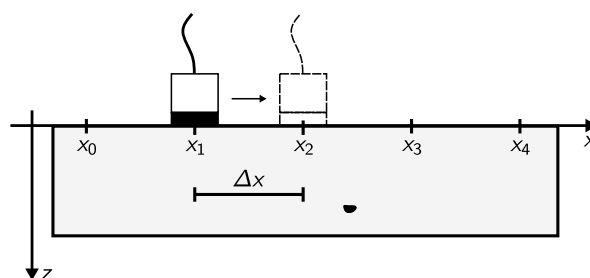


**Figure 11: Sweeping capture mode. The transducer is displaced on the  $x$  axis, by a fixed step  $\Delta x$ . A-scans signals are acquired for each position and stored in a matrix.**

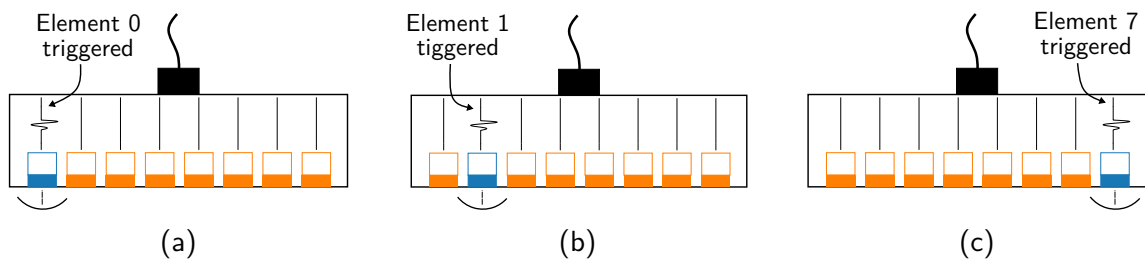


**Figure 12: FMC mode with linear arrays. (a) First, element 0 of the array, highlighted in blue, emits a ultrasonic wave, while all elements, including element 0, record the echo signals. (b) Next, this acquisition process is repeated for element 1. (c) The procedure is finished when the acquisition process is completed by the last element of the array.**

#### 2.1.4.2 FMC

A commonly used acquisition scheme with linear array transducers is the FMC. The method consists of obtaining acquisition data for all possible combinations of emitting and receiving elements of the transducer (HOLMES et al., 2005; WESTON et al., 2012). Although previously described in the context of medical imaging, this method was successfully applied for NDT only in the 2000s, with the development of processing techniques capable of processing the FMC data. Since then, FMC is considered as the default acquisition method for ultrasonic NDT using linear array transducers (FAN et al., 2014).

Figure 12 illustrates this capture mode for a linear array transducer with 8 elements. Elements in blue are elements which transmit and receive ultrasonic waves, while elements in orange only receive echo signals. Initially, as shown in Figure 12a, element 0 of the transducer emits an ultrasonic wave, while all elements, including element 0, receive the echo signals. This process is then repeated for element 1, as shown in Figure 12b. The FMC acquisition is completed after the last element of the array, illustrated in Figure 12c, emits an ultrasonic wave and the echo signals are recorded by all elements.

The FMC data obtained after completion of the acquisition procedure is schematically shown in Figure 13. After element 0 emits an ultrasonic wave, an A-scan signal is recorded by each element of the transducer, as shown in Figure 13a. This data can be grouped in a 2-D matrix, where each column represents an A-scan for each element. In Figure 13, for each 2-D matrix shown, columns in blue represents array elements which emitted the ultrasonic pulses and received the echo signals, while columns in orange represents only elements which received the echo signals. After emission with element 0 and reception with all elements, the procedure is repeated for element 1, and the data obtained is grouped in another 2-D matrix, as illustrated in Figure 13b. The procedure is repeated until a 2-D matrix has been obtained for the last element, represented by element 7 in Figure 13c. The 2-D matrices obtained for each element that emitted ultrasonic pulses can be grouped into a single 3-D matrix, which is denoted as the FMC, and is represented schematically in Figure 13d.

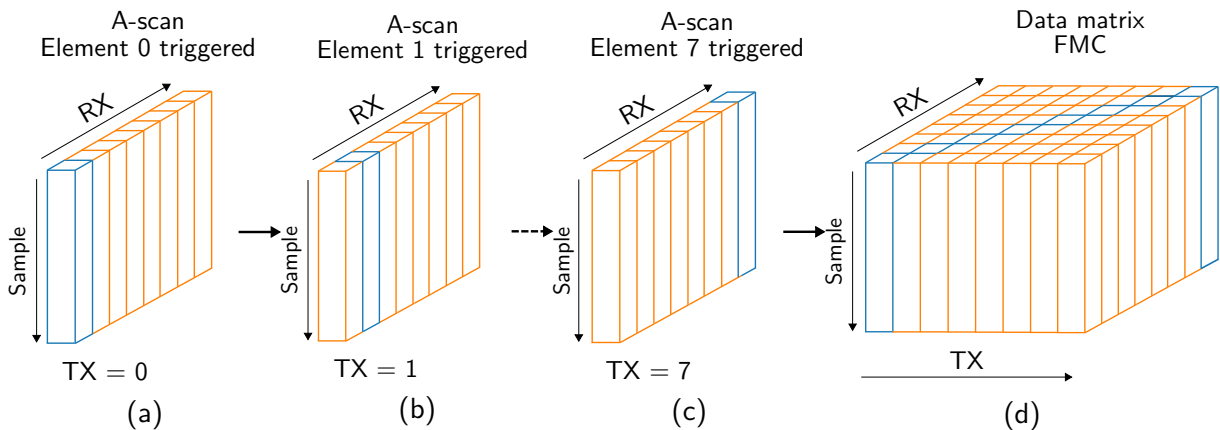


**Figure 13: Data set from a FMC acquisition. (a) After emission with element 0 and reception with all elements, a 2-D data set with A-scan signals is obtained, where blue columns represent the element that emitted and received the ultrasonic pulses and columns in orange represent the elements which received the echo signals. (b) The acquisition procedure is repeated for element 1, where another 2-D matrix is obtained. (c) The procedure is completed when the last element, in this case element 7, has obtained the set of echo signals. (d) After the completion of the acquisition process, all 2-D data sets obtained can be combined in a single 3-D matrix, denoted as the FMC.**

Linear arrays also allow to emulate a sweeping acquisition. In the FMC procedure, each element emits an ultrasonic pulse while all elements receive the echo signals. Another approach is to emit and receive the ultrasonic waves with only the same element. If this procedure is repeated for all the elements, the array emulates a sweeping inspection. Another way to obtain sweeping data is directly from the FMC, with the extraction of data from the 3-D matrix of A-scans. In this case, elements in the diagonal of the 3-D matrix (highlighted in blue in Figure 13d) represent emission and reception with the same element. Thus, A-scan signals in the diagonal of the FMC represent a sweeping inspection.

The FMC mode is one of the most common capture modes used with linear arrays. Specific processing techniques for the FMC data allow to obtain an image of the internal structure of the object and, currently, the Total Focusing Method (TFM) algorithm is considered as the “gold standard” for the processing of FMC data (FAN et al., 2014). Several ultrasound equipment have dedicated hardware to implement operations required by the TFM, aiming to accelerate the algorithm and to produce real-time images from the target object. However, the FMC mode has some disadvantages. Since each element of the array must individually emit a pulse, repeating this procedure for all elements increases acquisition time (SUTCLIFFE et al., 2012). In addition, the volume of generated data can be significant, since a B-scan data set is stored for each element of the transducer.

### 2.1.4.3 PWI

Another approach for ultrasonic imaging is to use plane-waves. In this method, denoted PWI, the elements of the transducer are triggered simultaneously, which leads to the individual ultrasonic waves emitted by each element to interfere resulting in a single, planar wavefront (MONTALDO et al., 2009). Application of the PWI technique first emerged for medical ultrasound in 1980, with a system denoted “*Explososcan*” (SHATTUCK et al., 1984), followed by the first applications in early 1990s, from the theory of nondiffracting beams (LU, 1997) and early 2000s, using conventional time-domain processing techniques (SANDRIN et al., 2002). For NDT, PWI was adapted for multimodal imaging and immersion inspections only more recently (JEUNE et al., 2016b, 2016a), although the technique was already employed in contact testings (MONTALDO et al., 2009).

The generation of plane-waves with a linear array transducer is shown in Figure 14. Excitation of all elements simultaneously, as illustrated in Figure 14a, allows the emitted waves to interfere with each other in such way that the result is a single, planar wavefront, having higher energy than the waves emitted by each element individually. This allows to illuminate an entire inspection region with a single emission, decreasing acquisition time and the volume of generated data, as well as to allow inspection of deeper areas of the object. Fewer emission pulses allow higher frame (image) rate, which benefits several medical applications. For instance, in medical ultrasound, the transient elastography and Supersonic Shear Imaging (SSI) techniques use plane-waves to study the elasticity of organs and tissues, which requires a high image rate (BERCOFF et al., 2003, 2004). The study of elasticity can be used in the diagnosis of lesions and even cancer (WELLS; LIANG, 2011).

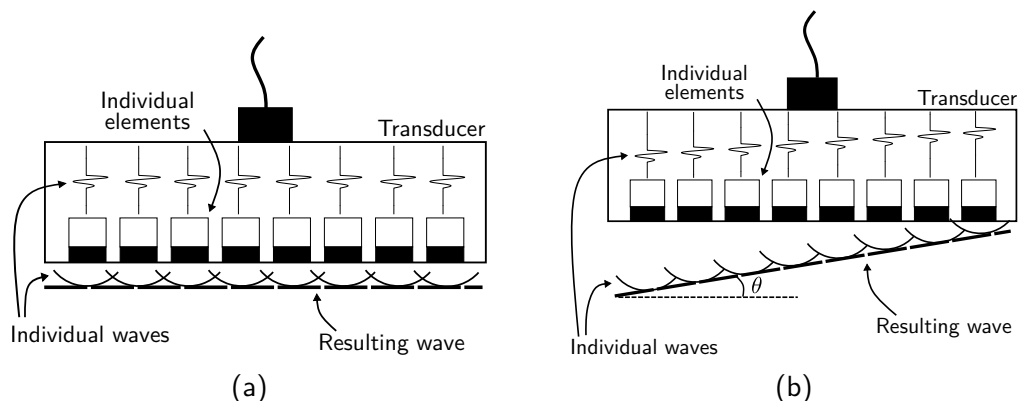


**Figure 14: Inspection using plane-wave (a) without and (b) with inclination. When all elements of the transducer are triggered simultaneously, the individual waves interfere such that a plane-wave is generated. Applying an appropriate delay law allows the plane-wave to be emitted with a certain angle.**

A drawback of PWI is that the emitted plane-waves does not have focus. This causes resulting PWI images to present low contrast and resolution. One way to improve resolution and contrast of the obtained image is with coherent plane-wave compounding (CPWC). In this method, several plane-waves with different steering angles are emitted in the medium. Data obtained from each acquisition are processed to produce a single image with higher resolution and contrast. As illustrated in Figure 14b, an appropriate delay law can be used, such that the individual waves emitted from the elements of the transducer interfere to form a single plane-wave with inclination  $\theta$ .

Initially, the development of PWI was directed at medical ultrasound, where inspections are performed with a direct contact between the transducer and the object under test, while the surface of the object can be assumed to be planar. In contrast, NDT inspections usually consists of objects with irregular surfaces, and immersion testings are common. Moreover, transducer for NDT are in general smaller than transducers for medical ultrasound, which results in images with smaller widths. Due to this necessary adaptations and the size limitation, the PWI technique has only been fully developed for NDT much more recently, with adaptations for immersion testings, multimodal imaging and objects with irregular surfaces (JEUNE et al., 2016b, 2016a; CRUZA et al., 2017; MERABET et al., 2019).

### 2.1.5 CIVA

CIVA is a software that allows simulation of NDT (CALMON et al., 2006; CALMON, 2012; RAILLON et al., 2012). Inicially developed by the French Alternative Energies and Atomic Energy Comission (CEA, *Commissariat à l'énergie atomique et aux énergies alternatives* in french), the CIVA software is currently developed and maintained by EXTENDE. Among several NDT techniques, CIVA allows simulation of ultrasonic testings with a wide range of options and settings. It is possible to simulate objects with complex geometries and different materials, in contact or immersion testings. CIVA simulates the propagation of the wave on the object from the geometry of the transducer, which can be defined or set from a predefined model, such as monostatic or phased array transducers. Simulations allows validation of processing techniques, allowing a multitude of testing settings, conditions and test pieces.

Figure 15 shows the model for simulation of an ultrasonic testing. In this example, a monostatic transducer is placed directly in contact with the test piece, for the simulation of a sweeping inspection, and it is possible to define the material of the object, the size of the transducer, its initial position, as well as the number of steps for the sweep and the step size, among many other possible settings. Wave propagation and interaction with the test piece is simulated for each position of the transducer. The results are presented as B-scans signals and individual A-scan signals, as shown in Figure 16.

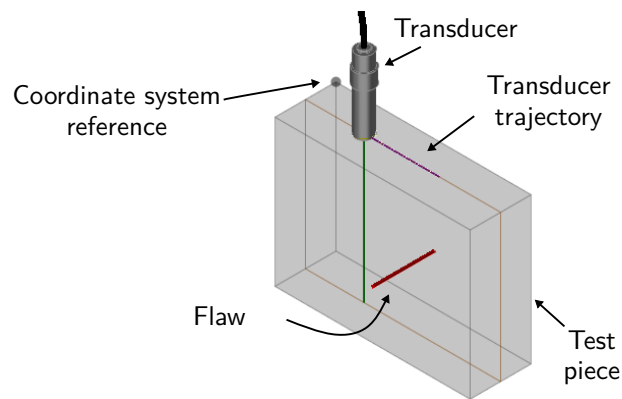


**Figure 15: Sweeping inspection simulation in CIVA.**

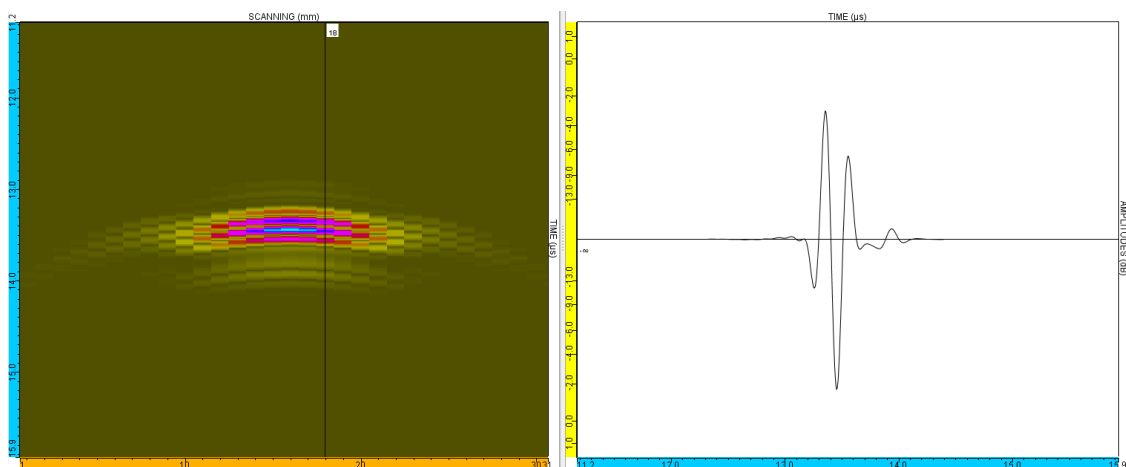


**Figure 16: Sweep inspection simulation results with CIVA: B-scan (left) e individual A-scan (right).**

The software also allows the use of phased arrays and linear arrays, with several predefined capture modes. Simulations of FMC and PWI captures are readily available through predefined models that generates the necessary delay laws for the transducer. Moreover, the software allows the use of processing techniques for the simulated ultrasonic data, which allows the analysis of different capture types under different settings.

## 2.2 PROCESSING TECHNIQUES

Analysis of raw ultrasonic data obtained from a testing, such as A-scan signals and B-scan images, can be difficult, and signal processing techniques are necessary to obtain more accurate representations of the test object. In ultrasonic imaging, data processing techniques aim to recover a map of the acoustic reflectivity of the object under testing, from the recorded A-scan signals. This map is seen as an image of the internal structure of the object, and these processing techniques are commonly referred to as *image reconstruction algorithms* or *imaging algorithms*. The image reconstruction process is also commonly referred to as *beamforming*, while the reconstructed images are also referred to as *focused image*.

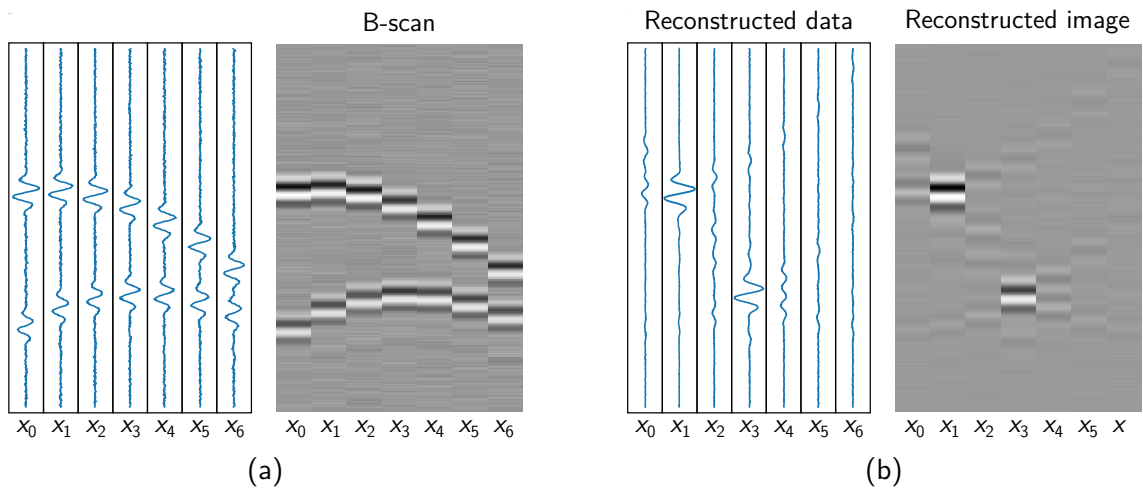


**Figure 17: Ultrasonic data (a) before and (b) after processing. Before processing, the B-scan image obtained from the A-scan signals is difficult to interpret, due to spreading of the echo signals. After processing, it is possible to identify the position of the origin of the echo signals more accurately.**

Figure 17 shows ultrasonic data before and after processing. Figure 17a illustrates the raw A-scan signals and the corresponding B-scan image. The A-scan signals are dispersed, owing to the aperture of the transducer, and it is difficult to determine the location of the flaws generating the observed echo signals. The task of an algorithm is to process the ultrasonic data such that the ultrasonic signals are focused. The main goal is to concentrate, or focus, the ultrasonic data, as shown in Figure 17b. Ideally, the echo signals are concentrated on the position in which they were originated.

Classical time-domain algorithms are based on the DAS approach and involves the coherent sum of samples along hyperbolas, which are given by the propagation time of the ultrasonic waves. DAS-based algorithms process the ultrasonic samples directly in the time-domain, and the DAS concept has been adapted to process data from capture modes such as sweeping, FMC and PWI, leading to the SAFT, TFM and coherent plane-wave compounding (CPWC) algorithms (LINGVALL et al., 2003; HOLMES et al., 2005; MONTALDO et al., 2009). Frequency-domain algorithms process the frequency spectrum of the ultrasonic echo signals. Classical frequency-domain algorithms are based on Stolt's migration (STOLT, 1978) and these algorithms solve the wave propagation problem under certain assumptions (STEPINSKI, 2007; HUNTER et al., 2008; GARCIA et al., 2013). Since ultrasonic data involves both temporal ( $\omega$ ) and spatial frequency ( $k$ ), frequency-domain algorithms are often referred to as  $\omega k$  algorithms.

The main disadvantage of DAS-based algorithms is the number of operations required to reconstruct an image, since it is necessary to compute the distance between each point on the object and each position of the transducer. Frequency-domain algorithms have been shown to have computational complexity lower than time-domain algorithms, which translates

**Table 1: Classical time-domain and frequency-domain algorithms for the sweep, FMC and PWI capture modes.**

Capture mode	Time-domain algorithm	Frequency-domain algorithm
Sweep	SAFT (LINGVALL et al., 2003)	$\omega k$ -SAFT (STEPINSKI, 2007)
FMC	TFM (HOLMES et al., 2005)	Wavenumber (HUNTER et al., 2008)
PWI	CPWC (MONTALDO et al., 2009)	$\omega k$ -CPWC (GARCIA et al., 2013)

to algorithms with a lower execution time (GARCIA et al., 2013; HUNTER et al., 2008).

In this section, three classical frequency-domain algorithms are presented. Each algorithm corresponds to a different capture mode, and the sweep, FMC and PWI capture modes are considered in this study. The classical time-domain algorithms for these capture modes are presented in Appendix A. Table 1 summarizes the classical time-domain and frequency-domain algorithms for each capture mode. For each algorithm, the reconstructed image is compared to the B-scan image generated by the corresponding capture mode. Inspection data used for processing are from an ultrasonic testing, simulated with the CIVA software. The specimen used for simulation was a steel block of 80 mm of length, 60 mm of height and 25 mm of depth, as shown in Figure 18. The specimen has two side-drilled holes (SDHs), positioned in  $(x_1, z_1) = (40, 40)$  mm and  $(x_2, z_2) = (33, 37)$  mm, with diameters of 1 mm and 2 mm; respectively. The origin for the coordinate system is considered as the upper left corner of the specimen. The transducer used during FMC and PWI simulations was a linear array with 64 elements, central frequency of 5 MHz, pitch of 0.3 mm and sampling frequency of 170 MHz. For sweeping tests, a circular monostatic transducer of diameter 6.35 mm was used. In this case, the transducer was positioned on the same coordinates than the elements of the linear array.

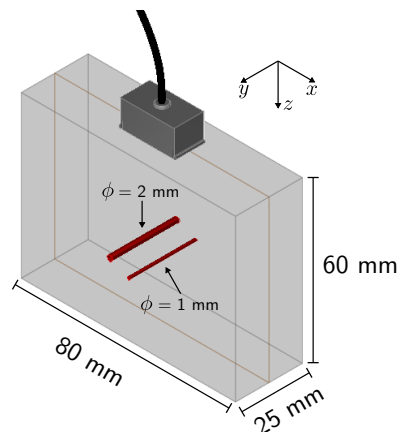


**Figure 18: Specimen used for simulation of ultrasonic data, for tests with monostatic transducers and linear arrays.**

### 2.2.1 $\omega k$ -SAFT

Frequency-domain algorithms are based on analytical solutions to the wave propagation problem. Usually, these solutions involve inverse problems, which are often ill-posed and require regularization in order to achieve practical solutions (MARGRAVE; LAMOUREUX, 2019). Different regularization lead to different algorithms and Stolt's migration is one of the most common approaches to obtain a solution which is numerically efficient to implement (STOLT, 1978; MARGRAVE; LAMOUREUX, 2019; SKJELVAREID et al., 2011). Originally developed for seismic imaging, Stolt's migration is one of the fastest migration methods available. In seismology, migration is the process by which seismic events are geometrically re-located in either space or time to the location the event occurred in the subsurface rather than the location that it was recorded at the surface, creating a more accurate image of the subsurface. The method consists of linking the spectrum of the acquired data to the spectrum of the reconstructed image, which are shown to be related via a nonlinear mapping. The main advantage of the algorithm is the formulation of integrals as Fourier transforms, which can be efficiently obtained on a numerical data set with the Fast Fourier Transform (FFT) algorithm.

Stolt's migration, adapted to ultrasonic imaging, has computational complexity lower than DAS-based methods, which has prompted its adaptation to imaging with monostatic and phased array transducers. In this section, the adaptation of Stolt's algorithm for ultrasonic imaging with monostatic transducers is presented. This algorithm is commonly referred to as  $\omega k$ -SAFT (STEPINSKI, 2007).

Stolt's migration is based on the exploding reflector model (ERM) (CLAERBOUT, 1985), illustrated in Figure 19. In the conventional pulse-echo setting with monostatic transducers, indicated in a Figure 19a, a transducer generates sound waves at  $t = 0$  that propagate through an object with travel speed  $c$ . Echo signals are produced by flaws in the object and travel back to the surface, where they are recorded by the transducer. In the exploding reflector model, show in in Figure 19b, flaws inside the object are assumed to produce sound waves at  $t = 0$ , i.e., the flaws become secondary sources and emit sound waves, which travel to the surface with propagation speed  $\hat{c}$  and are recorded by the transducer. The main advantage of the ERM is that the wave propagation model is reduced from a two-way propagation problem to a one-way propagation problem.

In the ERM, the main goal is to obtain the wavefield distribution at the time of explosion from knowledge of the recorded wavefield distribution at the surface. In other words, if  $\psi(x, z, t)$  is the acoustic wavefield distributed in the lateral position  $x$ , depth  $z$  and time  $t$ , the recorded echo data represents the wavefield at the surface, i.e.,  $\psi(x, z = 0, t)$ , and the objective is to find the wavefield at the time of explosion, i.e.,  $\psi(x, z, t = 0)$ , which represents

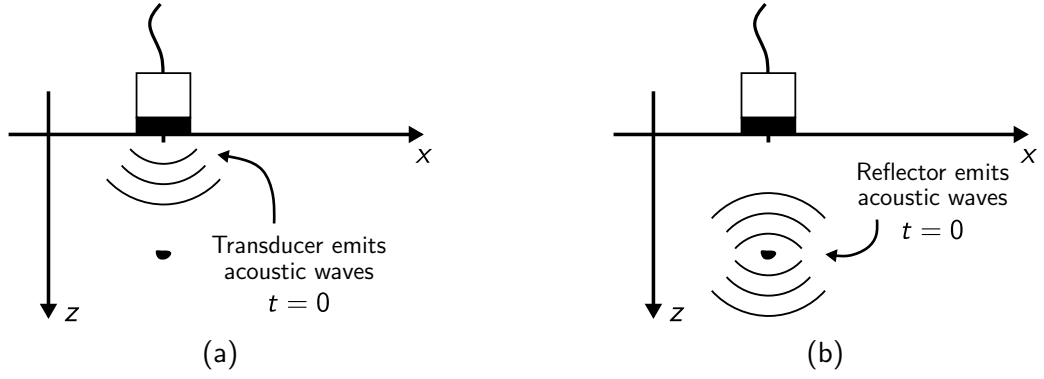


**Figure 19: (a) Pulse echo model and (b) ERM. In the conventional pulse-echo setting, the transducer emits acoustic waves with travel speed  $c$  at  $t = 0$ , whereas in the ERM, the reflectors are assumed to generate acoustic waves with travel speed  $\hat{c}$  at  $t = 0$ .**

an image of the object. Based on the ERM, the development of Stolt's migration consists on manipulating the frequency spectrum of  $\psi(x, z, t)$ , in order to obtain a solution to the wave equations using Fourier transforms. This leads to an efficient numerical implementation of the method, since Fourier transforms can be efficiently evaluated with the FFT algorithm. Let  $\psi(x, z, t)$  be a scalar wavefield, which satisfies the wave equation:

$$\nabla^2 \psi - \frac{1}{\hat{c}^2} \frac{\partial^2 \psi}{\partial t^2} = 0, \quad (1)$$

where  $\hat{c}$  is the ERM wave propagation velocity. If  $\Psi(k_x, z, f)$  is the frequency spectrum of  $\psi(x, z, t)$ ,  $\psi$  e  $\Psi$  and related via the inverse Fourier transform:

$$\psi(x, z, t) = \iint \Psi(k_x, z, f) e^{j2\pi(k_x x - ft)} dk_x df, \quad (2)$$

where  $j = \sqrt{-1}$ ,  $k_x$  is the spatial frequency related to  $x$ ,  $f$  is the temporal frequency related to  $t$  and the depth-axis  $z$  remains unchanged. The inverse Fourier transform expressed in (2) uses a negative sign convention for the temporal axis. This is to represent a wave traveling in the positive direction of  $x$  as the time  $t$  increases (MARGRAVE; LAMOUREUX, 2019). Further details on sign conventions for direct and inverse Fourier transforms can be found in the literature (BAUCK, 2019; CHONG, 2016; Stanford Exploration Project, 1998).

Substitution of (2) in (1) results in:

$$\iint \left[ \frac{\partial^2 \Psi(k_x, z, f)}{\partial z^2} + 4\pi^2 \left( \frac{f^2}{\hat{c}^2} - k_x^2 \right) \Psi(k_x, z, f) \right] e^{j2\pi(k_x x - ft)} dk_x df = 0. \quad (3)$$

In the case where the velocity  $\hat{c}$  is constant, the term in brackets in (3) has the form of an inverse Fourier transform. Due to the correspondence property of the Fourier transform, if a function is zero in its domain, its spectrum must also be zero, which leads to (MARGRAVE;

LAMOUREUX, 2019):

$$\frac{\partial^2 \Psi(k_x, z, f)}{\partial z^2} + 4\pi^2 k_z^2 \Psi(k_x, z, f) = 0, \quad (4)$$

where

$$k_z^2 = \frac{f^2}{\hat{c}^2} - k_x^2. \quad (5)$$

From this formulation, the problem consists in finding a function  $\Psi(k_x, z, f)$  which is a solution to (4). If a solution is found, the wavefield  $\psi(x, z, t)$  can be determined from the inverse Fourier transform of  $\Psi(k_x, z, f)$ . A possible solution has the form:

$$\Psi(k_x, z, f) = A(k_x, f)e^{j2\pi k_z z} + B(k_x, f)e^{-j2\pi k_z z}, \quad (6)$$

where  $A(k_x, f)$  and  $B(k_x, f)$  are constants to be determined. To determine the two constants, two initial conditions are necessary. However, the only initial condition available is the wavefield spectrum at the surface, i.e.,  $\Psi(k_x, z = 0, f)$ . To overcome this problem, the reflectors are assumed to emit acoustic waves only in the  $-z$  direction (MARGRAVE; LAMOUREUX, 2019). From this,  $A = 0$  and:

$$B = \Psi_0(k_x, f) = \Psi(k_x, z = 0, f). \quad (7)$$

It is important to note that  $\Psi_0(k_x, f)$  can be easily obtained, since it is the Fourier transform of  $\psi(x, z = 0, t)$ , namely, the Fourier transform of the A-scan data. A complete solution to the wave  $\psi(x, z, t)$  is then given by:

$$\psi(x, z, t) = \iint \Psi_0(k_x, f) e^{j2\pi(k_x x - k_z z - ft)} dk_x df, \quad (8)$$

which, for  $t = 0$ , becomes:

$$\psi(x, z, t = 0) = \iint \Psi_0(k_x, f) e^{j2\pi(k_x x - k_z z)} dk_x df. \quad (9)$$

In (9), one of the integrals has the form of a inverse Fourier transform and, hence, can be efficiently obtained on a numerical data set with the FFT algorithm. Stolt's migrations consists in manipulating (9) such that both integrals can be obtained with the FFT. From (5),  $k_z$  and  $f$  are related such that:

$$f(k_z) = \hat{c} \sqrt{k_x^2 + k_z^2}, \quad (10)$$

$$df = \frac{k_z \hat{c}}{\sqrt{k_x^2 + k_z^2}} dk_z, \quad (11)$$

which allows to write (9) as:

$$\psi(x, z, t = 0) = \iint \hat{\psi}(k_x, k_z) e^{j2\pi(k_x x - k_z z)} dk_x dk_z, \quad (12)$$

where  $\hat{\psi}$  is the spectrum of the wavefield at the time of explosion, given by:

$$\hat{\psi}(k_x, k_z) = \frac{\hat{c}k_z}{\sqrt{k_x^2 + k_z^2}} \psi_0(k_x, f(k_z)). \quad (13)$$

Equation (12) has the form of a inverse Fourier transform of  $\hat{\psi}(k_x, k_z)$ , which can be efficiently obtained with the FFT algorithm. In (9),  $\psi_0(k_x, f)$  represents the spectrum of  $\psi(x, z = 0, t)$ , namely, the Fourier transform of the A-scan signals. Since A-scan signals are discrete, the spectrum of the echo data will also be discrete, containing only uniformly-spaced frequency points. However, the mapping from  $f$  to  $k_z$  requires samples of the frequency spectrum at  $f(k_z)$ , which is nonuniform and does not coincide with the samples obtained from the Fourier transform of the A-scan signals. The usual way to obtain these samples is to interpolate  $\hat{\psi}(k_x, k_z)$  on  $\psi_0(k_x, f)$  (STEPINSKI, 2007). The spectrum can be interpolated directly on the complex samples or in its amplitude and phase.

A graphical representation of Stolt's migration is shown in Figure 20. The acquired signals from an inspection represents the wavefield measured at the surface, i.e.,  $\psi(x, z = 0, t)$ , shown in Figure 20a. These signals are sampled in time and space, and are associated with the temporal ( $t$ ) and spatial ( $x$ ) axes. The measured wavefield has a representation in the frequency-domain, via the Fourier transform ( $\mathcal{F}$ ), as shown in Figure 20b. The frequency spectrum  $\Psi(k_x, z = 0, f)$  of the measured wavefield is associated with the temporal and spatial frequency axes ( $f$  and  $k_x$ , respectively). The spectrum of the measured wavefield is discrete, and only samples of the spectrum at certain  $f$  and  $k_x$  are known. The known samples are represented by the green circles in Figure 20b.

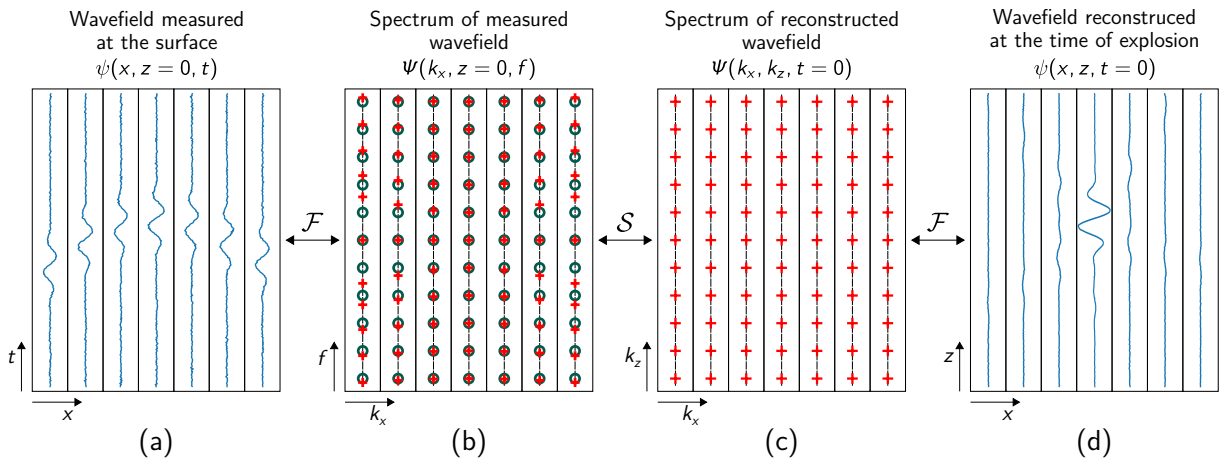


**Figure 20: Graphical representation of Stolt's migration.**

The reconstructed wavefield  $\psi(x, z, t = 0)$ , which is unknown *a priori*, is shown in Figure 20d. This wavefield, which is also discrete, is represented in the  $x$  and  $z$  spatial axes, and this wavefield also has a Fourier representation, as shown in Figure 20c. The frequency spectrum  $\Psi(k_x, k_z, t = 0)$  of the reconstructed wavefield is represented in the spatial frequency axes  $k_x$  and  $k_z$ . Considering that the  $x$  and  $z$  grids are regularly spaced, the frequency axes  $k_x$  and  $k_z$  are also regularly spaced, and these points are represented by red crosses in Figure 20c. In this case, it is assumed that the wavefield at the time of explosion is reconstructed on the same lateral positions as the measured wavefield.

Stolt's migration relates the spectrum of the measured wavefield to the spectrum of the reconstructed wavefield, as shown by the  $\mathcal{S}$  operator between Figures 20b and 20c. Samples of the unknown spectrum of the wavefield at the time of explosion are mapped to the known spectrum of the measured wavefield, through the relation given by (10). This is represented in Figure 20b, which shows the samples of the spectrum  $\Psi(k_x, k_z, t = 0)$ , represented by red crosses, mapped on the spectrum  $\Psi(k_x, z = 0, f)$ , given by the green circles. By interpolating on the known samples of  $\Psi(k_x, z = 0, f)$ , it is possible to obtain  $\Psi(k_x, k_z, t = 0)$ .

So far, it has been assumed that the wavefield at the time of explosion (or the image) is reconstructed on the same lateral positions as the acquired ultrasonic signals, i.e., the points on the  $x$ -axis of the image are the same as the points on the  $x$ -axis of the echo signals. This leads to the same points on the  $k_x$ -axis for both the spectrum of the measured wavefield and the spectrum of the reconstructed wavefield, as schematically shown in Figure 20. It is possible to have different points on the  $x$ -axis for both the echo data and the image. In this case, the values on the  $k_x$ -axis will differ for each spectrum, and interpolation on the  $k_x$ -axis on of the spectrum of the echo signals will be required.

Although the ERM considers that flaws are sources of acoustic waves, the actual data is obtained from the emission and reception of waves by the transducer. Hence, it is necessary to correct the wave propagation velocity to apply Stolt's migration to ultrasonic data (SKJELVAREID et al., 2011). In the conventional pulse-echo setting, the time  $t$  for the waves to travel from the transducer to a point on the object and back to the surface is given by  $t = 2d/c$ , where  $d$  is the distance between the point on the surface and the point on the object and  $c$  is the wave speed. In the ERM, the wave is emitted by the flaw and reaches the surface after a time  $t' = d/\hat{c}$ . For the two models to be compatible, the propagation time must be the same, which leads to  $\hat{c} = c/2$ .

From this development, Stolt's migration can be synthesized in Algorithm 1. The algorithm requires as input the points on the object where the image is desired (vectors  $x$  and  $z$ , of size  $N_x$  and  $N_z$ ; respectively), the matrix containing the A-scan signals (matrix  $s$ , of size

---

**Algorithm 1** Pseudocode for the  $\omega k$ -SAFT algorithm.
 

---

**Require:**  $x$  (a vector of size  $N_x$ ),  $z$  (a vector of size  $N_z$ ),  $s$  (a matrix of size  $(N_t, N_{x_t})$ ),  $x_t$  (a vector of size  $N_{x_t}$ ),  $t$  (a vector of size  $N_t$ ),  $c$  (a scalar)

**Ensure:**  $o$  (a matrix of size  $(N_z, N_x)$ )

```

1: function FREQS( $N, d_N$ )
2:   return  $\frac{1}{Nd_N} [-\frac{N}{2} \quad -\frac{N}{2} + 1 \quad \dots \quad \frac{N}{2} - 2 \quad \frac{N}{2} - 1]$ 
3: end function
4:  $dt \leftarrow t[1] - t[0]$ 
5:  $dx_t \leftarrow x_t[1] - x_t[0]$ 
6:  $dx \leftarrow x[1] - x[0]$ 
7:  $dz \leftarrow z[1] - z[0]$ 
8:  $f \leftarrow \text{FREQS}(N_t, dt)$ 
9:  $k_{x_t} \leftarrow \text{FREQS}(N_{x_t}, dx_t)$ 
10:  $k_x \leftarrow \text{FREQS}(N_x, dx)$ 
11:  $k_z \leftarrow \text{FREQS}(N_z, dz)$ 
12:  $\hat{c} \leftarrow c/2$ 
13:  $S \leftarrow \text{fft\_2D}(s)$ 
14: for  $j = 0, 1, \dots, N_x - 1$  do
15:    $k_{x_{\text{mig}}} \leftarrow k_x[j]$ 
16:   for  $i = 0, 1, \dots, N_z - 1$  do
17:      $f_{\text{mig}} \leftarrow \text{sgn}(k_z[j]) \hat{c} \sqrt{k_x[j]^2 + k_z[j]^2}$  ▷  $\text{sgn}$  is the sign function
18:      $\hat{S}[i, j] \leftarrow \text{interpolate}((k_{x_t}, f), (k_{x_{\text{mig}}}, f_{\text{mig}}), S)$ 
19:   end for
20: end for
21:  $o \leftarrow \text{ifft\_2D}(\hat{S})$ 

```

---

$(N_t, N_{x_t})$ ), the positions where the transducer acquired the A-scan signals (vector  $x_t$ , of size  $N_{x_t}$ ) and the sampling instants of the time samples ( $t$ , a vector of size  $N_t$ ), and the wave speed ( $c$ , a scalar). The output is the focused image (matrix  $o$ , of size  $(N_x, N_z)$ ).

The algorithm can be divided in three phases. First, in lines 1–13, the necessary parameters are determined. These parameters are the sampling periods ( $dt$ ,  $dx_t$ ,  $dx$  and  $dz$ ) and the corresponding spatial/temporal frequencies ( $f$ ,  $k_{x_t}$ ,  $k_x$  and  $k_z$ ), the wave speed for the ERM ( $\hat{c}$ ) and the spectrum of the echo data (complex-valued matrix  $S$ ). The spectrum of the wavefield at the time of explosion is reconstructed next, on lines 14–20. For every spatial frequency composing the vectors  $k_x$  and  $k_z$ , the corresponding  $k_{x_{\text{mig}}}$  and  $f_{\text{mig}}$  frequencies are determined and the spectrum of the A-scan signals ( $S$ ) is interpolated in those values, where the pair  $(k_x, f)$  is the known spatial and temporal frequencies of  $S$  and the pair  $(k_{x_{\text{mig}}}, f_{\text{mig}})$  contains the query points. The final phase is to obtain the inverse Fourier transform of the reconstructed spectrum, in order to obtain the reconstructed image (matrix  $o$ ).

In Algorithm 1, the interpolation step is only symbolically represented by a generic interpolation function. This interpolation could be piecewise linear, quadratic, sinc-based, or any interpolating function. The most common approach is to use an oversampling factor when

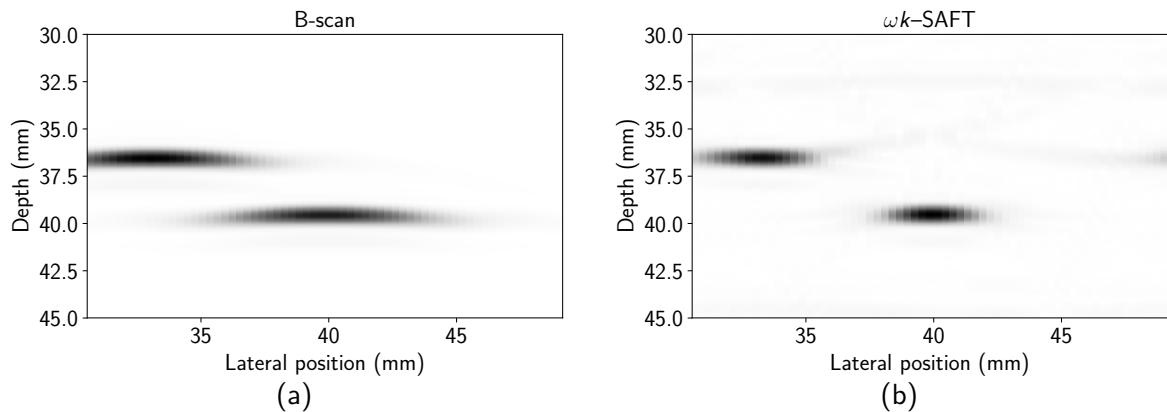


**Figure 21: (a) B-scan image and (b) image obtained with the  $\omega k$ -SAFT algorithm. After processing, the flaws are less dispersed around their respective locations.**

taking the FFT of the echo signals (line 13 of Algorithm 1) and piecewise interpolation for the interpolation step. It is worth nothing that interpolation may be required for both the spatial and temporal axis, if the vectors  $x$  and  $x_t$  are numerically different. Oversampling is used for both axis in this case; however, the oversampling factor need not be the same.

Figure 21 shows a comparison between the B-scan image and the image reconstructed with the  $\omega k$ -SAFT algorithm. The A-scan data used in this example is from the CIVA simulator, with data from the simulation of a monostatic transducer used to inspect the specimen previously shown in Figure 18. As Figure 21 shows, the image reconstructed by the  $\omega k$ -SAFT algorithm is less dispersed than the B-scan image.

Despite the common use of linear and phased array systems, several studies have focused on the development of frequency-domain processing techniques for monostatic transducers (OLOFSSON, 2010; SKJELVAREID et al., 2011; QIN et al., 2014; LUKOMSKI, 2014). The  $\omega k$ -SAFT was adapted from Stolt's migration, initially developed for seismic imaging and, in its development, the wave speed must be constant. Olofsson (2010) demonstrated that it is possible to use the phase shift migration (PSM) method, also initially developed for seismology, for ultrasound. The PSM method allows for a variable wave speed. In the work developed by Skjelvareid et al. (2011), the authors proposed an algorithm that combines the  $\omega k$ -SAFT with the PSM algorithm, obtaining images from objects consisting of layers of different materials. However, in both cases, the interface between two media is considered as plane. In the work developed by Qin et al. (2014), the authors generalized the PSM algorithm for non-plane interfaces and, with the same purpose, Lukomski (2014) proposed an algorithm for imaging of multi-layered objects with complex geometries.

## 2.2.2 Wavenumber

The lower computational complexity of frequency-domain algorithms, when compared to DAS-based methods, have prompted its development beyond ultrasonic imaging with monostatic transducers. Since linear array transducers are now commonplace in NDT inspections, the concept of Stolt's migration has been adapted to acquisition modes with these types of transducers (HUNTER et al., 2008; STEPINSKI, 2007; CHANG; CHERN, 2000). In this section the Wavenumber algorithm, developed for imaging with linear array transducers, is presented.

The Wavenumber algorithm aims to reconstruct an ultrasonic image with data obtained from an FMC. The algorithm proposes a solution to the wave propagation problem, based on a simplified model of 2-D wave propagation and the development of the method is based on the representation illustrated in Figure 22. Element  $u$ , located at  $(u, 0)$ , is responsible for emitting an ultrasonic wave into the medium, while element  $v$ , located at  $(v, 0)$ , receives echo signals. The echo signal received by element  $v$ , resulting from emission of element  $u$ , is identified as  $s(t, u, v)$ . Signal  $s(t, u, v)$  can also be represented by its temporal-frequency spectrum:

$$s(t, u, v) = \int S(\omega, u, v) e^{j\omega t} d\omega. \quad (14)$$

where  $\omega = 2\pi f$ , and  $f$  is the temporal frequency. In this case, the inverse Fourier transform uses a positive sign convention for the temporal axis, which differs from formulation of the  $\omega k$ -SAFT algorithm. This is for consistency with the cited work (HUNTER et al., 2008).

The echo signal received by a transducer depends on the distribution  $f(x, z)$  of the reflectors contained in the object, and  $S(\omega, u, v)$  can be modeled as:

$$S(\omega, u, v) = \iint f(x, z) G(\omega, x - u, z) G(\omega, x - v, z) dx dz, \quad (15)$$

where  $G(\omega, x, z)$  describes the wave propagation by decomposition of the 2-D Green function

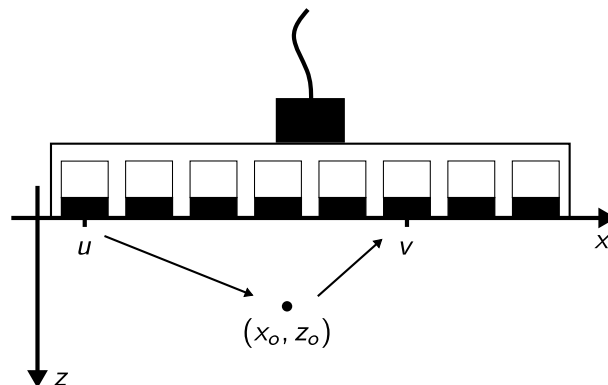


Figure 22: Representation of the transducer and flaw, for the Wavenumber algorithm.

into plane-waves, given by:

$$G(\omega, x, z) = -\frac{j}{4\pi} \int \frac{e^{jk_x x - j|z|\sqrt{(\omega/c)^2 - k_x^2}}}{\sqrt{(\omega/c)^2 - k_x^2}} dk_x, \quad (16)$$

which, substituted in (15) leads to:

$$S(\omega, u, v) = -\frac{1}{(4\pi)^2} \iint \frac{e^{jk_u u + jk_v v}}{\sqrt{(\omega/c)^2 - k_u^2} \sqrt{(\omega/c)^2 - k_v^2}} \left[ \iint f(x, z) e^{-j(k_u + k_v)x - j(\sqrt{(\omega/c)^2 - k_u^2} + \sqrt{(\omega/c)^2 - k_v^2})z} dx dz \right] dk_u dk_v. \quad (17)$$

The term in brackets in (17) represents the Fourier transform of the spatial distribution of the reflectors, for  $k_x = k_u + k_v$  and  $k_z = \sqrt{(\omega/c)^2 - k_u^2} + \sqrt{(\omega/c)^2 - k_v^2}$ , which represents Stolt's migration. Hence, if  $F(k_x, k_z)$  is the Fourier transform of  $f(x, z)$ ,  $S(\omega, u, v)$  can be written as (HUNTER et al., 2008):

$$S(\omega, u, v) = \iint \left[ \frac{1}{(4\pi)^2} \frac{F\left(k_u + k_v, \sqrt{(\omega/c)^2 - k_u^2} + \sqrt{(\omega/c)^2 - k_v^2}\right)}{\sqrt{(\omega/c)^2 - k_u^2} \sqrt{(\omega/c)^2 - k_v^2}} \right] e^{jk_u u + jk_v v} dk_u dk_v. \quad (18)$$

Expression (18) has the form of an inverse Fourier transform, such that the term in brackets is the inverse Fourier transform of  $S(\omega, u, v)$ , namely:

$$S(\omega, k_u, k_v) = -\frac{1}{(4\pi)^2} \frac{F\left(k_u + k_v, \sqrt{(\omega/c)^2 - k_u^2} + \sqrt{(\omega/c)^2 - k_v^2}\right)}{\sqrt{(\omega/c)^2 - k_u^2} \sqrt{(\omega/c)^2 - k_v^2}}. \quad (19)$$

Equation (19) relates the spectrum of the echo signals,  $S(\omega, k_u, k_v)$ , to the spectrum of the distribution of the reflectors,  $F(k_x, k_z)$ . Since the echo signals are known (which are the A-scan signals recorded by the transducer), its spectrum is easily obtained with the Fourier transform of the FMC data set, and the distribution of the reflectors could be obtained from (19). The main restriction is that  $F$  is not expressed directly in terms of  $k_x$  and  $k_z$ . Expression of  $F$  in terms of  $k_x$  and  $k_z$  is imperative, since the image space,  $x$  and  $z$ , is previously defined and is associated with  $k_x$  and  $k_z$ . This requires that the relation:

$$k_x = k_u + k_v, \quad (20)$$

$$k_z = \sqrt{(\omega/c)^2 - k_u^2} + \sqrt{(\omega/c)^2 - k_v^2}, \quad (21)$$

be inverted, such that  $F$  can be expressed in terms of  $k_x$  and  $k_z$ . However, the mapping from  $\omega, k_u$  and  $k_v$  to  $k_x$  and  $k_z$  is not unique. This issue is resolved if one of the parameters ( $\omega, k_u$  or  $k_v$ ) is considered as constant. If  $k_u$  is considered as constant, the inverse mapping is obtained as (HUNTER et al., 2008):

$$k_v = k_x - k_u, \quad (22)$$

$$\omega = c \frac{\sqrt{k_z^4 + 2(k_u^2 + (k_x - k_u)^2)k_z^2 + k_u^4 + (k_x - k_u)^4 - 2k_u^2(k_x - k_u)^2}}{2k_z}. \quad (23)$$

Thus, for a specific  $k_u$ , the spectrum  $F(k_x, k_z)$  of the spatial distribution of the flaws can be obtained from (19). In this case, the spectrum obtained corresponds to the emission of only a single element, while all other elements are receivers, and a final spectrum can be obtained from the combination of the spectra of all emitters. Then, the final focused image can be reconstructed via the inverse Fourier transform of the resulting spectrum (HUNTER et al., 2008).

Algorithm 2 presents a pseudocode for the Wavenumber algorithm. The Wavenumber algorithm requires as inputs the locations on the object where the image is desired (vectors  $x$  and  $z$ , of size  $N_x$  and  $N_z$ ; respectively), the FMC data set (matrix  $s$ , of size  $(N_t, N_{x_t}, N_{z_t})$ ), the geometric locations of the elements of the transducer (vector  $x_t$ , of size  $N_{x_t}$ ), the sampling instants of the time samples ( $t$ , a vector of size  $N_t$ ) and the wave propagation velocity (scalar  $c$ ). The output (matrix  $f$ ) is the image reconstructed from the FMC data.

The algorithm can be divided in three parts. First, in lines 1–14, the sampling periods ( $dt$ ,  $dx_t$ ,  $dx$  and  $dz$ ) and the corresponding spatial/temporal frequencies ( $f$ ,  $k_u$ ,  $k_v$ ,  $k_x$  and  $k_z$ ) are obtained, a 3-D FFT is applied to the FMC data set and the matrix which will hold the accumulated spectrum is initialized with zeros. Next, through lines 15–24, the algorithm loops for each  $k_u$ , corresponding to each element that emitted a wave. The spectrum  $S_r$  of the corresponding  $k_u$  is extracted from the spectrum of the echo signals and, for each value of  $k_x$  and  $k_z$ , the corresponding  $k_{v_{\text{mig}}}$  and  $f_{\text{mig}}$  frequencies are obtained. These values are then interpolated on the spectrum  $S_r$  and the result is accumulated in the matrix  $F$ . The interpolation step is only symbolically represented with a generic function. It is common to use piecewise linear interpolation, along with an oversampling factor on the 3-D FFT applied in the first phase of the algorithm. Moreover, as Algorithm 2 shows, a new spectrum is reconstructed for each  $k_u$  and is then accumulated in the matrix  $F$ . In essence, an image is reconstructed for each element of the transducer that emitted an ultrasonic pulse. In the last part, a 2-D inverse FFT is applied to the accumulated spectrum  $F$ , to obtain the reconstructed image ( $f$ ).

Figure 23 shows the images obtained for the B-scan and Wavenumber algorithm. The data used is from simulation of the specimen shown in Figure 18, using a linear array for the inspection. The B-scan image, shown in Figure 23a, corresponds to the A-scan signals obtained from the diagonal of the FMC data set. From the B-scan image, the internal structure of the object is unclear. With the Wavenumber algorithm, the flaws are accurately located, as indicated in Figure 23b.

---

**Algorithm 2** Pseudocode for the Wavenumber algorithm.
 

---

**Require:**  $x$  (a vector of size  $N_x$ ),  $z$  (a vector of size  $N_z$ ),  $s$  (a matrix of size  $(N_t, N_{x_t}, N_{z_t})$ ),  $x_t$  (a vector of size  $N_{x_t}$ ),  $t$  (a vector of size  $N_t$ ),  $c$  (a scalar)

**Ensure:**  $f$  (a matrix of size  $(N_z, N_x)$ )

```

1: function FREQS( $N, d_N$ )
2:   return  $\frac{1}{Nd_N} [-\frac{N}{2} \quad -\frac{N}{2} + 1 \quad \dots \quad \frac{N}{2} - 2 \quad \frac{N}{2} - 1]$ 
3: end function
4:  $dt \leftarrow t[1] - t[0]$ 
5:  $dx_t \leftarrow x_t[1] - x_t[0]$ 
6:  $dx \leftarrow x[1] - x[0]$ 
7:  $dz \leftarrow z[1] - z[0]$ 
8:  $f \leftarrow \text{FREQS}(N_t, dt)$ 
9:  $k_u \leftarrow \text{FREQS}(N_{x_t}, dx_t)$ 
10:  $k_v \leftarrow \text{FREQS}(N_{x_t}, dx_t)$ 
11:  $k_x \leftarrow \text{FREQS}(N_x, dx)$ 
12:  $k_z \leftarrow \text{FREQS}(N_z, dz)$ 
13:  $S \leftarrow \text{fft\_3D}(s)$ 
14:  $F \leftarrow \text{zeros}(N_x, N_z)$  ▷ Matrix of zeros, with size  $(N_x, N_z)$ 
15: for  $r = 0, 1, \dots, N_{x_t} - 1$  do
16:    $S_r \leftarrow S(f, k_u[r], k_v)$  ▷ Gets only the spectrum for a specific  $k_u$ 
17:   for  $j = 0, 1, \dots, N_x - 1$  do
18:      $k_{v_{\text{mig}}} \leftarrow k_x[j] - k_u[r]$ 
19:     for  $i = 0, 1, \dots, N_z - 1$  do
20:        $f_{\text{mig}} \leftarrow \text{wn\_mig}(k_u[r], k_x[j], k_z[i], c)$  ▷ According to (23)
21:        $F[i, j] \leftarrow F[i, j] + \text{interpolate}((k_{x_t}, f), (k_{v_{\text{mig}}}, f_{\text{mig}}), S_r)$ 
22:     end for
23:   end for
24: end for
25:  $f \leftarrow \text{ifft\_2D}(F)$ 

```

---

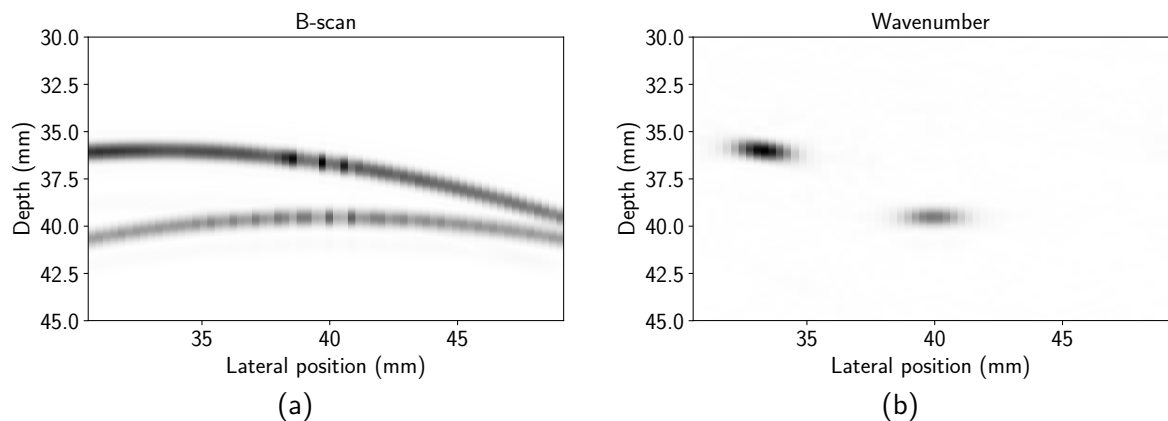


**Figure 23: (a) B-scan image generated with A-scan data from the diagonal of an FMC and (b) image reconstructed with the Wavenumber algorithm. The internal structure of the object is unclear from the B-scan image, whereas the image obtained with the Wavenumber algorithm allows to locate of the flaws more precisely.**

Initially, the Wavenumber algorithm was developed to process FMC data from contact inspections, with a plane surface between the transducer and the test piece. The wave propagation speed must also be constant. Recent studies have been proposed to overcome these limitations (LUKOMSKI, 2016; WU et al., 2016). In the work developed by Wu et al. (2016), the authors proposed an algorithm that process FMC data in the frequency domain for multi-layered media. The authors demonstrated the proposed algorithm on a block consisting of two different materials, leading to wave propagation with a variable speed. In the study conducted by Lukomski (2016), the authors proposed an algorithm which also allows materials with different media. The algorithm developed by the authors allows immersion testings and also considers objects with complex surfaces. A constraint of the aforementioned algorithms is the requirement of *a priori* knowledge on the layers involved. Moghimirad et al. (2016) directed their research on combining linear arrays with the concept of virtual sources. In this case, instead of triggering each element of the transducer, the elements are combined to emit focused waves. In their work, the authors were able to obtain images with the same quality as the TFM algorithm; however, with a 20-fold reduction in computational cost.

### 2.2.3 $\omega k$ -CPWC

The ERM is easily adapted to ultrasonic inspections using monostatic transducers, which requires only that the propagation speed of the waves emitted by the transducer is halved, i.e.,  $\hat{c} = c/2$ . The Wavenumber algorithm does not directly uses the ERM but Stolt's migration is used to adapt the integrals involved in the model into Fourier transforms. This leads to different equations for both the Wavenumber and  $\omega k$ -SAFT algorithms, which leads to different mapping functions.

Processing of PWI data in the frequency domain is more closely based on the  $\omega k$ -SAFT algorithm and the ERM. Adaptation of the PWI acquisition scheme to the ERM is achieved by considering emissions with different angles separately. While adaptation of ultrasonic data acquisition with monostatic transducer to the ERM requires only scaling of the wave velocity, adaptation of PWI requires also scaling and displacement of the image points, which is a function of the emitted plane-wave (GARCIA et al., 2013). PWI is adapted to ERM via the following transformations:

$$\begin{cases} \hat{c} = \alpha c, \\ \hat{z} = \beta z, \\ \hat{x} = x + \gamma z, \end{cases} \quad (24)$$

where the parameters  $\alpha$ ,  $\beta$  and  $\gamma$  are functions of the angle  $\theta$  and are given by:

$$\begin{cases} \alpha = \frac{1}{\sqrt{1 + \cos \theta + \sin^2 \theta}}, \\ \beta = \frac{\sqrt{(1 + \cos \theta)^3}}{1 + \cos \theta + \sin^2 \theta}, \\ \gamma = \frac{\sin \theta}{2 - \cos \theta}. \end{cases} \quad (25)$$

A pseudocode for the  $\omega k$ -CPWC is shown in Algorithm 3. The algorithm requires as input the locations on the object where the image is to be determined (vectors  $x$  and  $z$ , of size  $N_x$  and  $N_z$ ; respectively), the PWI data set (matrix  $s$ , of size  $(N_t, N_\theta, N_{x_t})$ ), the geometric locations of the elements of the transducer ( $x_t$ ), the sampling instants of the time samples ( $t$ , a vector of size  $N_t$ ), the set of angle used in the inspection (vector  $\theta$ , of size  $N_\theta$ ) and the wave propagation speed (scalar  $c$ ). The output is the focused image (matrix  $o$ , of size  $(N_z, N_x)$ ).

As the previous frequency-domain algorithms, the  $\omega k$ -CPWC starts by defining the sampling periods ( $dt$ ,  $dx_t$ ,  $dx$  and  $dz$ ) and the corresponding spatial/temporal frequencies ( $f$ ,  $k_{x_t}$ ,  $k_x$  and  $k_z$ ), as indicated in lines 1–11. Next, in lines 12–30, the algorithm loops for each emitting angle. For each emitting angle, the parameters  $\alpha$ ,  $\beta$  and  $\gamma$  are computed according to (25), as well as the ERM speed. The spectrum of the echo data is computed in two steps. First, a FFT is applied to the time-axis of the echo data corresponding to a single angle. The resulting spectrum is then phase-multiplied and another FFT is applied to the multiplied spectrum. This time, the FFT is applied to the spatial-axis. With the spectrum transformed in both axes, the frequencies are mapped according to Stolt's migration and the spectrum  $S$  is interpolated on these frequencies. After the interpolation step is completed, an inverse FFT is applied to the  $k_x$ -axis of the interpolated spectrum. The resulting spectrum is phase-multiplied to correct for the displacement of the image points and another inverse FFT is applied to the multiplied spectrum; this time, on the  $k_z$ -axis. The resulting image is accumulated to the compounded image  $o$ .

Figure 24 shows the results obtained with the  $\omega k$ -CPWC algorithm, used to process PWI data obtained from simulation of the specimen previously shown in Figure 18. For testing, a set of 21 angles was used, with an initial angle of  $-10^\circ$ , a final angle of  $10^\circ$  and a step of  $1^\circ$ . Since one image is reconstructed for each angle used, the final result consists of the compounding of these 21 partial images. As Figure 24a shows, the B-scan image, which corresponds to the A-scans signals obtained from emission with  $\theta = 0^\circ$ , is difficult to interpret. After processing with the  $\omega k$ -CPWC algorithm, location of the flaws can be more precisely determined, as indicated in Figure 24b.

---

**Algorithm 3** Pseudocode for the  $\omega k$ -CPWC algorithm.
 

---

**Require:**  $x$  (a vector of size  $N_x$ ),  $z$  (a vector of size  $N_z$ ),  $s$  (a matrix of size  $(N_t, N_\theta)$ ),  $x_t$  (a vector of size  $N_{x_t}$ ),  $t$  (a vector of size  $N_t$ ),  $\theta$  (a vector of size  $N_\theta$ ),  $c$  (a scalar)

**Ensure:**  $o$  (a matrix of size  $((N_z, N_x))$ )

```

1: function FREQS( $N, d_N$ )
2:   return  $\frac{1}{Nd_N} [-\frac{N}{2} \quad -\frac{N}{2} + 1 \quad \dots \quad \frac{N}{2} - 2 \quad \frac{N}{2} - 1]$ 
3: end function
4:  $dt \leftarrow t[1] - t[0]$ 
5:  $dx_t \leftarrow x_t[1] - x_t[0]$ 
6:  $dx \leftarrow x[1] - x[0]$ 
7:  $dz \leftarrow z[1] - z[0]$ 
8:  $f \leftarrow \text{FREQS}(N_t, dt)$ 
9:  $k_{x_t} \leftarrow \text{FREQS}(N_{x_t}, dx_t)$ 
10:  $k_x \leftarrow \text{FREQS}(N_x, dx)$ 
11:  $k_z \leftarrow \text{FREQS}(N_z, dz)$ 
12: for  $r = 0, 1, \dots, N_\theta - 1$  do
13:    $\alpha, \beta, \gamma \leftarrow \text{stolt\_params}(\theta[r])$  ▷ According to (25)
14:    $\hat{c} \leftarrow \alpha c$ 
15:    $S \leftarrow \text{fft}(s[t, \theta[r], x_t], \text{axis: } t)$  ▷ Transforms only the time-axis
16:    $S \leftarrow S \cdot e^{j2\pi f x \sin(\theta[i])/c}$  ▷ Element-wise multiplication
17:    $S \leftarrow \text{fft}(S, \text{axis: } x_t)$  ▷ Transforms only the spatial-axis
18:   for  $j = 0, 1, \dots, N_x - 1$  do
19:      $k_{x_{\text{mig}}} = k_x[j]$ 
20:     for  $i = 0, 1, \dots, N_z - 1$  do
21:        $\hat{k}_z \leftarrow \beta k_z[i]$ 
22:        $\hat{k}_x \leftarrow k_x[j]$ 
23:        $f_{\text{mig}} \leftarrow \text{sgn}(\hat{k}_z) \hat{c} \sqrt{\hat{k}_x^2 + \hat{k}_z^2}$  ▷  $\text{sgn}$  is the sign function
24:        $\hat{S}[i, j] \leftarrow \text{interpolate}((k_{x_t}, f), (k_{x_{\text{mig}}}, f_{\text{mig}}), S)$ 
25:     end for
26:   end for
27:    $\hat{s} \leftarrow \text{ifft}(\hat{S}, \text{axis: } k_x)$  ▷ Transforms only the  $k_x$ -axis
28:    $\hat{s} \leftarrow s_{\text{int}} \cdot e^{j2\pi \hat{k}_x \gamma z}$  ▷ Element-wise multiplication
29:    $\hat{s} \leftarrow \text{ifft}(\hat{s}, \text{axis: } k_z)$  ▷ Transforms only the  $k_z$ -axis
30:    $o \leftarrow o + \hat{s}$ 
31: end for

```

---

Different frequency domain algorithms have been proposed for acquisition with plane-waves. One example is the Ultrasound Fourier Slice (UFS) algorithm (BERNARD et al., 2014), which allows a better lateral resolution on the focused images, and the phase shift migration techniques, which allows variable wave propagation speeds (ALBULAYLI; RAKHMATOV, 2018). Recent studies have also been direct to unite the theory of compressed sensing to image reconstruction with PWI. Compressed sensing uses sparse techniques, as well as *a priori* knowledge of the signals being inferred, to obtain the same information with a lower number of measurements (CANDES; WAKIN, 2008). The use of compressed sensing

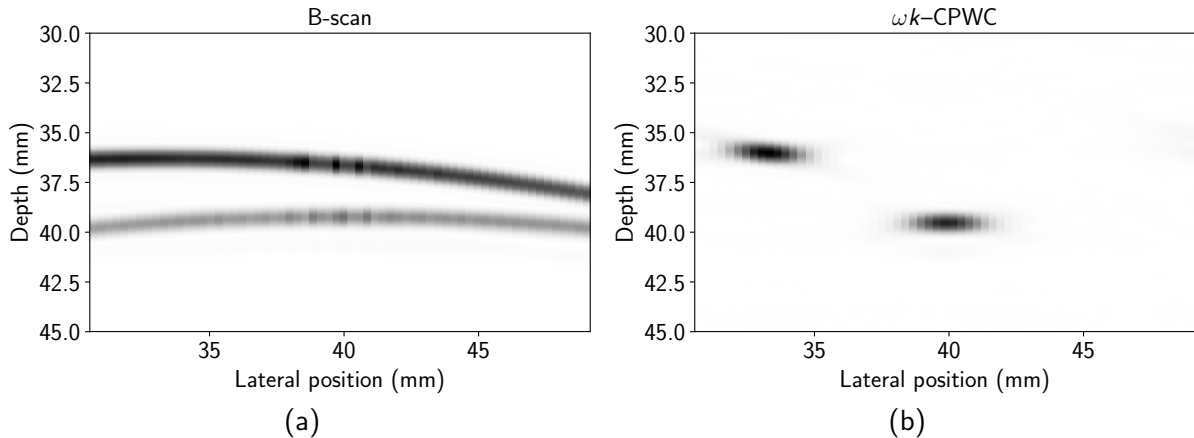


**Figure 24: (a) B-scan image and (b) image obtained with the  $\omega k$ -CPWC algorithm. The B-scan image, defined as the image obtained for an emission angle of  $\theta = 0^\circ$ , is difficult to interpret. After processing and compounding the set of 21 images with the  $\omega k$ -CPWC algorithm, location of the flaws can be more precisely determined.**

has also been evaluated for frequency-domain algorithms. Besson et al. (2016b) developed a framework for image reconstruction in the frequency-domain, suggesting that algorithms previously proposed could be improved with the use of sparse techniques.

### 2.3 REVIEW

This chapter presented a review on the principles of ultrasonic NDT, as well as a review of common frequency-domain processing techniques. Ultrasonic methods for NDT have been widely adopted in industry and are commonly used for medical imaging.

The first section of this chapter presented the pulse-echo method for ultrasonic NDT. Flaws inside a solid object can be identified from the reflection of ultrasonic waves emitted into it. Ultrasonic transducers are responsible for the emission and detection of the ultrasonic waves, and the first section of this chapter discusses monostatic and linear array transducers, as well as common acquisition schemes, such as sweep, FMC and PWI.

It is difficult to determine the internal structure of the inspected object from the raw ultrasonic signals, due to the transducer aperture. The second section of this chapter presented common frequency-domain algorithms for ultrasonic imaging. These algorithms aim to reconstruct an image representing the internal structure of the object from the echo signals recorded by the transducer. Frequency-domain algorithms are based on Stolt's migration and consists essentially of direct/inverse Fourier transforms and interpolation operations. An example of each algorithm was also presented, in order to demonstrate the reconstruction of an image from the raw ultrasonic signals.

### 3 INTERPOLATION-FREE STOLT MIGRATION

Stolt's migration provides a solution to the wave equation after reflections by formulating the forward propagation model in the frequency-domain and considering only waves traveling in the upward direction. In essence, Stolt's migration consists of applying a Fourier transform to the echo signals, interpolating the spectral data and applying the inverse Fourier transform to the interpolated spectrum. The interpolation step is responsible for performing Stolt's mapping and requires caution. If not performed correctly, the reconstructed image may not be focused and the result obtained may be a misleading representation of the inspected object. Simple interpolation schemes are computationally efficient but can degrade image quality, whereas more sophisticated interpolators improve image quality at the cost of a higher computational complexity (LEHMANN et al., 1999; KOKOLEV et al., 2009).

The common approach to perform Stolt's migration is to use an oversampled FFT, by zero-padding the time-domain echo signals, and piecewise linear interpolation in the frequency-domain. Zero-padding of the time-domain echo signals increases its spectral density, which alleviates interpolation of the resulting frequency-domain data. To illustrate the effect of zero-padding in a finite and discrete time-domain signal, consider the time and frequency-domain representation of a finite and discrete echo signal obtained from a flaw, shown in Figure 25. The discrete time-domain signal  $x(t)$  is shown in Figure 25a, while the magnitude of its frequency spectrum  $|X(\omega)|$  is shown in Figure 25b. The frequency spectrum is taken as the discrete Fourier Transform (DFT) of the discrete time-domain signal, which can be obtained with the FFT algorithm. In Stolt's migration, the spectrum shown in Figure 25b is interpolated to obtain the required frequency samples.

Zero-padding the time-domain signal oversamples its spectrum, increasing the spectral density, which is shown in Figure 26. Figure 26a shows the finite and discrete echo signal before and after zero-padding, represented by the signals  $x(t)$  and  $x'(t)$ ; respectively. In the example, the signal was padded with as many zeros as its original length, thus, doubling its samples and corresponding to an oversampling factor of 2. The effect of zero-padding on the spectrum is shown in Figure 26b, which shows the magnitude of the spectrum of the unpadded signal,  $|X(\omega)|$ , and the magnitude of the padded signal,  $|X'(\omega)|$ . As Figure 26b shows, the spectrum

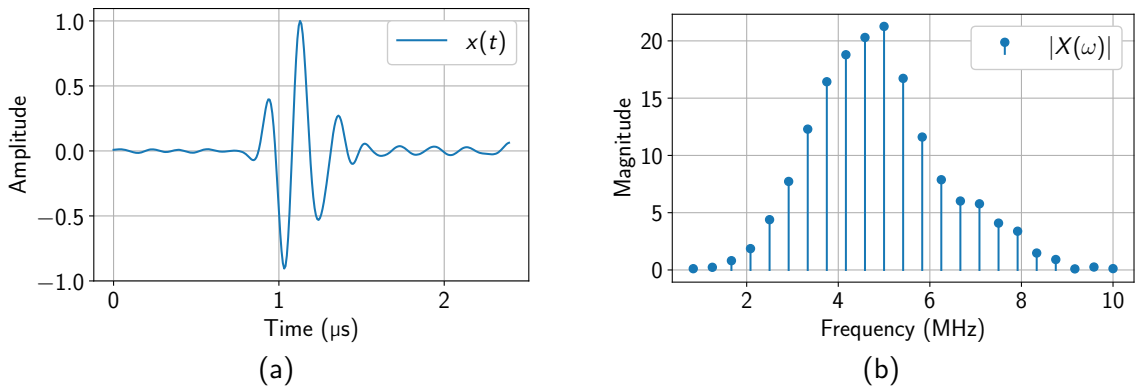


**Figure 25: (a) A-scan signal  $x(t)$  and (b) the magnitude of its spectrum  $|X(\omega)|$ .**

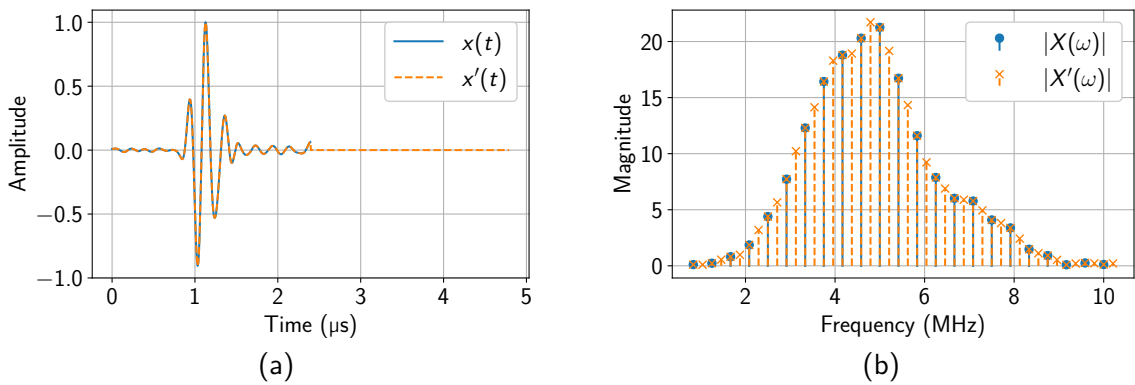


**Figure 26: (a) A-scan signals  $x(t)$  and  $x'(t)$  and (b) the magnitude  $|X(\omega)|$  and  $|X'(\omega)|$  of its spectra.**

of the padded signal contains the same samples as the spectrum of the unpadded signal, as well as new samples. These new samples, however, are actually interpolated from the original samples via sinc-based interpolation (LATHI, 2000). This interpolation process occurs when the FFT is applied to the padded signal, and its effect on the reconstruction of the image's spectrum is discussed in Appendix B. In this study, we refer the spectrum of the zero-padded signal as the oversampled FFT. The ratio between the number of time samples after zero-padding and the original number of time samples is referred to as the oversampling factor. The main disadvantage of using the oversampled FFT and piecewise linear interpolation is that extensive zero-padding of the data is required, leading to large values for the oversampling factor, and it is not uncommon to have data sets where over 75% of the samples are zeros (oversampling factor of 4). This affects processing time and the efficiency of the frequency-domain algorithm is degraded.

One approach to avoid the interpolation step required by Stolt's migration is with the Non-Uniform Fast Fourier Transform (NUFFT). The NUFFT allows to obtain the inverse Fourier transform directly on non-uniformly spaced frequency points, by using an oversampled FFT and linear interpolation with Kaiser-Bessel kernels (FESSLER; SUTTON, 2003; KRUI-

ZINGA et al., 2012). In the research conducted by Kruizinga et al. (2012), the authors were able to successfully use the NUFFT with a frequency-domain algorithm, processing ultrasonic data obtained from PWI. They compared several frequency-domain techniques, as well as the DAS approach, and concluded that the NUFFT can be used as a replacement for interpolation. In their results, they obtained gains in both image quality and computational complexity, obtaining an average reduction of 15% in execution time, with their proposed algorithm. However, in the NUFFT study, the authors consider a different migration method, known as Lu's method. This method differs from Stolt's migration in the solution to the wave equation, which leads to different mappings of the frequency data.

Another approach, demonstrated by Li et al. (2014) in the context of synthetic aperture radar (SAR), is the use of frequency shifts. Instead of interpolation, the authors proposed to shift the frequency spectrum in order to obtain the samples required to perform Stolt's migration. Using this approach on simulated data, they compared their proposed algorithm to zero-padding with sinc-based interpolation and showed that, although there were no gains in image quality, processing time was reduced by over 4 times.

In this chapter, the algorithm developed by Li et al. (2014) will be discussed. The adaptation and extension of their algorithm to ultrasonic imaging is also presented, which will later be used to replace the interpolation step required by the  $\omega k$ -SAFT, Wavenumber and  $\omega k$ -CPWC algorithms.

### 3.1 INTERPOLATION BY FREQUENCY SHIFTS

Interpolation by frequency shifts stems from the time/frequency-shift property of the Fourier transform. If a signal  $x(t)$  has Fourier transform  $X(\omega)$ , then multiplication of  $X(\omega)$  by  $e^{-j\omega t_0}$  advances the time signal by  $t_0$ , i.e.,  $x(t)$  becomes  $x(t - t_0)$  (LATHI, 2000).

This property is also valid for discrete signals. In this case, if a discrete signal  $x[n]$  has a discrete Fourier transform  $X[\Omega]$ , then, multiplication of  $X[\Omega]$  by  $e^{-j\Omega n_0}$  advances the original signal by  $n_0$  samples, i.e.,  $x[n]$  becomes  $x[n - n_0]$ . For discrete signals, the shifting property holds exactly when the delay  $n_0$  is an integer. When  $n_0$  is fractional, the signal  $x[n]$  is interpolated at  $x[n - n_0]$  with a trigonometric series (BAI; FENG, 2007).

Figure 27 illustrates a discrete signal and its corresponding frequency spectrum. Figure 27a shows a signal  $x[n] = \cos(2\pi f n T_s)$ , where  $f = 10$  Hz,  $n = 0, 1, \dots, 20$  and  $T_s = 0.01$  s, while Figures 27b and 27c show the magnitude and phase of its discrete Fourier transform  $X[\Omega]$ . In this case,  $x[n]$  is known only at time instants  $t = nT_s = 0, 0.01, \dots, 0.19$  s. Evaluation of this signal at time instants  $t' = t + \tau$ , where  $\tau = T_s/2$ , can be obtained by multiplying the spectrum  $X[\Omega]$  by  $e^{-j\Omega T_s/2}$ .

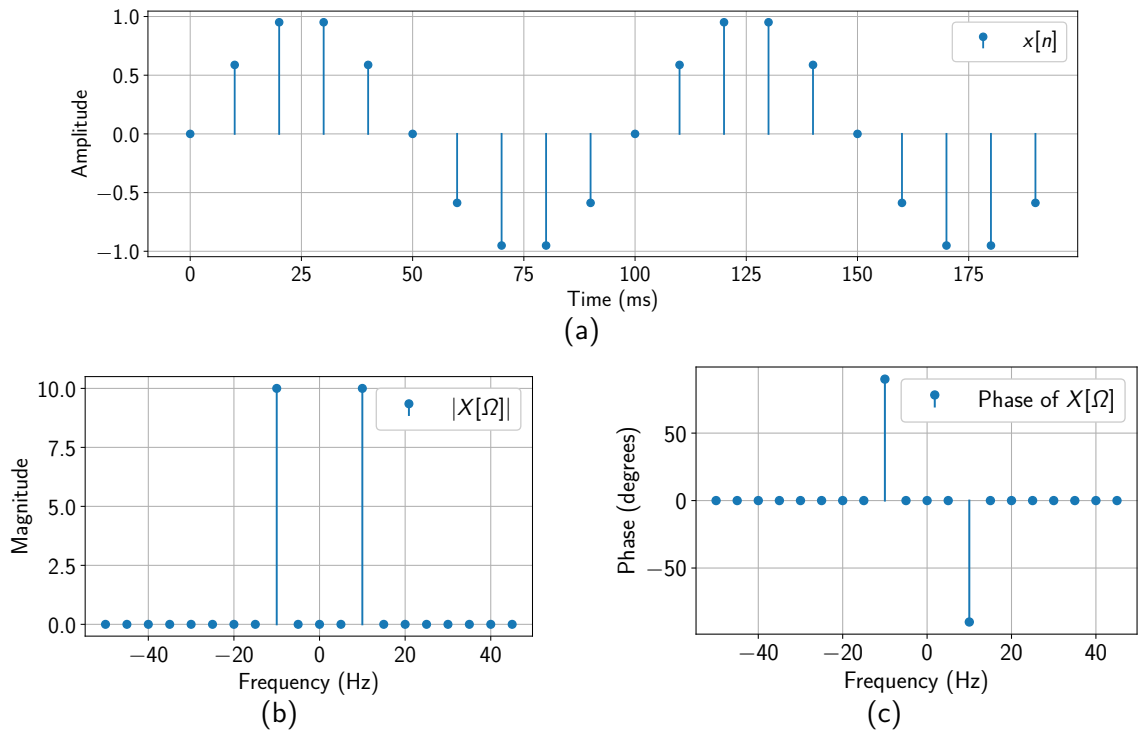


Figure 27: (a) Sequence  $x[n]$ , sampled at  $T = 0, 0.01, \dots, 0.19$  s. (b) The magnitude and (c) phase of its spectrum  $X[\Omega]$  are also shown.

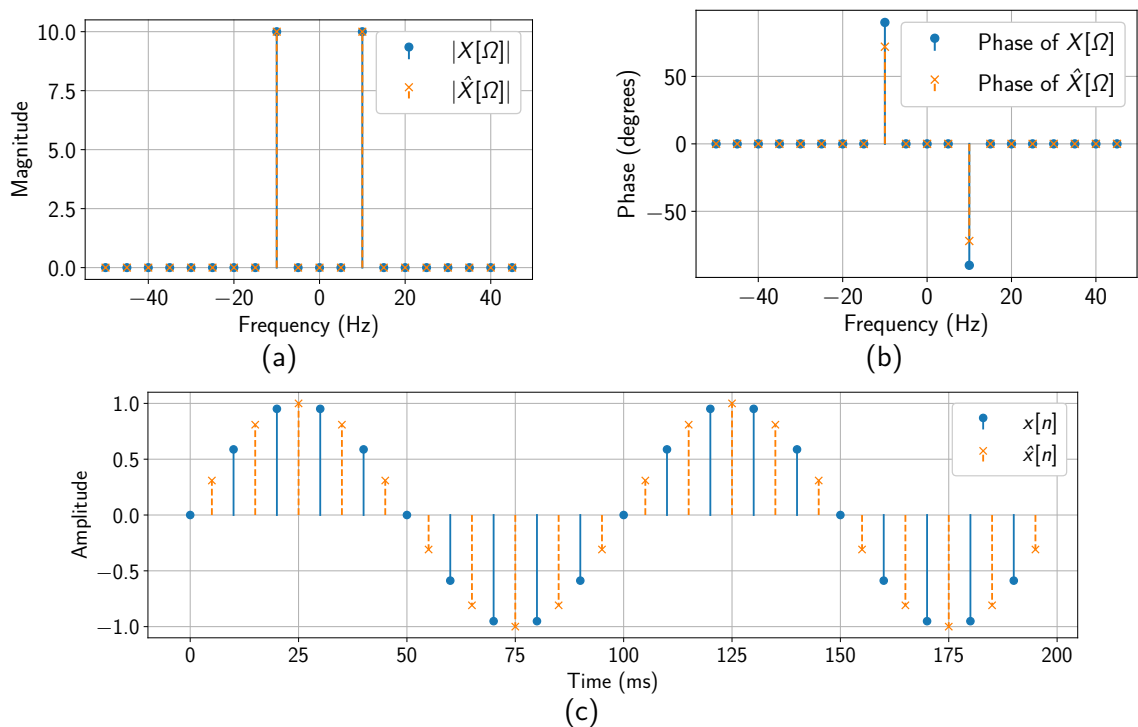


Figure 28: (a) Magnitude and (b) phase of the spectra  $X[\Omega]$  and  $\hat{X}[\Omega] = X[\Omega]e^{-j\Omega T_s/2}$ . Multiplication of  $X[\Omega]$  by a complex exponential changes only its phase, while the amplitude remains the same. (c) Sequences  $x[n]$  and  $\hat{x}[n]$ , corresponding to the spectra  $X[\Omega]$  and  $\hat{X}[\Omega]$ , respectively. Sequence  $x[n]$  is sampled at  $T = 0, 0.01, \dots, 0.19$  s, whereas sequence  $\hat{x}[n]$  is sampled at  $T = 0.005, 0.015, \dots, 0.195$  s.

The result of this multiplication is a new spectrum  $\hat{X}[\Omega]$  and a new corresponding sequence  $\hat{x}[n]$ , which are shown in Figure 28. Multiplication of  $X[\Omega]$  by the complex exponential  $e^{-j\Omega T_s/2}$  does not change its amplitude; only the phase is altered, as shown in Figures 28a and 28b, respectively. The inverse discrete Fourier transform of  $\hat{X}[\Omega]$  results in the sequence  $\hat{x}[n]$ , which is shown in Figure 28c along with the original sequence  $x[n]$ . As the image shows, the sequence  $\hat{x}[n]$  is the sequence  $x[n]$  interpolated at the time instants  $t'$ .

Analogously, the frequency spectrum can also be shifted in frequency by multiplication of the corresponding time series. If a frequency signal  $X(\omega)$  has an inverse Fourier transform  $x(t)$ , multiplication of  $x(t)$  by  $e^{-j\omega_0 t}$  shifts the spectrum by  $\omega_0$ , i.e.,  $X(\omega)$  becomes  $X(\omega + \omega_0)$ . In this case, the frequency spectrum is first converted to the time-domain, where the time series is multiplied by  $e^{-j\omega_0 t}$  and this result is then converted back to the frequency domain, where the shifted spectrum is obtained.

### 3.2 STOLT'S MIGRATION BY FREQUENCY SHIFTS

Applying the time/frequency-shifting results in the entire signal being shifted, i.e.,  $x(t)$  becomes  $x(t - t_0)$  or  $X(\omega)$  becomes  $X(\omega + \omega_0)$ . For discrete signals, this results in all samples being shifted by the same amount.

This poses an issue to perform Stolt's migration with frequency shifting, since Stolt's mapping produces non-uniformly spaced frequency points, which would demand the original spectrum to be entirely shifted for each required frequency sample. For each frequency sample required by Stolt's mapping, the entire spectrum would need to be transformed to the time-domain, phase multiplied and then transformed back to the frequency-domain, which would be computationally expensive for all frequency samples.

Li et al. (2014) devised a method to overcome this issue, which shifts each point individually, without the need to transform the entire spectrum. The algorithm developed by the authors arise from the realization that the frequency shift of each point can be achieved in two operations. Suppose that frequency point  $f_i \in f$ , where  $f$  is a vector containing the temporal frequencies of the FFT, is to be shifted to a frequency point  $f(k_{z_i})$ . Since  $f$  is a discrete vector, the shift from  $f_i$  to  $f(k_{z_i})$  can be achieved first by a change in index (inter-bin shift) and subsequently with a phase multiplication (sub-bin shift).

This concept is illustrated in Figure 29, where frequency point  $f_i$  on the vector  $f$  is to be shifted to frequency point  $f(k_{z_i})$ . First, an inter-bin shift is performed, by changing from  $f_i$  to  $f_{i+1}$ . The shift is then completed by the sub-bin shift, which is accomplished with a phase multiplication of the corresponding time series.

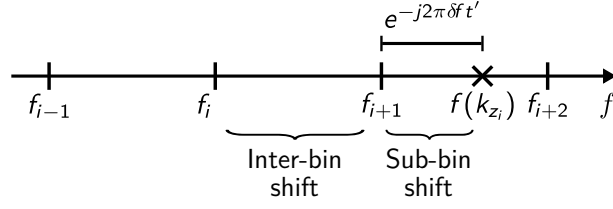


**Figure 29: Frequency shift as a two-step operation.**

Recall in Section 2.2.1, which discussed the  $\omega k$ -SAFT algorithm. The development of the algorithm consisted in solving the wave propagation problem, by relating the wavefield distribution  $\psi(x, z)$  at the time of explosion ( $t = 0$ ) to the spectrum of the raw ultrasonic data  $\Psi_0(k_x, f)$  obtained by the transducer at the surface ( $z = 0$ ). Stolt's migration consists of obtaining the spectrum  $\Psi_0$ , which is discrete and consists of uniformly-spaced frequency points, on non-uniformly distributed frequency points, with a mapping from  $f$  to  $f(k_z)$ , where  $k_z$  is the wavenumber related to the  $z$ -axis of the image. Without loss of generality, Stolt's migration using frequency shifts with the algorithm developed by Li et al. (2014) can be synthesized by the following steps:

1. For the  $i$ -th frequency bin ( $i = 0, 1, \dots, N - 1$ ), where  $N$  is the number of time samples, extract the frequency point

$$\Psi_{k_x}^i = \Psi_0(k_x, f_i). \quad (26)$$

The frequency shift is given by  $f_{\text{shift}} = f_i - f(k_z)$ . If  $\Delta f$  is the size of each frequency bin, the inter-bin shift  $n_i$  is given by  $n_i = \text{floor}(f_{\text{shift}}/\Delta f)$ , while the sub-bin shift  $\delta f$  is given by  $\delta f = f_{\text{shift}} - n_i \Delta f$ .

2. Zero-pad the sample  $\Psi_{k_x}^i$  to the length-4 vector

$$\Psi'_{k_x} = \begin{bmatrix} 0 & 0 & \Psi_{k_x}^i & 0 \end{bmatrix}, \quad (27)$$

and create the length-4 vector of indexes  $l = \begin{bmatrix} i - 2 & i - 1 & i & i + 1 \end{bmatrix} - n_i$  circularly in  $\begin{bmatrix} 0, 1, \dots, N - 1 \end{bmatrix}$ .

3. Apply the inverse Fourier transform to  $\Psi'_{k_x}$  to obtain  $\psi'_{k_x}$ .
4. Shift  $\psi'_{k_x}$  by phase multiplication of  $\psi'_{k_x}$  to obtain

$$\psi''_{k_x} = \psi'_{k_x} e^{-j2\pi\delta f t'}, \quad (28)$$

where  $t'$  are the time instants of the samples  $l$ , i.e.,  $t' = t[l]$ , and  $t$  is a vector containing the time instants of the samples of the echo signals. In this step, the spectrum  $\Psi'_{k_x}$  is shifted by  $\delta f$ .

5. Apply the Fourier transform to  $\psi''_{k_x}$  to obtain  $\psi''_{k_x}$ , which is  $\psi'_{k_x}$  shifted by  $\delta f$ .
6. Coherently sum the shifted samples to the migrated spectrum

$$\hat{\psi}_l = \hat{\psi}_l + \psi''_{k_x}. \quad (29)$$

7. Repeat steps (1) to (6) for all frequency bins to obtain  $\hat{\psi}$ .

Applying this technique, Li et al. (2014) was able to focus radar images. The results obtained by the authors showed that this approach can show computational complexity lower than interpolation methods. They compared interpolation by frequency shifts with sinc-based interpolations, and obtained a gain of over 4 times in execution time, while maintaining image quality. The authors did not compare the proposed method to piecewise linear interpolation.

### 3.3 EXTENSION TO ULTRASONIC IMAGING

The algorithm developed by Li et al. (2014) to shift individual frequency points replaces only the interpolation step required by Stolt's migration. Hence, it is possible to use the algorithm without modifications to focus ultrasonic images, for inspections with a monostatic transducer. One of the limitations of the algorithm is that the image grid must be fixed, i.e., it is not possible to focus on arbitrary  $(x, z)$  points. This is because each frequency point  $f_i$  is shifted to a corresponding frequency point  $f(k_{z_i})$  and, thus, the points on the  $z$ -axis of the focused image are restricted.

An arbitrary definition of the points on the  $z$ -axis of the image would be possible if, instead of shifting each point from  $f$  to  $f(k_z)$ , only the closest points of  $f(k_z)$  on  $f$  were to be shifted. This concept is shown in Figure 30, where, instead of shifting to  $f(k_{z_i})$  from the corresponding point  $f_i$ , the point lying closest to  $f(k_{z_i})$  is shifted. In the example shown in Figure 30, it is suffice to shift point  $f_3$  to point  $f(k_{z_i})$ . In addition to allowing an arbitrary definition of the points on the  $z$ -axis of the focused image, this approach also eliminates the need of inter-bin shifts.

Thus, we propose to complete Stolt's migration by shifting only the nearest available frequency. The extended algorithm can be summarized in the following steps:

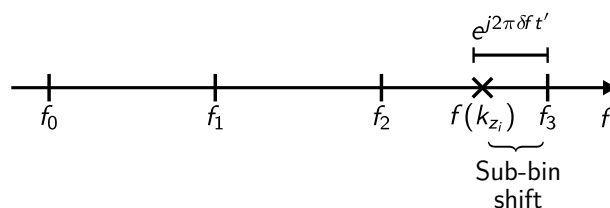


**Figure 30: Shifting closest points.**

1. For the  $i$ -th spatial frequency bin ( $i = 0, 1, \dots, N_z - 1$ ), where  $N_z$  is the number of points in the  $z$ -axis, compute the frequency

$$f(k_{z_i}) = \text{sgn}(k_{z_i}) \hat{c} \sqrt{k_x^2 + k_{z_i}^2}, \quad (30)$$

where  $\text{sgn}$  is the sign function.

2. Search the vector  $f$  for the frequency point  $f_p$  which is closest to  $f(k_{z_i})$ , compute the frequency shift  $\delta f = f_p - f(k_{z_i})$ . Create the length-4 vectors of indexes  $I = [i-2 \ i-1 \ i \ i+1]$  circularly in  $N_z$  and  $P = [p-2 \ p-1 \ p \ p+1]$  circularly in  $N$ .
3. Extract the frequency point

$$\Psi_{k_x}^p = \Psi_0(k_x, f_p). \quad (31)$$

4. Zero-pad the sample  $\Psi_{k_x}^p$  to the vector

$$\Psi'_{k_x} = [0 \ 0 \ \Psi_{k_x}^p \ 0]. \quad (32)$$

5. Apply the inverse Fourier transform to  $\Psi'_{k_x}$  to obtain  $\psi'_{k_x}$ .
6. Shift  $\Psi'_{k_x}$  by phase multiplication of  $\psi'_{k_x}$  to obtain

$$\psi''_{k_x} = \psi'_{k_x} e^{j2\pi\delta f t'}, \quad (33)$$

where  $t'$  are the time instants of the samples  $P$ , i.e.,  $t' = t[P]$ , and  $t$  is a vector containing the time instants of the samples of the echo signals. In this step, the spectrum  $\psi'_{k_x}$  is shifted by  $\delta f$ .

7. Apply the Fourier transform to  $\psi''_{k_x}$  to obtain  $\Psi''_{k_x}$ , which is  $\Psi'_{k_x}$  shifted by  $\delta f$ .
8. Coherently sum the shifted samples to the migrated spectrum

$$\hat{\Psi}_l = \hat{\Psi}_l + \Psi''_{k_x}. \quad (34)$$

9. Repeat steps (1) to (8) for all frequency bins to obtain  $\hat{\Psi}$ .

Step (2) of the algorithm requires, for each spatial frequency bin, searching the vector  $f$  for the closest value to the frequency point  $f(k_{z_i})$ , which could be a computationally expensive operation. However, the vector  $f$  consists of regularly spaced frequency points, which allows  $f_p$  to be efficiently determined by estimating the index of  $f(k_{z_i})$  on  $f$ .

Algorithm 4 shows a pseudocode for the proposed nearest-neighbor shift (NNS) algorithm. The Fourier-transformed inspection data is assumed to be a 2-D matrix of the form  $\Psi(f, k_x)$ , where  $f$  are the temporal frequencies and  $k_x$  is the spatial frequency wavenumber related to the  $x$ -axis. It is assumed that each column of this 2-D matrix corresponds to a specific  $k_x$ , i.e., each column is the Fourier transform of each A-scan signal.

Algorithm 4 performs Stolt's migration for each column of the 2-D matrix  $\Psi(f, k_x)$ . The algorithm take as input several parameters. The first parameter is the vector  $\Psi_0$ , of size  $N$ , which is the frequency spectrum  $\Psi(f, k_x)$  for a specific  $k_x$ . The vector  $f$ , of size  $N$ , contains the spatial frequencies corresponding to the spectrum, while the vector  $t$ , also of size  $N$ , contains the time instants for which the A-scan signals were acquired. The spatial-frequency wavenumbers  $k_x$  and  $k_z$  are also required. In this case,  $k_x$  is a scalar and  $k_z$  is a vector of size  $N_z$  related to the  $z$ -axis of the image. The ERM velocity for ultrasonic inspection with monostatic transducers must also be informed, as a scalar  $\hat{c}$ . The output of the algorithm is the migrated vector  $\hat{\Psi}$ , of size  $N_z$ .

The algorithm starts by defining the variables  $f_{\min}$  and  $\Delta f$  in lines 1 and 2. The variable  $f_{\min}$  corresponds to the lowest frequency value contained in the vector  $f$ , while the variable  $\Delta f$  is the frequency resolution. Next, the algorithm loops for each value of  $i$ , starting from zero and stopping at  $i = N_z - 1$ . In each loop, Stolt's migration frequency  $f_{\text{mig}}$  is computed (line 4), its index on vector  $f$  is estimated (line 5) and the frequency shift  $\delta f$  is computed (line 6). The indexing vectors  $P$  and  $I$  are also computed (lines 7 and 8) and the time instants  $t'$  corresponding to the indexes given by  $P$  are stored in a vector (line 9). The effective migration of the spectrum starts by selection the  $p$ -th sample of the vector  $\Psi_0$  (line 10) and zero-padding it to the vector  $\Psi'$  (line 11). The inverse Fourier transform  $\psi'$  of this vector is then taken (line 12) and phase-multiplied (line 13) to displace the spectrum by  $\delta f$ . After phase-multiplication, the resulting vector  $\psi''$  is transformed back to the frequency domain (line 14) and the resulting samples  $\Psi''$  are coherently summed to the migrated spectrum  $\hat{\Psi}$  (line 15).

Algorithm 4 is specific for the  $\omega k$ -SAFT algorithm only because Stolt's mapping is performed as  $f_{\text{mig}} = \text{sgn}(k_z[i])\hat{c}\sqrt{k_x^2 + k_z[i]^2}$ , which is Stolt's migration for inspections with monostatic transducers. Algorithm 4 can be adapted to the Wavenumber and  $\omega k$ -CPWC algorithms by changing the computation of  $f_{\text{mig}}$  according to (23) and (24). From this, the  $\omega k$ -SAFT, Wavenumber and  $\omega k$ -CPWC algorithms can be implemented with frequency shifts by changing the interpolation step required in Algorithms 1, 2 and 3 to the procedure described by Algorithm 4.

---

**Algorithm 4** Pseudocode for the proposed nearest-neighbor shift (NNS) algorithm.

---

**Require:**  $\Psi_0$  (a vector of size  $N$ ),  $f$  (a vector of size  $N$ ),  $t$  (a vector of size  $N$ ),  $k_x$  (a scalar),  $k_z$  (a vector of size  $N_z$ ),  $\hat{c}$

**Ensure:**  $\hat{\Psi}$  (a vector of size  $N_z$ )

```

1:  $f_{\min} \leftarrow \min(f)$ 
2:  $\Delta f \leftarrow f[1] - f[0]$ 
3: for each  $i = 0, 1, \dots, N_z - 1$  do
4:    $f_{\text{mig}} \leftarrow \text{sgn}(k_z[i])\hat{c}\sqrt{k_x^2 + k_z[i]^2}$ 
5:    $p \leftarrow \text{round}((f_{\text{mig}} - f_{\min})/\Delta f)$ 
6:    $\delta f \leftarrow f[p] - f_{\text{mig}}$ 
7:    $P \leftarrow [p - 2 \ p - 1 \ p \ p + 1] \bmod N$ 
8:    $I \leftarrow [i - 2 \ i - 1 \ i \ i + 1] \bmod N_z$ 
9:    $t' \leftarrow t[P]$ 
10:   $\Psi_p \leftarrow \Psi_0[p]$ 
11:   $\Psi' \leftarrow [0 \ 0 \ \Psi_p \ 0]$ 
12:   $\psi' \leftarrow \text{ifft}(\Psi')$ 
13:   $\psi'' \leftarrow \psi' e^{j2\pi\delta f t'}$ 
14:   $\Psi'' \leftarrow \text{fft}(\psi'')$ 
15:   $\hat{\Psi}[I] \leftarrow \hat{\Psi}[I] + \Psi''$ 
16: end for

```

---

### 3.4 REVIEW

Frequency-domain algorithms employing piecewise linear interpolation require high oversampling factors in order to reconstruct well focused images. This chapter presented the concept of interpolation by frequency shifts, which is an alternative to the usual method of FFT oversampling and piecewise linear interpolation.

The concept of interpolation by frequency shifts is based on the time/frequency shift property of the Fourier transform. In order to complete Stolt's migration, Li et al. (2014) developed an algorithm capable of shifting individual points of the spectrum to new frequency points. This algorithm was developed for synthetic aperture radar and is limited to reconstructing images in a fixed grid. This chapter presented an extension of Li's algorithm to ultrasonic imaging. The developed algorithm is able to focus on arbitrary points on the inspected object and replaces the interpolation step required by the  $\omega k$ -SAFT, Wavenumber and  $\omega k$ -CPWC algorithms.

## 4 MATERIALS AND METHODS

The frequency-domain algorithms were evaluated with experimental ultrasonic data. This chapter details the specimen used for testing and the set-up to acquire the experimental ultrasonic signals. Details concerning the implementation of the frequency-domain algorithms are discussed, along with the pre-processing and post-processing applied to the raw ultrasonic signals and to the reconstructed images. The metrics considered to evaluate the performance of the algorithms are also discussed in this chapter.

### 4.1 EXPERIMENTS

The proposed method was verified with experimental data. For testing, the specimen illustrated in Figure 31 was used. The specimen used consists of an aluminum block, with 80 mm of length, 60 mm of height and 25 mm of depth. The specimen contains four SDHs, each with a diameter of 1 mm. For geometrical reference, the origin of a Cartesian system of coordinates  $(x, z)$  was considered as shown in Figure 31. The  $x$ -axis is considered as a line along the surface of the object, and is also referred to as lateral-axis or spatial-axis. The  $z$ -axis was considered as a line along the height of the object, and is also referred to as depth-axis or axial-axis. The value of  $z$  increases as a point moves in the down direction. The origin  $(x, z) = (0, 0)$  of this system is the intersection of the  $x$  and  $z$  axis, as shown in the figure. The longitudinal wave velocity is  $c = 6370$  m/s.

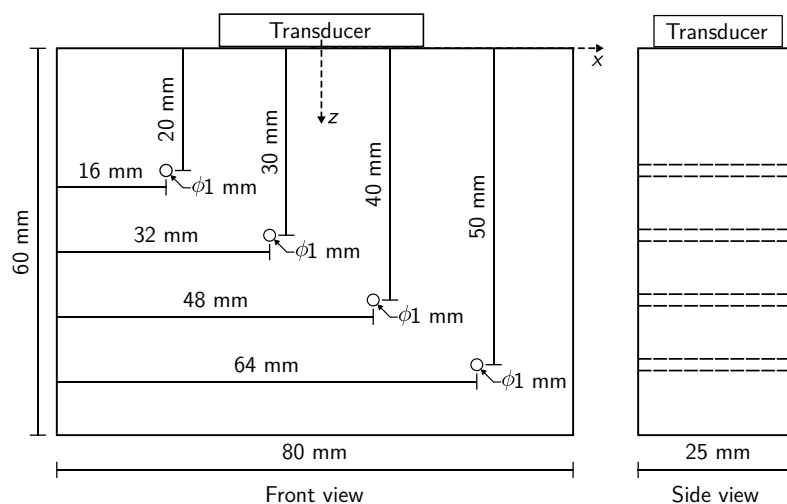


**Figure 31: Specimen used for acquisition of ultrasonic data with a linear array transducer.**

The transducer used to acquire the ultrasonic signal was an Olympus 5L64-A32 probe. This is a linear array transducer, which contains 64 elements with a 5 MHz central frequency and element pitch of 0.5 mm. The array was controlled with an Eddyfi Panther research scanner. The scanner sampled the A-scan signals from the transducer at a sampling frequency of 125 MHz. In addition, the transducer was centered with the specimen.

Three data sets were acquired from the specimen. The first data set was an FMC of the object, for which all the elements of the array were used. The second data set is a sweeping inspection, which is derived from the FMC data set by extracting only the A-scan signals of the main diagonal of the matrix (refer to Section 2.1.4.2 for details on obtaining sweeping data set from an FMC). The third data set was from acquisition with plane-waves (PWI). For the PWI acquisition, a set of 21 angles were used, ranging from  $-10^\circ$  to  $10^\circ$ , with a step of  $1^\circ$ . For the acquisition of the FMC and PWI data sets, no gating was applied, i.e., the time samples start at  $t = 0$  (refer to Section 2.1.1 for the definition of gating). Each A-scan signal was sampled during a period of  $44.144 \mu\text{s}$ , rendering a total of 5519 time samples. Hence, the FMC data set acquired has dimension (5519, 64, 64), the sweeping data set has dimension (5519, 64) and the PWI data set has dimension (5519, 21, 64).

## 4.2 IMPLEMENTATIONS

It is worth recalling that interpolation of the spectrum of the ultrasonic data is required both in the frequency-axis and in the wavenumber-axis, as discussed in Section 3.3. Implementation of the aforementioned frequency-domain algorithms were performed with piecewise linear interpolation of the wavenumber-axis and with either piecewise linear interpolation or frequency shifts in the frequency-axis. To differentiate algorithms performing Stolt's migration on the frequency-axis with piecewise linear interpolation or with the proposed nearest-neighbor shift approach, we denote as  $\omega k$ -SAFT, Wavenumber and  $\omega k$ -CPWC the algorithms using piecewise linear interpolation and we denote as NNS- $\omega k$ -SAFT, NNS-Wavenumber and NNS- $\omega k$ -CPWC the algorithms employing frequency shifts.

Implementation of the  $\omega k$ -SAFT, Wavenumber and  $\omega k$ -CPWC algorithms followed the set of pseudocodes indicated in Algorithms 1, 2 and 3. These algorithms use piecewise linear interpolation to perform Stolt's migration on the frequency-axis. Implementation of the NNS- $\omega k$ -SAFT, NNS-Wavenumber and NNS- $\omega k$ -CPWC used essentially the same pseudocode, except that piecewise linear interpolation was replaced with the appropriate adaptation of Algorithm 4, which performs Stolt's migration with frequency shifts.

### 4.3 PRE-PROCESSING

Before processing, the raw ultrasonic data were pre-processed. Pre-processing consisted in gating and zero-padding the echo data. Gating was applied to acquire the ultrasonic signals relevant to the imaging region only, while zero-padding was applied to increase the spectral density of the echo data both in the time-axis and in the spatial-axis (or element-axis).

The ultrasonic data was acquired in a  $44.144 \mu\text{s}$  time-window, which corresponds to a depth  $d$  of  $d = ct/2 \approx 140.6 \text{ mm}$ . Since the specimen used for testing has a height of 60 mm, the A-scan signals contains echos from reflectors beyond the bottom of the object and echos from multiple reflections inside the object. Thus, before processing, gating was applied to the data sets, in order to retain only the relevant data contained in the imaging region. This gating was applied by considering only the size of the imaging region. For instance, for an imaging region ranging from  $z_s = 10 \text{ mm}$  to  $z_e = 60 \text{ mm}$ , only the time samples from index  $i_s = 2z_s f_s/c \approx 392$  to index  $i_e = 2z_e f_s/c \approx 2355$ , where  $f_s$  is the sampling frequency of the A-scan signals, were considered. No gating was applied to the spatial-axis of the ultrasonic echo data.

In addition, the echo data was padded with zeros in both the time- and spatial-axis to produce an oversampled FFT, as mentioned previously. Zero-padding was applied in the time-axis only for algorithms using piecewise linear interpolation to complete Stolt's migration, whereas the echo data was padded with zeros in the spatial-axis for all algorithms. The amount of zero padding applied to the spatial-axis aimed at rounding the number of samples to the next power of two.

To illustrate gating and zero-padding, consider the FMC data set, initially with dimension (5519, 64, 64). For an imaging region ranging from  $z_s = 10 \text{ mm}$  to  $z_e = 60 \text{ mm}$ , gating of the time samples leads to a resulting data set of dimension (1963, 64, 64). Zero-padding the spatial-axis (or element-axis) such that its length is rounded to the next power of two results in a data set of dimension (1963, 128, 128). Similarly, the PWI data set has, initially, a dimension of (5519, 64, 64). Gating the time samples and zero-padding the spatial-axis leads to a data set of dimension (1963, 21, 128). The same concept is used to zero-pad the time-axis. For instance, zero-padding the time-axis to the next power of two leads to a data set of dimension (2048, 128, 128) for the FMC. In Chapter 5, of results and discussion, the amount of zero-padding on the time-axis is varied, also aiming at rounding the time samples to the next power of two. Thus, increasing further the amount of zero-padding on the time-axis leads to a data set of dimension (4096, 128, 128).

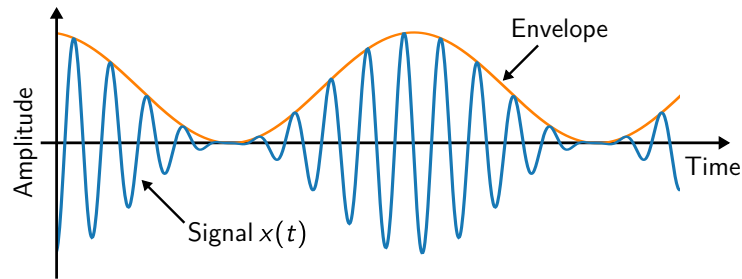


**Figure 32: Amplitude envelope of a signal  $x(t)$ .**

In this study, we refer to the oversampling factor, instead of referring to the number of samples after zero-padding. The oversampling factor is defined as the ratio between the number of samples after zero-padding and the original number of samples, for the time-axis only. Considering original number of samples in the time-axis as 1963, zero-padding the time samples to a length of 4096 produces an oversampling factor of 2.09.

#### 4.4 POST-PROCESSING

After processing the ultrasonic data with the evaluated algorithms, the reconstructed images were post-processed before exhibition. In this study, we employ amplitude envelope extraction and normalization as post-processing steps for the ultrasound images.

To aid visualization, it is common to extract the amplitude envelope of the reconstructed images before display. The amplitude envelope of a signal  $x(t)$  is shown in Figure 32 and corresponds to the magnitude of its analytic signal (FELDMAN, 2011). In reconstructed ultrasonic images, the amplitude envelope is extracted for each column of the image. Normalization consists of applying an offset and a scaling factor to the image such that all values lie inside the  $[0, 1]$  range. This is helpful to compare images, since each algorithm may produce an image with varying ranges.

Figure 33 shows the same ultrasound image before and after post-processing. The image shown is the image obtained with the  $\omega k$ -SAFT algorithm, previously shown in Figure 21. Before post-processing, shown in Figure 33a, the oscillating values on the image hinders its interpretation. The amplitude envelope of the image allows for a better interpretation of the image, as indicated in Figure 33b. In this case, the images have been normalized to the  $[0, 1]$  range and are displayed in a gray-scale color map, where pixel values closer to zero are displayed in white and pixel values closer to 1 are displayed in black.

#### 4.5 METRICS

Two metrics, image quality and number of floating point operations, were used to assess the performance of the frequency-domain algorithms considered in this study.

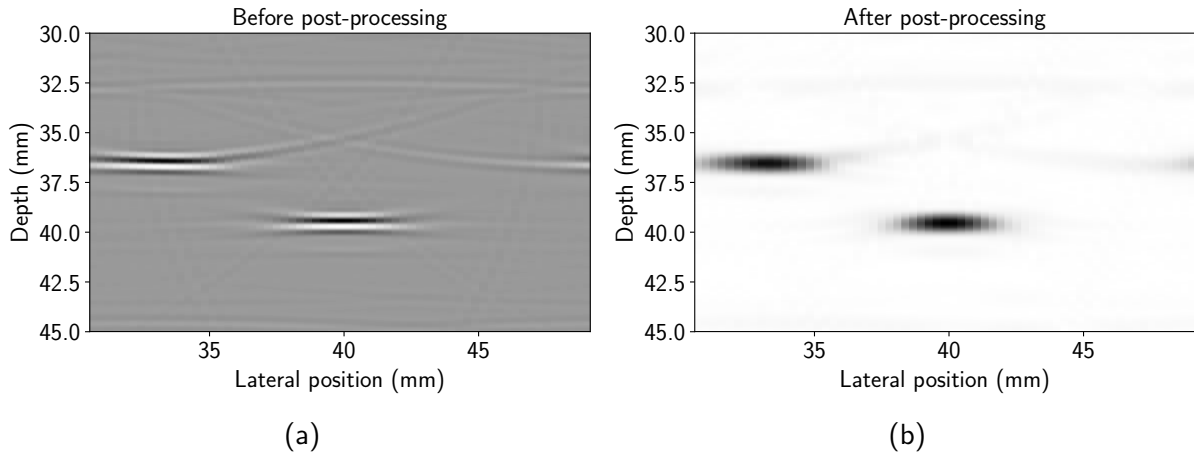


**Figure 33: Ultrasound image (a) before and (b) after post-processing.**

The execution time of an algorithm is related to the required number of floating operations. The number of floating point operations, also referred to as *flops*, accounts for the number of real additions and real multiplications. In this study, the number of floating point operations was estimated analytically and verified experimentally, by measuring the execution time of each algorithm. The algorithms were executed 10 times and the average of these samples was considered as a representative value of its execution time.

Image quality was assessed with the contrast-to-noise ratio (CNR) metric, which is a measure between the standard deviation  $\sigma_s$  of a signal and the standard deviation  $\sigma_n$  of its noise. The CNR, expressed in decibels (dB), is given by (WELVAERT; ROSSEEL, 2013):

$$\text{CNR} = 20 \log \left( \frac{\sigma_s}{\sigma_n} \right). \quad (35)$$

The CNR was evaluated on the reconstructed images after normalization and amplitude envelope extraction. The signal contained in the images was defined as the pixel values inside the flaw and bottom regions, whereas the noise was considered as the surrounding background. Figure 34 shows the mask used to extract the signal and noise from the reconstructed images. The signal is considered as the values inside the black regions, whereas noise is the surrounding white region.

#### 4.6 REVIEW

This chapter presented details concerning the experimental setup used for ultrasonic data acquisition. The experimental data were acquired from an aluminum block containing four SDHS. Two data sets were acquired from the specimen, which provided data for execution of all frequency-domain algorithms evaluated.

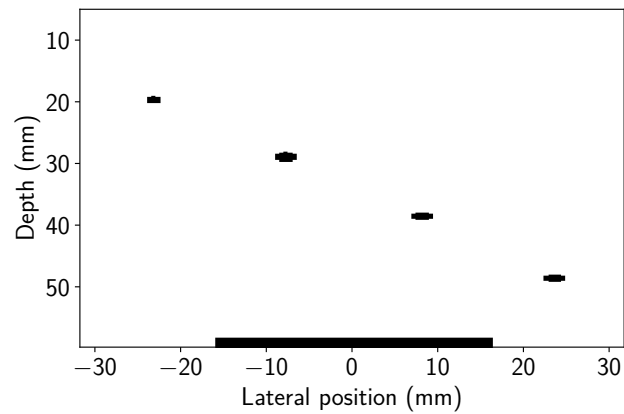


**Figure 34: Mask used to extract signal and noise from an image. The signal is considered as the pixels inside the black regions, while noise is considered as the pixel values in the surrounding white region.**

Details of the implementation of the frequency-domain algorithms were also presented. Before processing with the implemented algorithms, the raw ultrasonic data were pre-processed with gating and zero-padding and the reconstructed images were post-processed with envelope extraction and normalization. Evaluation of the performance of each algorithm was based on the two metrics presented in this chapter. Image quality is assessed with the CNR metric and the number of floating point operations is used to estimate computational load.

## 5 RESULTS AND DISCUSSION

This chapter presents the results obtained by using the proposed algorithm to focus ultrasonic images in the frequency-domain. The proposed algorithm is compared to the frequency-domain algorithms employing the oversampled FFT and piecewise linear interpolation, in terms of image CNR and floating point operations. The results were obtained with data acquired from the experimental setup described in Chapter 4.

The algorithms evaluated allows to focus on arbitrary positions on the  $z$ -axis of the images (also denoted as depth-axis or axial-axis). The  $\omega k$ -SAFT, Wavenumber and  $\omega k$ -CPWC algorithms achieves this with piecewise linear interpolation of the spectral data, whereas the NNS- $\omega k$ -SAFT, NNS-Wavenumber and NNS- $\omega k$ -CPWC algorithms achieves focusing on arbitrary depths via frequency shifting of the spectrum. The spatial resolution of the  $z$ -axis influences both reconstruction quality and the required number of floating point operations. Thus, before evaluating CNR and the number of floating operations of each algorithm, the influence of spatial resolution on image reconstruction is first evaluated.

The oversampling factor affects the frequency-domain algorithms which use piecewise linear interpolation to perform Stolt's migration, and this effect is evaluated next. This evaluation is required, in order to determine a sufficient oversampling factor for the time samples of the echo data. On the one hand, an insufficient oversampling factor may lead to images that are not well focused, and image quality will be low despite a shorter number of floating point operations. On the other hand, a high oversampling factor may lead to well focused images but the number of floating point operations may be large. Hence, the influence of the oversampling factor on the CNR of the images obtained with algorithms employing piecewise linear interpolation is evaluated. In addition, these results are compared to the CNR of the images obtained with algorithms using frequency shifts.

The number of floating point operations required by each algorithm are then evaluated. For the  $\omega k$ -SAFT, Wavenumber and  $\omega k$ -CPWC algorithms, this depends on the oversampling factor and on the number of points in the imaging region. For the NNS- $\omega k$ -SAFT, NNS-Wavenumber and NNS- $\omega k$ -CPWC algorithms, this depends of the number of points in the imaging region only. In addition, the execution time of the algorithms are measured and compared, as a function of the height of the imaging region.

The last section of this chapter verifies how CNR and execution time of the evaluated algorithms varies with the imaging region. These metrics are not only affected by the size of the imaging region; the content of the echo signals directly impacts reconstruction quality.

## 5.1 SPATIAL RESOLUTION

Stolt's migration allows to arbitrarily focus the reconstructed images on the depth-axis (z-axis or axial-axis). This allows the imaging region or the region-of-interest (ROI) to have an arbitrary spatial resolution. A lower spatial resolution leads to images with fewer points and with a "pixelated" aspect. As the spatial resolution of the image increases, the final image contains more points and may have a better visual aspect. For the evaluated frequency domain algorithms, as the spatial resolution increases, the number of points requiring migration (either by frequency shifts or by piecewise linear interpolation) and the number of points of the inverse 2-D Fourier transform also increases, which leads to higher execution times.

Although finer spatial resolution leads to images with a better visual aspect, the information contained in the reconstructed images is limited by the axial resolution of the ultrasonic system. In an ultrasonic measurement system, the axial resolution is defined as the ability of the system to distinguish between two reflectors located in the same direction as the ultrasonic beam. Theoretically, this resolution is  $n\lambda/2$ , where  $n$  is the number of wave cycles and  $\lambda$  is the wavelength of the ultrasonic wave (NG; SWANEVELDER, 2011; SILVERMAN, 2009). In essence, the resolution is limited to half the spatial length of the ultrasonic pulse. Thus, increasing the spatial resolution of the image beyond a certain amount does not provide any additional information, since this is limited by the resolution of the ultrasonic system.

Figures 35–37 shows images reconstructed with the  $\omega k$ -SAFT, Wavenumber and  $\omega k$ -CPWC algorithms with a varying spatial resolution, which is varied by varying the size of each pixel of the image. For each pixel, the width is fixed at 0.5 mm and the height is varied from  $\lambda/2$  to  $\lambda/16$ . The images were reconstructed on a ROI with  $x \in [-31.75, 31.75]$  mm and  $z \in [5, 60]$  mm. For all algorithms, images with a pixel height of  $\lambda/2$  are focused but difficult to interpret. Decreasing the pixel height to  $\lambda/4$  results in clearer images, with the flaws well visible. With a pixel height of  $\lambda/8$ , the reconstructed images contain less artifacts. Decreasing the pixel height to  $\lambda/16$  does not visibly improve image quality.

In this study, a pixel width of 0.5 mm and a pixel height of  $\lambda/8$  is chosen. The width is chosen to be the same as the pitch of the transducer, which allows the image to be reconstructed in the same lateral positions as its elements without interpolation of the spectrum of the data in the spatial-axis, or with interpolation via the oversampled FFT. The height is chosen as  $\lambda/8$  as the images are not improved by selecting a smaller height.

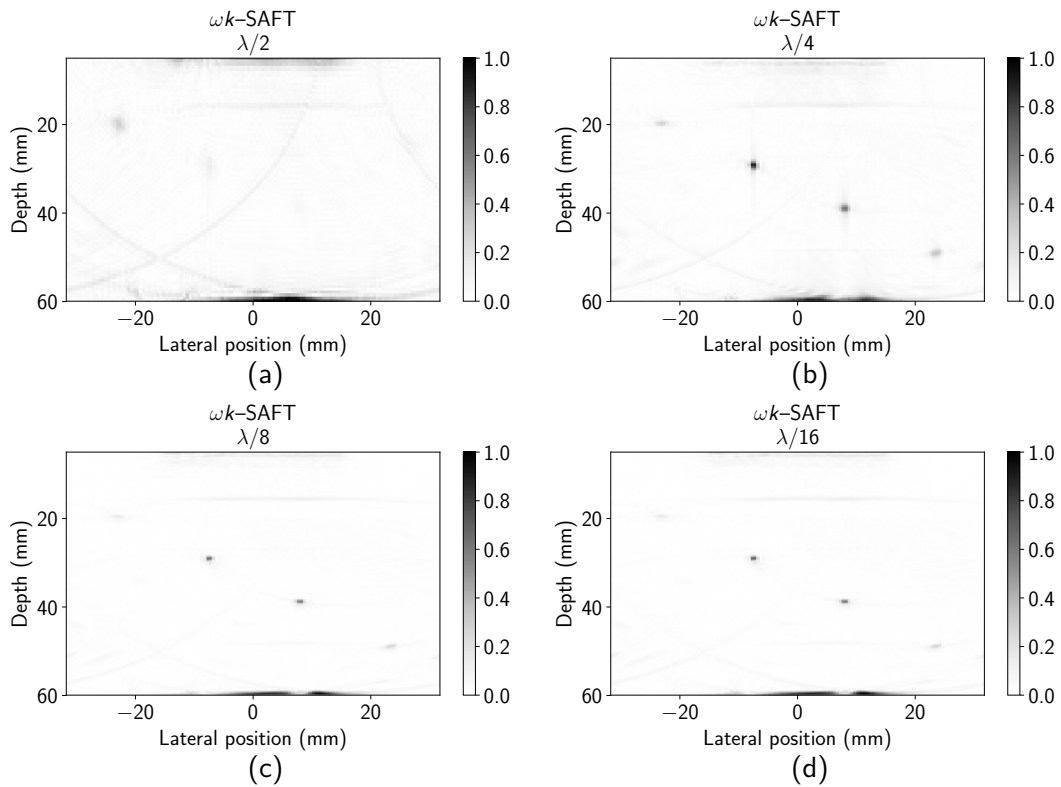


**Figure 35: Effect of spatial resolution on images reconstructed with the  $\omega k$ -SAFT algorithm. Images were reconstructed on a ROI with  $x \in [-31.75, 31.75]$  mm and  $z \in [5, 60]$  mm, with a pixel width of 0.5 mm and pixel height of (a)  $\lambda/2$ , (b)  $\lambda/4$ , (c)  $\lambda/8$  and (d)  $\lambda/16$ .**

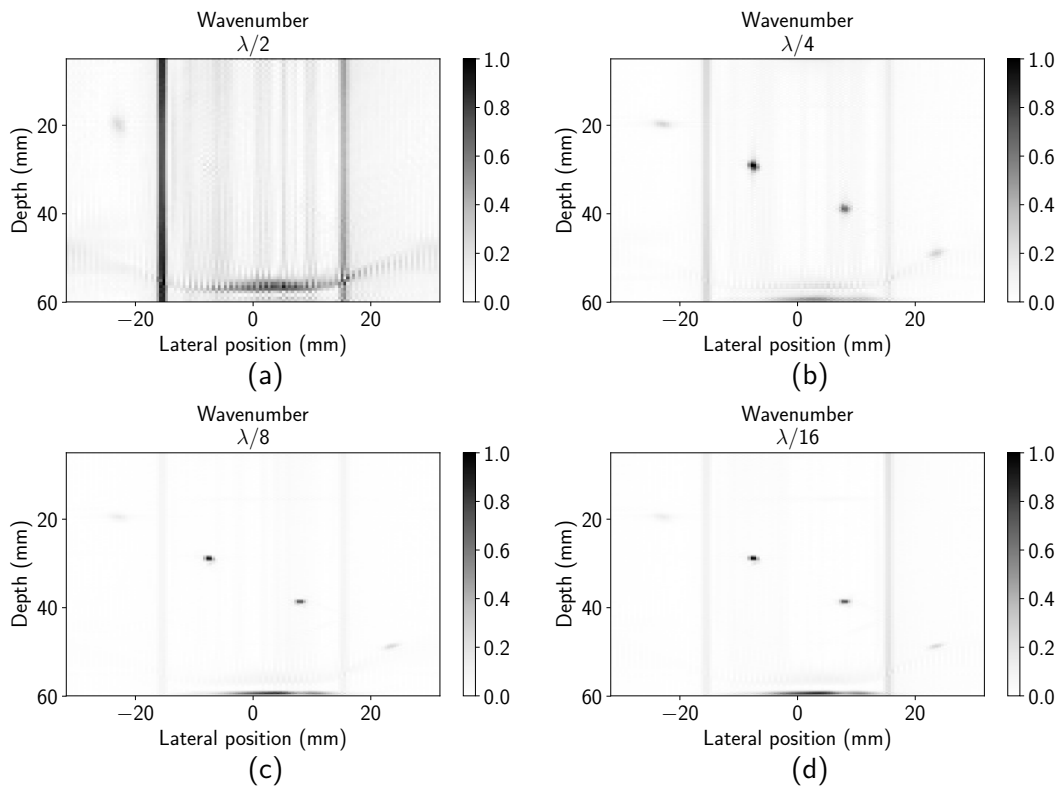


**Figure 36: Effect of spatial resolution on images reconstructed with the Wavenumber algorithm. Images were reconstructed on a ROI with  $x \in [-31.75, 31.75]$  mm and  $z \in [5, 60]$  mm, with a pixel width of 0.5 mm and pixel height of (a)  $\lambda/2$ , (b)  $\lambda/4$ , (c)  $\lambda/8$  and (d)  $\lambda/16$ .**

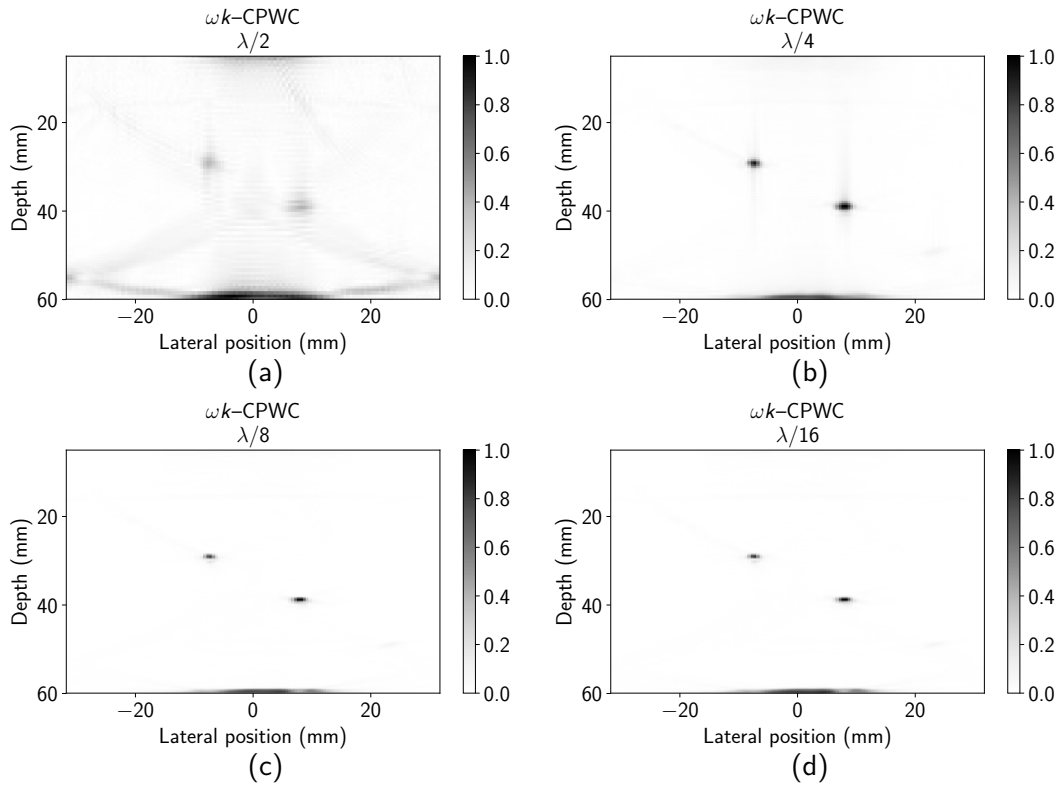
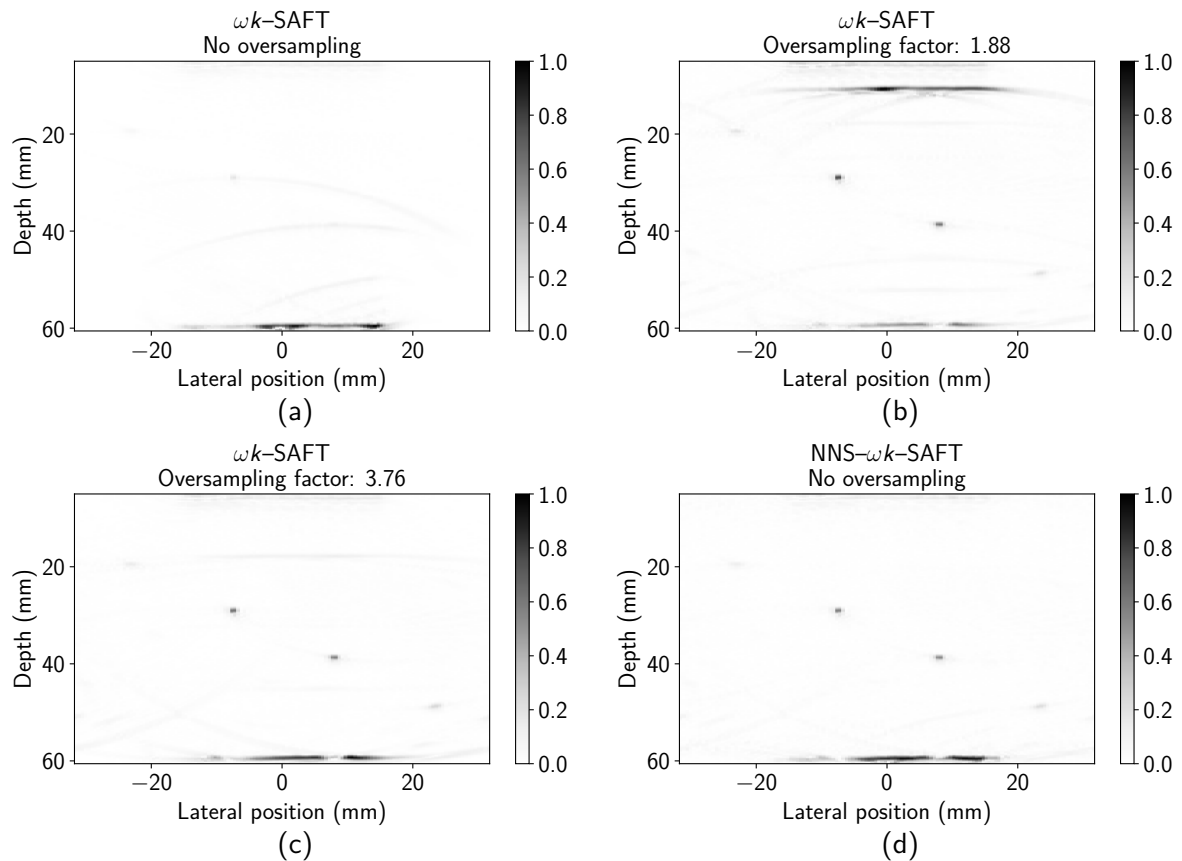


**Figure 37: Effect of spatial resolution on images reconstructed with the  $\omega k$ -CPWC algorithm. Images were reconstructed on a ROI with  $x \in [-31.75, 31.75]$  mm and  $z \in [5, 60]$  mm, with a pixel width of 0.5 mm and pixel height of (a)  $\lambda/2$ , (b)  $\lambda/4$ , (c)  $\lambda/8$  and (d)  $\lambda/16$ .**

## 5.2 EFFECT OF THE OVERSAMPLING FACTOR

The  $\omega k$ -SAFT, Wavenumber and  $\omega k$ -CPWC algorithms use piecewise linear interpolation to perform Stolt's migration. However, piecewise linear interpolation alone may not be sufficient and the reconstructed images may not be correctly focused, due to large interpolation errors. In order to improve the interpolation error, a common approach is to use an oversampled FFT, obtained by zero-padding the time-axis of the acquired ultrasonic data before applying the FFT. This increases the density of the spectrum of the data, via sinc-based interpolation of the frequency samples. Hence, the oversampling factor applied to the ultrasonic data affects the quality of the reconstructed images when migration is performed with piecewise linear interpolation.

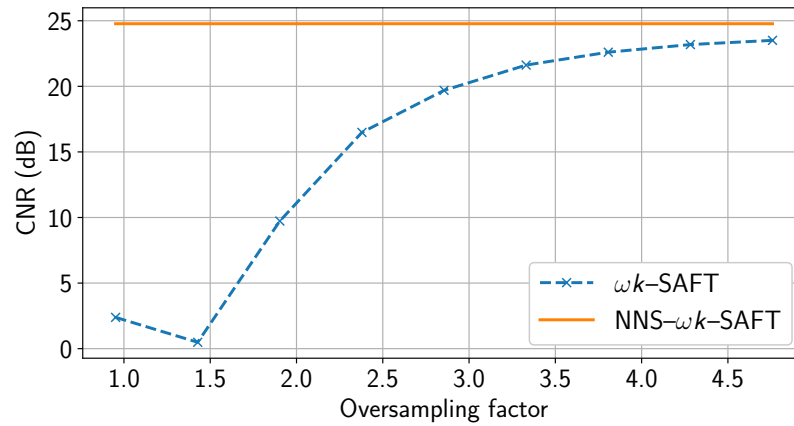
Figure 38 shows images reconstructed with the  $\omega k$ -SAFT algorithm, with no oversampling and with an oversampling factor of 1.88 and 3.76. With no oversampling, as shown in Figure 38a, the reconstructed image is not well focused and the flaws are not clearly visible. Using an oversampling factor of 1.88 improves the reconstructed image, as shown in Figure 38b. The flaws are visible but there are strong artifacts on the upper region of the image. Increasing the oversampling factor to 3.76 further improves the reconstructed image,



**Figure 38: Effect of the oversampling factor on images reconstructed with the  $\omega k$ -SAFT algorithm. Images were reconstructed on a ROI with  $x \in [-31.75, 31.75]$  mm and  $z \in [5, 60]$  mm, with (a) no oversampling (b) an oversampling factor of 1.88 and (c) an oversampling factor of 3.76. (d) The image reconstructed with the NNS- $\omega k$ -SAFT is also shown, which does not require oversampling of the FFT.**

as there are less artifacts and the two flaws directly below the transducer are clearly visible, as indicated in Figure 38c. In addition, Figure 38d shows the image reconstructed with the NNS- $\omega k$ -SAFT algorithm, which uses frequency shifts instead of piecewise linear interpolation. As Figure 38d shows, the image reconstructed with NNS- $\omega k$ -SAFT requires no oversampling and the reconstructed image is similar to the image obtained with the  $\omega k$ -SAFT algorithm with an oversampling factor of 3.76.

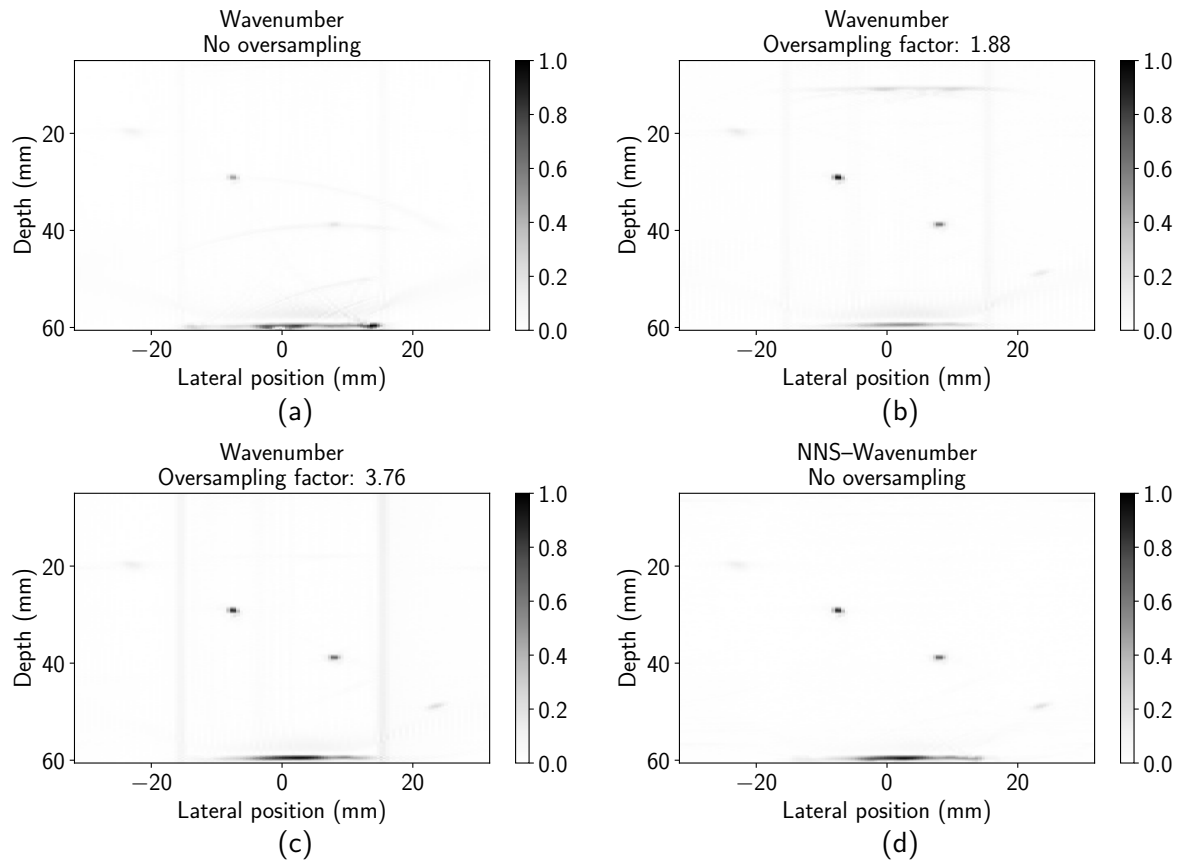
The CNR of images reconstructed with the  $\omega k$ -SAFT algorithm for a varying oversampling factor is shown in Figure 39. As the image shows, the CNR increases with the oversampling factor, in accordance with the results shown in Figure 38. Figure 39 also shows the CNR of the image reconstructed with the NNS- $\omega k$ -SAFT algorithm, which is constant as function of oversampling, since this is not required for this algorithm. Figure 39 shows that the CNR of the image reconstructed with the NNS- $\omega k$ -SAFT algorithm is always higher than the CNR of the image reconstructed with the  $\omega k$ -SAFT algorithm, even after the latter uses an oversampled FFT with a factor of 4.75, in which case the margin is approximately 0.5 dB.



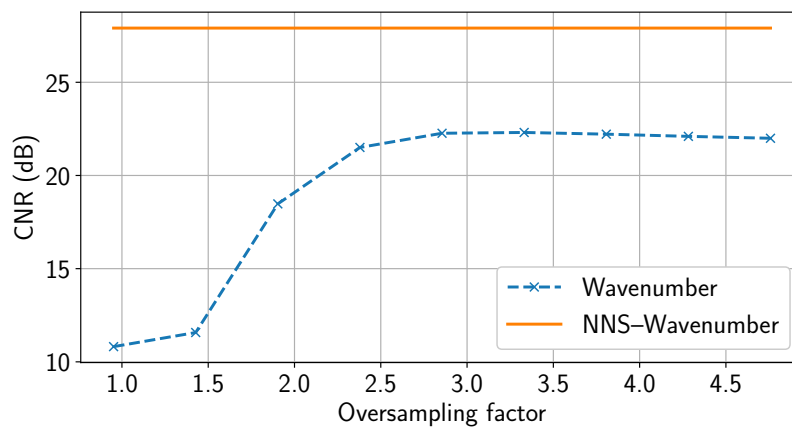
**Figure 39: CNR of the images obtained with the  $\omega k$ -SAFT algorithm, for a varying oversampling factor (dashed line) and CNR of the image obtained with the NNS- $\omega k$ -SAFT algorithm (solid line), which does not depend on oversampling.**

Figure 40 shows the effect of oversampling on the images reconstructed by the Wavenumber algorithm. With no oversampling, shown in Figure 40a, the image is not correctly focused, as the signal from the flaws appear weak and on the same level of intensity as the surrounding artifacts. After using an oversampling factor of 1.88, the image is improved, such that the signals from the two flaws directly below the transducer are clearly visible, as shown in Figure 40b. However, artifacts still appear in the upper region on the image. The reconstructed image is further improved by increasing the oversampling factor to 3.76, as shown in Figure 40c. The artifacts in the upper region appears weak and the signal from the bottom of the object appears with a higher intensity. In addition, the image reconstructed with the NNS-Wavenumber is shown in Figure 40d, which requires no oversampling and the image obtained is comparable to the image obtained with the Wavenumber algorithm using an oversampling factor of 3.76.

The CNR of the images reconstructed with the Wavenumber algorithm, as a function of the oversampling factor, is shown in Figure 41. The CNR improves until an oversampling factor of 2.8 is reached, and remains approximately constant as the oversampling factor is increased further. Figure 41 also shows the CNR of the image reconstructed with the NNS-Wavenumber algorithm, which is constant since no oversampling is required in this case. As Figure 41 shows, the CNR of the image obtained with the NNS-Wavenumber algorithm is at least 5 dB higher than the CNR of the images obtained with the Wavenumber algorithm, regardless of the oversampling factor. This is mainly due to the artifacts seen around the border of the transducer, as shown in Figure 40, which appears on the images reconstructed with the Wavenumber algorithm but do not appear on the image reconstructed with the NNS-Wavenumber algorithm.



**Figure 40: Effect of oversampling on images reconstructed with the Wavenumber algorithm. Images were reconstructed on a ROI with  $x \in [-31.75, 31.75]$  mm and  $z \in [5, 60]$  mm, with (a) no oversampling (b) an oversampling factor of 1.88 and (c) an oversampling factor of 3.76. (d) The image reconstructed with the NNS-Wavenumber is also shown, which does not require oversampling of the FFT.**



**Figure 41: CNR of the images obtained with the Wavenumber algorithm, for a varying oversampling factor (dashed line) and CNR of the image obtained with the NNS-Wavenumber algorithm (solid line), which does not depend on oversampling.**

The effect of zero-padding on the time-axis for the  $\omega k$ -CPWC algorithm is shown in Figure 42. Similarly to the results obtained with the  $\omega k$ -SAFT and Wavenumber algorithms, no oversampling of the FFT does not result in a well focused image, as shown in Figure 42a. Although the two flaws below the transducer appears on the image, they are surrounded by artifacts. After using an oversampling factor of 1.88, the reconstructed image contains less artifacts, as shown in Figure 42b. There are no visible artifacts surrounding the flaws, but there are artifacts in the upper region of the image. Using an oversampling factor of 3.76 further decreases the artifacts in the reconstructed image, as shown in Figure 42c. The artifacts in the upper region of the image are not clearly visible and the echo from the bottom of the object has a higher intensity. In addition, the image reconstructed with the NNS- $\omega k$ -CPWC algorithm is shown in Figure 42d. Oversampling of the FFT is not required for the NNS- $\omega k$ -CPWC algorithm and the image obtained is comparable to the image obtained with the  $\omega k$ -CPWC algorithm using an oversampling factor of 3.76.

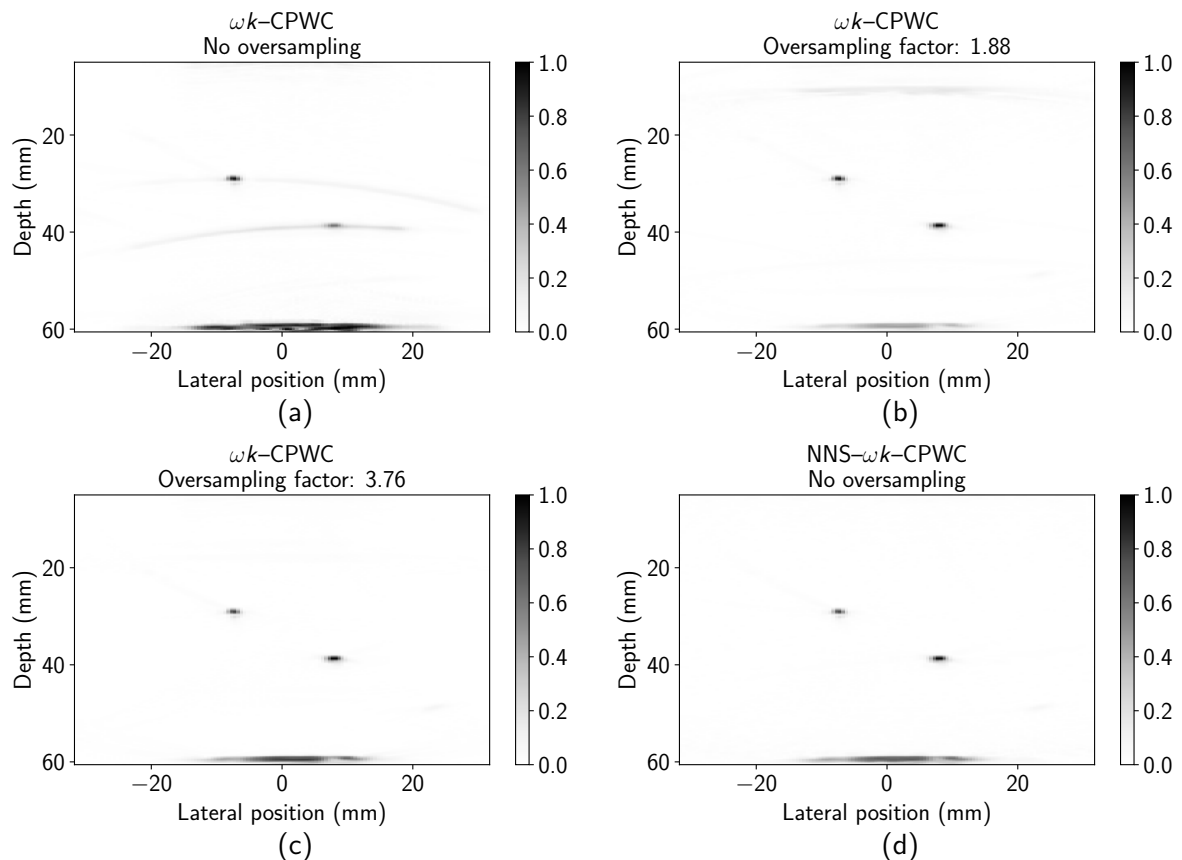


**Figure 42: Effect of oversampling on images reconstructed with the  $\omega k$ -CPWC algorithm. Images were reconstructed on a ROI with  $x \in [-31.75, 31.75]$  mm and  $z \in [5, 60]$  mm, with (a) no oversampling (b) an oversampling factor of 1.88 and (c) an oversampling factor of 3.76. (d) The image reconstructed with the NNS- $\omega k$ -CPWC is also shown, which does not require oversampling of the FFT.**

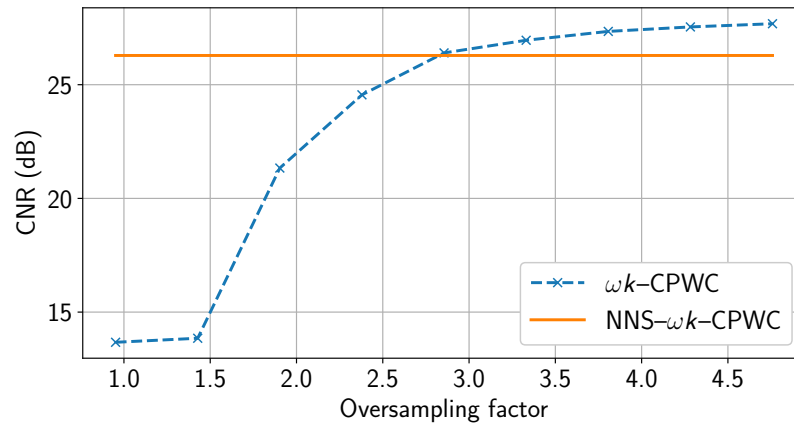


**Figure 43: CNR of the images obtained with the  $\omega k$ -CPWC algorithm, for a varying oversampling factor (dashed line) and CNR of the image obtained with the NNS- $\omega k$ -CPWC algorithm (solid line), which does not depend on oversampling.**

The CNR of the images reconstructed by the  $\omega k$ -CPWC algorithm, as a function of the oversampling factor, is shown in Figure 43. The CNR of the reconstructed images increase as the oversampling factor increases, as also seen in the results shown in Figure 42. Figure 43 also shows the CNR of the image reconstructed with the NNS- $\omega k$ -CPWC algorithm, which is constant, since no oversampling is required. As the image shows, the CNR of the image reconstructed by both algorithms is close when the oversampling factor is 2.8. Increasing the oversampling factor for the  $\omega k$ -CPWC algorithm beyond this point produces images with higher CNR than the CNR obtained with the image reconstructed by the NNS- $\omega k$ -CPWC algorithm. For an oversampling factor of 3.76, the CNR of the  $\omega k$ -CPWC algorithm improves by approximately 1 dB, and it is improved further by approximately 0.5 dB for an oversampling factor of 4.75.

### 5.3 NUMBER OF FLOATING POINT OPERATIONS

The execution time of an algorithm is impacted by the required number of floating point operations. The number of floating operations usually accounts for the number of real additions and real multiplications of an algorithm, and the higher the number of real additions and real multiplications of an algorithm, the longer its execution time. The number of floating point operations of each algorithm was evaluated.

The  $\omega k$ -SAFT algorithm consists essentially of three steps. Initially, a 2-D FFT is applied to the ultrasonic data, after it has been padded with zeros, both in the time-axis and in the spatial-axis. If the padded ultrasonic data has dimension  $(K', J)$ , where  $K'$  is the number of time samples and  $J$  is the number of spatial positions of the padded echo data, a 2-D FFT on this data set has  $5K'J \log_2(K'J)$  floating point operations (JOHNSON; FRIGO, 2007; LI et al., 2014). After the initial 2-D FFT, the resulting spectrum is then linearly interpolated.

The complex-valued spectrum needs to be interpolated on the real-valued frequency points dictated by Stolt's migration. Piecewise linear interpolation of a real point  $x_q$ , which lies between the known pair  $(x_0, y_0)$  and  $(x_1, y_1)$ , where  $x_0$  and  $x_1$  are real-valued variables and  $y_0$  and  $y_1$  are complex-valued variables, is given by:

$$y_q = y_0 + (y_1 - y_0) \left( \frac{x_q - x_0}{x_1 - x_0} \right), \quad (36)$$

where  $y_q$  is the (complex-valued) interpolated sample. Piecewise linear interpolation as presented in (36) contains two complex additions, two real additions, two real multiplications and one real division. Considering that a complex addition has two real additions, piecewise linear interpolation is estimated to have 9 floating point operations. In this study, we do not weight addition, division and multiplication and consider these operations to account for a single floating point operation. The  $\omega k$ -SAFT algorithm requires linear interpolation of all points in the imaging region. Hence, if the image is reconstructed on the same  $J$  spatial positions of the padded echo data and  $N$  is the number of points in the depth-axis of the image, the  $\omega k$ -SAFT algorithm requires  $9NJ$  floating point operations. The last step of the  $\omega k$ -SAFT algorithm is a 2-D inverse FFT of the interpolated spectrum, which requires  $5NJ \log_2(NJ)$  operations. Thus, the total number of operations required by the  $\omega k$ -SAFT algorithm is estimated to be:

$$\Gamma_{\omega k\text{-SAFT}} = 5K'J \log_2(K'J) + 9NJ + 5NJ \log_2(NJ). \quad (37)$$

The NNS- $\omega k$ -SAFT differs from the  $\omega k$ -SAFT in two aspects. First, the initial 2-D FFT is applied to the echo data without zero-padding of the time-axis. Thus, if the echo data, without padding of the time-axis, has dimension  $(K, J)$ , the initial 2-D FFT has  $5KJ \log_2(KJ)$  floating point operations. Second, instead of piecewise linear interpolation, the nearest-neighbor shift approach proposed in Algorithm 4 is used. The frequency-shifting algorithm is estimated to have  $\alpha NJ$  floating point operations, where  $\alpha$  is a positive constant and reflects the number of floating operations required by the frequency shifting algorithm (LI et al., 2014). Hence, the estimated number of floating operations required by the NNS- $\omega k$ -SAFT algorithm is estimated at:

$$\Gamma_{\text{NNS-}\omega k\text{-SAFT}} = 5KJ \log_2(KJ) + \alpha NJ + 5NJ \log_2(NJ). \quad (38)$$

The  $\omega k$ -SAFT and NNS- $\omega k$ -SAFT differs in the first two steps and thus, the difference in the execution time between these algorithms results from the size of the initial 2-D FFT and the method to complete Stolt's migration. The initial 2-D FFT requires more operations for the  $\omega k$ -SAFT algorithm than the NNS- $\omega k$ -SAFT algorithm, since the latter does not require zero-padding of the time axis, i.e.,  $K < K'$ . However, the NNS- $\omega k$ -SAFT algorithm requires more operations than the  $\omega k$ -SAFT algorithm to complete Stolt's migra-

tion. Since the frequency-shifting algorithm requires at least a 4-point direct and inverse FFT, the NNS- $\omega k$ -SAFT algorithm requires at least  $40 \log_2(4)$  floating point operations, which is more than the  $9NJ$  operations required by piecewise linear interpolation.

For a small number of points in the imaging region (small  $N$ ), the number of floating point operations required by the NNS- $\omega k$ -SAFT algorithm is lower than the number of floating point operations required by the  $\omega k$ -SAFT algorithm. Hence, for smaller imaging regions, the execution time of the NNS- $\omega k$ -SAFT algorithm is expected to be lower than the execution time of the  $\omega k$ -SAFT algorithm. As the imaging region increases and  $N$  gets larger, the execution time of the  $\omega k$ -SAFT algorithm is expected to be shorter than the execution time of the NNS- $\omega k$ -SAFT algorithm, since the nearest-neighbor frequency shift algorithm requires more floating point operations to migrate each point of the imaging region.

Figure 44 shows the execution time of the  $\omega k$ -SAFT and NNS- $\omega k$ -SAFT algorithms, as a function of the height of the imaging region. The images were reconstructed on a ROI with  $x \in [-31.75, 31.75]$  mm and the height varying from 5 mm to 60 mm. For the  $\omega k$ -SAFT algorithm, the amount of zero-padding was fixed at 10240 samples in order to keep the spectral density of the FFT constant. This is the amount of zero-padding corresponding to the 4.75 oversampling factor shown previously in Figure 39, which produces, for the  $\omega k$ -SAFT algorithm, a CNR value closer to the image reconstructed with the NNS- $\omega k$ -SAFT algorithm.

As Figure 44 shows, the execution time of the NNS- $\omega k$ -SAFT algorithm is much lower than that of the  $\omega k$ -SAFT, for small ROI heights. For a height of 30 mm, the NNS- $\omega k$ -SAFT algorithm executes in less than half the execution time of the  $\omega k$ -SAFT algorithm. As the imaging region height increases, the execution time of the NNS- $\omega k$ -SAFT algorithm grows faster than the execution time of the  $\omega k$ -SAFT algorithm, since the frequency-shifting method requires more floating point operations to complete Stolt's migration.

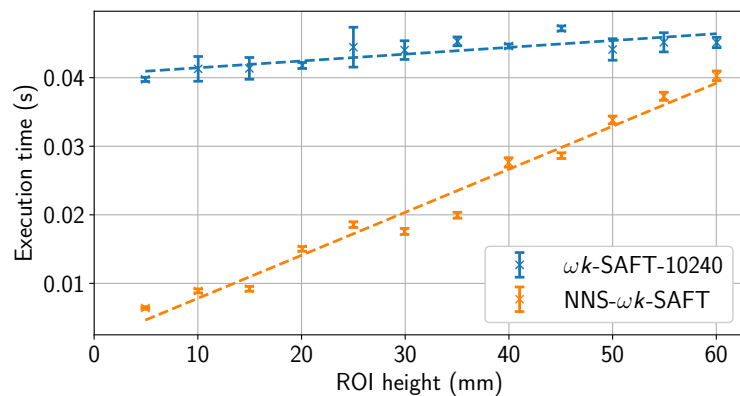


**Figure 44: Execution time of the  $\omega k$ -SAFT and NNS- $\omega k$ -SAFT algorithms, as a function of ROI height. The images were reconstructed in a ROI with  $x \in [-31.75, 31.75]$  mm and depth varying from 5 mm to 60 mm.**

The analysis of the number of floating point operations required by the  $\omega k$ -SAFT and NNS- $\omega k$ -SAFT algorithms can be extended to the Wavenumber and NNS-Wavenumber algorithms, since they consist of essentially the same three steps. The Wavenumber contains a 3-D FFT on the echo data, padded both in the time- and spatial-axis, which requires  $5K'J^2 \log_2(K'J^2)$  floating point operations. Next, for each emitting element, the spectrum is linearly interpolated, which consists of  $9NJ^2$  floating point operations. The last step is a 2-D inverse FFT on the interpolated and summed spectrum, which requires  $5NJ \log_2(NJ)$  floating point operations. Thus, an estimate of the floating point operations required for the Wavenumber algorithms is:

$$\Gamma_{\text{Wavenumber}} = 5K'J^2 \log_2(K'J^2) + 9NJ^2 + 5NJ \log_2(NJ). \quad (39)$$

The NNS-Wavenumber algorithm contains the same steps; however, the initial 3-D FFT is applied to the echo data padded only in the spatial-axis, which requires  $5KJ^2 \log_2(KJ^2)$  floating point operations. Additionally, linear interpolation is replaced with the nearest-neighbor shift algorithm, which requires  $\alpha NJ^2$  floating point operations. Therefore, the number of floating point operations required by the NNS-Wavenumber algorithm is estimated to be:

$$\Gamma_{\text{NNS-Wavenumber}} = 5KJ^2 \log_2(KJ^2) + \alpha NJ^2 + 5NJ \log_2(NJ). \quad (40)$$

Analogous to the  $\omega k$ -SAFT and NNS- $\omega k$ -SAFT algorithms, the NNS-Wavenumber algorithm is expected to have shorter execution times for a smaller number of points in the imaging region, since the cost of the initial 3-D FFT dominates the overall number of floating point operations and is higher for the Wavenumber algorithm. However, the Wavenumber algorithm is expected to have shorter execution times on imaging regions with a larger number of points, since the number of floating point operations required by the nearest-neighbor shift algorithm is higher than linear interpolation.

The execution time for the Wavenumber and NNS-Wavenumber algorithms, as a function of the ROI height, is shown in Figure 45. The images were reconstructed on a ROI with  $x \in [-31.75, 31.75]$  mm and the height varying from 5 mm to 60 mm. The Wavenumber algorithm was executed with zero-padding the time-axis of the echo data to a length of 6144 (corresponding to the oversampling factor of 2.8 in Figure 41), since the CNR does not improve by padding the time-axis to a length beyond this point. As Figure 45 shows, for ROI heights smaller than 45 mm, the execution time of the NNS-Wavenumber algorithm is lower than the execution time of the Wavenumber algorithm. However, the execution time of the NNS-Wavenumber algorithm is higher than the execution time of the Wavenumber algorithm as the ROI height increases beyond 45 mm.

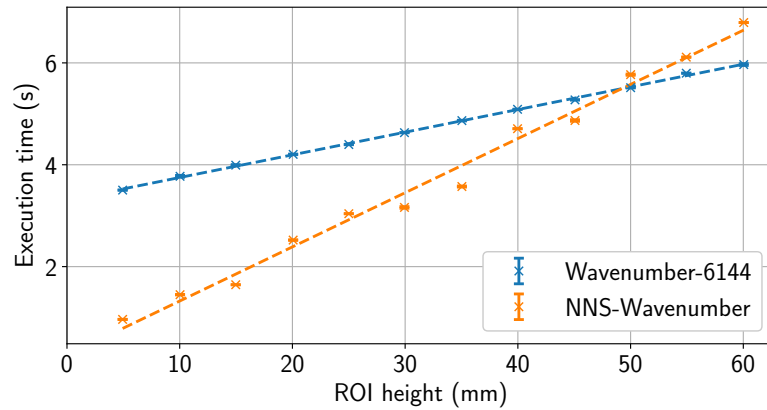


**Figure 45: Execution time of the Wavenumber and NNS–Wavenumber algorithms, as a function of ROI height. The images were reconstructed in a ROI with  $x \in [-31.75, 31.75]$  mm and depth varying from 5 mm to 60 mm.**

Estimation of the number of floating point operations required by the  $\omega k$ –CPWC and NNS– $\omega k$ –CPWC algorithms is analogous to the analysis applied previously. The  $\omega k$ –CPWC reconstruct one image from each emitting angle, which requires requires a 2-D FFT on the padded echo data, linear interpolation of the spectrum and accumulation on a single reconstructed spectrum. This procedure is repeated for the  $M$  emitted angles and then an inverse 2-D FFT is applied to the accumulated spectrum. The number of floating point operations for the  $\omega k$ –CPWC algorithms is estimated to be:

$$\Gamma_{\omega k\text{-CPWC}} = 5MK'J \log_2(K'J) + 9MNJ + 5NJ \log_2(NJ). \quad (41)$$

Replacing linear interpolation with frequency-shifts changes the size of the 2-D FFT and replaces linear interpolation with the frequency-shifting algorithm. An estimate for the number of floating point operations of the NNS– $\omega k$ –CPWC algorithm is:

$$\Gamma_{\text{NNS-}\omega k\text{-CPWC}} = 5MKJ \log_2(KJ) + \alpha MNJ + 5NJ \log_2(NJ). \quad (42)$$

For smaller imaging regions, where  $N$  has smaller values, the number of floating point operations required by the NNS– $\omega k$ –CPWC algorithm is lower than the number of floating point operations required by the  $\omega k$ –CPWC algorithm. As the imaging region increases in height and the value of  $N$  reaches larger values, the number of operations required by the NNS– $\omega k$ –CPWC algorithm will be higher than the number of operations required by the  $\omega k$ –CPWC algorithm. Figure 46 shows execution time of the  $\omega k$ –CPWC and NNS– $\omega k$ –CPWC algorithms, as a function of the ROI height. The images were reconstructed on a ROI with  $x \in [-31.75, 31.75]$  mm and the height varying from 5 mm to 60 mm. As Figure 46 shows, the execution time of the NNS– $\omega k$ –CPWC algorithm is lower than the execution time of the  $\omega k$ –CPWC algorithm for smaller ROI heights but grows faster as the height increases.

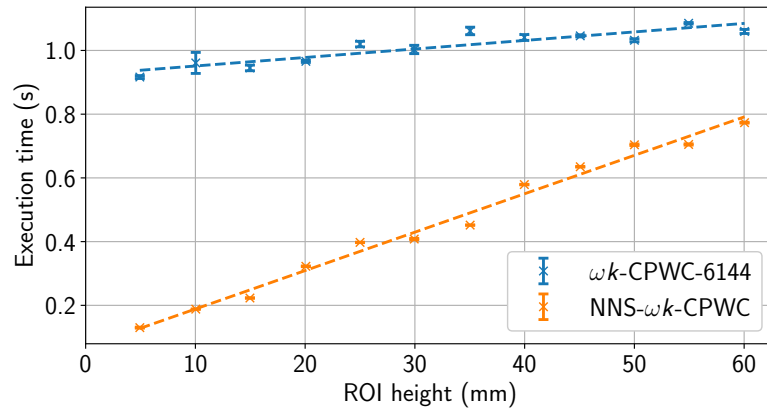


**Figure 46:** Execution time of the  $\omega k$ -CPWC and NNS- $\omega k$ -CPWC algorithms, as a function of ROI height. The images were reconstructed in a ROI with  $x \in [-31.75, 31.75]$  mm and depth varying from 5 mm to 60 mm.

**Table 2:** Data set, dimensions and estimated number of floating point operations for each of the evaluated algorithms.  $K$  is the number of time samples,  $J$  is the number of lateral positions and  $K'$  is the number of time samples after zero-padding. The image is assumed to have dimension  $(N, J)$ , where  $N$  is the number of points in the depth-axis of the image.

Algorithm	Data set	Dimension	Estimated number of floating point operations
$\omega k$ -SAFT	Sweep	$(K', J)$	$5K'J \log_2(K'J) + 9NJ + 5NJ \log_2(NJ)$
NNS- $\omega k$ -SAFT	Sweep	$(K, J)$	$5KJ \log_2(KJ) + \alpha NJ + 5NJ \log_2(NJ)$
Wavenumber	FMC	$(K', J, J)$	$5K'J^2 \log_2(K'J^2) + 9NJ^2 + 5NJ \log_2(NJ)$
NNS-Wavenumber	FMC	$(K, J, J)$	$5KJ^2 \log_2(KJ^2) + \alpha NJ^2 + 5NJ \log_2(NJ)$
$\omega k$ -CPWC	PWI	$(K', M, J)$	$5MK'J \log_2(K'J) + 9MNJ + 5NJ \log_2(NJ)$
NNS- $\omega k$ -CPWC	PWI	$(K, M, J)$	$5MKJ \log_2(KJ) + \alpha MNJ + 5NJ \log_2(NJ)$

Table 2 shows the main aspects of each of the evaluated algorithms. The table shows which data set each algorithm processes, the size of the data set and the estimated number of floating point operations. The dimension of each data set depends either on the number  $K$  of time samples or the number  $K'$  of samples after zero-padding, as well as on the number  $J$  of lateral positions. All algorithms are considered to reconstruct a image of size  $(N, J)$ , where  $N$  is the number of points on the imaging region.

In this study, computational complexity is evaluated in terms of floating point operations and asymptotic behavior (“Big O notation”) is not considered. This is because asymptotic behavior estimates the number of operations as one variable grows to infinity. Since computational complexity is evaluated as a function of the number  $N$  of points in the imaging region, all algorithms show asymptotic complexity of  $\mathcal{O}(N \log_2(N))$ . However, the nearest-neighbor shift approach is advantageous over smaller values of  $N$  and the asymptotic analysis does not capture this behavior.

In addition to influencing the number of floating point operations, the dimension of the data sets affects the memory usage of each algorithm. All algorithms require that the spectrum of the ultrasonic data is stored and algorithms using the oversampled FFT require

more memory since the spectrum contains more points. Since the oversampling factor is multiplicative factor, i.e.,  $K' = \gamma K$ , where  $\gamma$  is a positive constant, algorithms using the oversampled FFT require  $\gamma$  more bytes of memory to store the spectrum of the echo data. However, the overall memory usage of each algorithms depends on several factors. The echo data, its spectrum, the image and its spectrum need not be stored simultaneously and, hence, the memory required by each algorithm depends largely on implementation. Thus, in this study, the overall memory usage is not systematically analyzed.

#### 5.4 RECONSTRUCTION QUALITY AND ROI HEIGHT

Reconstruction quality was evaluated using the CNR metric, on images reconstructed on a ROI which accounts for all the flaws of the object and the backwall (bottom). This indicated which oversampling factor would be required by algorithms using piecewise linear interpolation to best match the CNR of the algorithms using frequency shifts. This oversampling factor leads to an amount of zero-padding, and this amount was used to keep the density of the oversampled FFT constant and to compare execution time of the algorithms using piecewise linear interpolation with a constant spectral density to the algorithms using piecewise linear interpolation.

However, the CNR will vary for different imaging regions and as a consequence, the oversampling factor required by algorithms using piecewise linear interpolation may vary as well. Table 3 shows the CNR and execution time obtained with the  $\omega k$ -SAFT and NNS- $\omega k$ -SAFT algorithms, as the ROI height varies. The images were reconstructed on a ROI with  $x \in [-31.75, 31.75]$  mm and variable depth. The initial value of the depth was kept constant at 10 mm, and the final value ( $z_f$ ) varies from 25 mm to 55 mm. For each ROI, Table 3 shows the amount of time samples after gating ( $K$ ), the oversampling factor ( $\gamma$ ), the CNR and execution time for the  $\omega k$ -SAFT and NNS- $\omega k$ -SAFT algorithms. For the  $\omega k$ -SAFT algorithm, the oversampling factor was chosen such that the CNR matched the one obtained with the NNS- $\omega k$ -SAFT algorithm.

**Table 3: CNR and execution time of the  $\omega k$ -SAFT and NNS- $\omega k$ -SAFT algorithms, for a varying ROI height. The starting value of the ROI is kept constant and the final value is varied. Execution time and standard deviation are in milliseconds.**

$z_f$ (mm)	$K$	$\gamma$	CNR (dB)		Execution time (standard deviation)	
			$\omega k$ -SAFT	NNS- $\omega k$ -SAFT	$\omega k$ -SAFT	NNS- $\omega k$ -SAFT
25	587	4.14	14.5	14.4	13.9 (1.40)	<b>12.9 (0.63)</b>
35	975	2.83	24.4	24.5	19.8 (0.77)	<b>15.4 (0.35)</b>
45	1369	2.62	26.1	26.1	<b>19.7 (0.44)</b>	22.7 (1.32)
55	1762	2.32	26.5	26.5	<b>24.2 (0.59)</b>	32.7 (0.75)

For  $z_f = 25$  mm (a ROI height of 15 mm), only the leftmost flaw of the object appears on the reconstructed image (refer to Figure 31 for the position of each flaw). In this case, the NNS- $\omega k$ -SAFT produced an image with CNR of 14.4 dB, and execution time of 12.9 ms. The  $\omega k$ -SAFT algorithm produces a similar CNR for this ROI if the oversampling factor is 4.14, which leads to an execution time of 13.9 ms. For this ROI, the NNS- $\omega k$ -SAFT produces an image with similar reconstruction quality but with a lower execution time. This is also true when  $z_f = 35$  mm (resulting in a ROI height of 25 mm), in which the two leftmost flaws appear on the reconstructed image. When  $z_f = 45$  mm, three flaws appear on the reconstructed image and, for the same CNR, the  $\omega k$ -SAFT presents a lower execution time. This result is also seen when  $z_f = 55$  mm. In these cases, the  $\omega k$ -SAFT reconstructs an image with similar quality but in a shorter time. The main result indicated in Table 3 is that when the oversampling factor is higher than 2.7, the NNS- $\omega k$ -SAFT algorithm is advantageous over the  $\omega k$ -SAFT algorithm, since for close values of CNR, the execution time will be lower for the algorithm using frequency shifts. When this ratio is lower than 2.7, the  $\omega k$ -SAFT algorithm will show lower execution time, for the same CNR, being advantageous over the NNS- $\omega k$ -SAFT algorithm.

Table 3 seems to contradict the results presented in Section 5.2, where the CNR of the image obtained with the NNS- $\omega k$ -SAFT algorithm was shown to be higher than that of the  $\omega k$ -SAFT algorithm, even if the latter uses an oversampling factor of 4.75. This is because the bottom of the object does not appear in any of the ROIs considered in Table 3. Table 4 shows a different experiment, in which  $z_f$  was kept constant at 60 mm and  $z_i$ , the initial depth of the ROI, varies from 15 mm to 45 mm. In this case, where the bottom of the inspected object appears on the image, the  $\omega k$ -SAFT algorithm requires higher oversampling factors to produce images with CNR similar to those obtained with the NNS- $\omega k$ -SAFT algorithm. This leads to much lower processing times for the NNS- $\omega k$ -SAFT algorithm, at an equal or better reconstruction quality. Thus, the NNS- $\omega k$ -SAFT algorithm is better at reconstructing images which contain the bottom of the object or a flaw with large lateral dimension.

**Table 4: CNR and execution time of the  $\omega k$ -SAFT and NNS- $\omega k$ -SAFT algorithms, for a varying ROI height. The final value of the ROI is kept constant and the starting value is varied. Execution time and standard deviation are in milliseconds.**

$z_i$ (mm)	$K$	$\gamma$	CNR (dB)		Execution time (standard deviation)	
			$\omega k$ -SAFT	NNS- $\omega k$ -SAFT	$\omega k$ -SAFT	NNS- $\omega k$ -SAFT
15	1763	5.81	25.4	26.6	65.3 (9.10)	<b>30.7 (3.39)</b>
25	1368	8.98	24.7	25.0	65.0 (8.31)	<b>22.2 (7.06)</b>
35	975	10.5	23.2	24.3	58.5 (10.4)	<b>16.1 (2.42)</b>
45	587	14.0	20.5	20.6	38.6 (0.75)	<b>13.0 (0.54)</b>

**Table 5: CNR and execution time of the Wavenumber and NNS–Wavenumber algorithms, for a varying ROI height. The starting value of the ROI is kept constant and the final value is varied. Execution time is in seconds and standard deviation is in milliseconds.**

$z_f$ (mm)	$K$	$\gamma$	CNR (dB)		Execution time (standard deviation)	
			Wavenumber	NNS–Wavenumber	Wavenumber	NNS–Wavenumber
25	587	4.36	14.4	14.5	2.45 (19.0)	<b>2.07 (3.05)</b>
35	975	2.63	29.4	29.4	2.93 (28.5)	<b>2.63 (20.8)</b>
45	1369	2.24	29.0	29.1	<b>3.67 (24.7)</b>	3.85 (13.6)
55	1762	2.03	29.1	29.2	<b>4.28 (28.5)</b>	5.87 (39.9)

These results are also seen for the Wavenumber and NNS–Wavenumber algorithms, as shown in Table 5. For a ROI starting with a depth of 10 mm and having a final value varying between 25 mm and 55 mm, the NNS–Wavenumber is advantageous over the Wavenumber algorithm when the oversampling factor is greater than approximately 2.4, in the sense that an image with same CNR can be obtained in a shorter execution time. When the oversampling factor is lower than 2.4, the Wavenumber algorithm is advantageous over the NNS–Wavenumber algorithm, producing images with same CNR on a shorter execution time. However, the bottom of the object does not appear in any of the ROIs evaluated in the results shown in Table 5.

Table 6 shows the CNR and execution time of the Wavenumber and NNS–Wavenumber algorithms for a ROI with final depth fixed at 60 mm and the initial value varying from 15 mm to 45 mm. For ROIs with a starting depth of 15 mm and 25 mm, the Wavenumber algorithm is not able to reach the same CNR as the NNS–Wavenumber algorithm, and its execution time is always higher. For ROIs with starting depths of 45 mm and 55 mm, the Wavenumber algorithm produces values of CNR close to those of the NNS–Wavenumber algorithm only for higher oversampling factors, and the gap in execution time between these two algorithms is wider.

**Table 6: CNR and execution time of the Wavenumber and NNS–Wavenumber algorithms, for a varying ROI height. The final value of the ROI is kept constant and the starting value is varied. Execution time is in seconds and standard deviation is in milliseconds.**

$z_i$ (mm)	$K$	$\gamma$	CNR (dB)		Execution time (standard deviation)	
			Wavenumber	NNS–Wavenumber	Wavenumber	NNS–Wavenumber
15	1763	2.90	22.9	27.4	5.23 (46.2)	<b>5.03 (49.4)</b>
25	1368	4.49	23.3	27.0	5.53 (78.4)	<b>3.58 (12.8)</b>
35	975	10.5	26.2	28.1	7.70 (63.3)	<b>2.67 (5.93)</b>
45	587	12.2	25.4	26.0	5.17 (39.3)	<b>2.08 (5.39)</b>

**Table 7: CNR and execution time of the  $\omega k$ -CPWC and NNS- $\omega k$ -CPWC algorithms, for a varying ROI height. The starting value of the ROI is kept constant and the final value is varied. Execution time is in seconds and standard deviation is in milliseconds.**

$z_f$ (mm)	$K$	$\gamma$	CNR (dB)		Execution time (standard deviation)	
			$\omega k$ -CPWC	NNS- $\omega k$ -CPWC	$\omega k$ -CPWC	NNS- $\omega k$ -CPWC
25	587	5.45	7.4	7.4	0.53 (13.2)	<b>0.27 (5.93)</b>
35	975	2.63	28.4	28.5	0.46 (8.27)	<b>0.37 (3.23)</b>
45	1369	2.20	27.3	27.3	0.59 (8.81)	<b>0.49 (5.94)</b>
55	1762	2.08	28.5	28.5	<b>0.68 (12.7)</b>	0.69 (4.33)

**Table 8: CNR and execution time of the  $\omega k$ -CPWC and NNS- $\omega k$ -CPWC algorithms, for a varying ROI height. The final value of the ROI is kept constant and the starting value is varied. Execution time is in seconds and standard deviation is in milliseconds.**

$z_i$ (mm)	$K$	$\gamma$	CNR (dB)		Execution time (standard deviation)	
			$\omega k$ -CPWC	NNS- $\omega k$ -CPWC	$\omega k$ -CPWC	NNS- $\omega k$ -CPWC
15	1763	3.34	24.1	24.2	1.02 (5.72)	<b>0.65 (3.07)</b>
25	1368	4.30	22.6	22.5	0.99 (7.92)	<b>0.47 (1.17)</b>
35	975	5.91	21.1	21.0	0.92 (6.14)	<b>0.36 (1.47)</b>
45	587	9.38	20.8	20.8	0.94 (19.1)	<b>0.26 (1.02)</b>

These results are also true for the  $\omega k$ -CPWC and NNS- $\omega k$ -CPWC algorithms, as shown in Tables 7 and 8. Considering the case where the bottom of the object does not appear on the reconstructed image, the NNS- $\omega k$ -CPWC algorithm produces images with the same reconstruction quality but at a lower execution time when the oversampling factor is greater than 2. When this factor is smaller than 2, the  $\omega k$ -CPWC shows lower execution time at the same CNR. When the bottom appears on the imaging region, as shown in Table 8, the NNS- $\omega k$ -CPWC produces images with higher CNR at a lower execution time, for all of the evaluated imaging regions.

The results presented in Tables 4–8 show that algorithms using frequency shifts outperforms algorithms using piecewise linear interpolation in terms of CNR and execution time when the imaged region contains the bottom of the object. When the imaged region contains only flaws such as SDHs, algorithms using piecewise linear interpolation may be the better option in terms of execution time, depending on the oversampling factor. The reason for this is discussed in Chapter B of the Appendix. Reconstruction of images containing only SDHs are less sensitive to interpolation error than reconstruction of images containing the bottom of the object. Thus, the oversampling factor for images containing SDH-like flaws can be lowered without degrading reconstruction quality, while reconstruction quality is more affected by the oversampling factor when a flaw with large lateral dimension or the bottom of the object appears on the ultrasonic data.

## 5.5 REVIEW

This chapter compared image reconstruction with the  $\omega k$ -SAFT, Wavenumber and  $\omega k$ -CPWC algorithms to image reconstruction with the NNS- $\omega k$ -SAFT, NNS-Wavenumber and NNS- $\omega k$ -CPWC. The former set of algorithms use an oversampled FFT and piecewise linear interpolation to complete Stolt's migration, whereas the latter set of algorithms use frequency shifts on the frequency spectrum. The comparison evaluated reconstruction quality and the number of floating operations of each algorithm.

The oversampling factor affects reconstruction quality of the  $\omega k$ -SAFT, Wavenumber and  $\omega k$ -CPWC algorithms. Usually, the CNR of the reconstructed images increases as the amount of zero-padding also increases. Except for the Wavenumber algorithm, the CNR of the images reconstructed with the  $\omega k$ -SAFT and  $\omega k$ -CPWC algorithms can be made closer or higher than the CNR of the images reconstructed with the NNS- $\omega k$ -SAFT and NNS- $\omega k$ -CPWC algorithms, depending on the oversampling factor applied to the FFT.

The frequency-domain algorithms were also compared in terms of required number of floating point operations, which affects execution time. Since algorithms using frequency-shifts do not require an oversampled FFT, these algorithms have a lower count of floating point operations than algorithms using piecewise linear interpolation, when the height of the imaging region is smaller. However, algorithms using piecewise linear interpolation show lower number of floating point operations when the imaging region is sufficiently large. Thus, algorithms using frequency shifts have shorter execution time for smaller imaging regions, whereas algorithms using piecewise linear interpolation have shorter execution time if the imaging region is sufficiently large.

Algorithms using frequency shifts outperforms algorithms using piecewise linear interpolation when the imaged region contains the bottom of the object, or a flaw with large lateral dimension. In this case, algorithms using frequency shifts show equal or better CNR than algorithms using piecewise linear interpolation and high oversampling factors, at a lower execution time. When the imaging region contains only SDHs, algorithms using frequency shifts and piecewise linear interpolation can present similar CNR; however, execution time will shorter for each method depending on the oversampling factor.

## 6 CONCLUSIONS

Ultrasonic NDT is an active research area and is widely adopted in the industry and in the medical field. In this research, we have provided an alternative implementation for three common frequency-domain algorithms for ultrasonic image reconstruction, namely the  $\omega k$ -SAFT, Wavenumber and  $\omega k$ -CPWC algorithms. A class of frequency-domain algorithms are based on Stolt's migration, which requires interpolation on the frequency spectrum of the ultrasonic data. Typically, Stolt's migration is completed by using an oversampled FFT and piecewise linear interpolation of the resulting oversampled spectrum. In this case, reconstruction quality depends on the oversampling factor.

An alternative to complete Stolt's migration is with the use of frequency shifts. Instead of interpolating the frequency spectrum to obtain the samples required by Stolt's migration, this approach consists of shifting the frequency spectrum via the time/frequency shifting property of the Fourier transform. The use of frequency shifts was previously applied to the focusing of radar images, where an efficient algorithm was proposed to shift individual samples of the frequency spectrum.

In this research, we showed that frequency shifts can be used to replace the interpolation step required by three common frequency-domain algorithms for ultrasonic imaging based on Stolt's migration, namely the  $\omega k$ -SAFT, Wavenumber and  $\omega k$ -CPWC algorithms. We propose the nearest-neighbor shift approach, from which we propose the NNS- $\omega k$ -SAFT, NNS-Wavenumber and NNS- $\omega k$ -CPWC algorithms. The proposed nearest-neighbor shift is based on the algorithm developed by Li et al. (2014), which performs an inter-bin shift and a sub-bin shift, and does not allow the image to be focused on arbitrary depths. The nearest-neighbor shift algorithm proposed in this study contains only a sub-bin step and allows to focus the image on arbitrary depths. The proposed method is compared to the conventional method by means of image quality, using the CNR metric, and by means of computational complexity, by estimation of the number of floating point operations required by each algorithm.

Reconstruction quality of images obtained by algorithms using either piecewise linear interpolation or frequency shifts was evaluated with the CNR metric. On the imaging region considered, the CNR of the image obtained with the NNS- $\omega k$ -SAFT algorithm is approxima-

tely 0.5 dB higher than the CNR of the image obtained with the  $\omega k$ -SAFT algorithm, when the latter uses an oversampling factor of 4.75. The CNR of the image reconstructed with the NNS-Wavenumber algorithms is at least 5 dB higher than the CNR of the image reconstructed with the Wavenumber algorithm, regardless of the oversampling factor used. For the  $\omega k$ -CPWC algorithm, the CNR of the reconstructed image, in the considered imaging region, is close to the CNR of the image reconstructed with the NNS- $\omega k$ -CPWC algorithm after an oversampling factor of 2.8. Increasing the oversampling factor improves the CNR further, such that the CNR of the  $\omega k$ -CPWC algorithm is higher than the CNR of the NNS- $\omega k$ -CPWC algorithm. The CNR obtained with the  $\omega k$ -CPWC algorithm can be up to 1.5 dB higher than the CNR obtained with NNS- $\omega k$ -CPWC, at an increase in the oversampling factor to 4.75.

The computational load of each algorithm was also evaluated, in terms of number of floating point operations and execution time. Estimation of the number of floating point operations shows that, for a lower number of points in the imaging region, algorithms using frequency shifts presents a lower computational load. This leads to shorter execution times. For an imaging region with 30 mm in height, the execution time of the Wavenumber algorithm was approximately 1.5 times higher than the execution time of the NNS-Wavenumber algorithm. Similarly, the execution time of the  $\omega k$ -SAFT and  $\omega k$ -CPWC algorithms were at least two times higher than the execution time of the NNS- $\omega k$ -SAFT and NNS- $\omega k$ -CPWC algorithms. However, since the nearest-neighbor shift algorithm is more complex than piecewise linear interpolation, the execution time of algorithms using this approach grew faster as the ROI height increased, when compared to algorithms using piecewise linear interpolation.

Reconstruction quality and execution time depends also on the content of the ROI. When the ROI contains the bottom of the object, algorithms using frequency shifts outperforms algorithms using piecewise linear interpolation in terms reconstruction quality and execution time. When the ROI contains only SDH-like flaws, algorithms using piecewise linear interpolation and frequency shifts may present the same reconstruction quality but execution time will be shorter for each algorithm depending on the oversampling factor.

Since the use of an oversampled FFT is not required for the nearest-neighbor shift approach, it is not necessary to choose this parameter for the NNS- $\omega k$ -SAFT, NNS-Wavenumber and NNS- $\omega k$ -CPWC algorithms. When using piecewise linear interpolation, the oversampling factor must be chosen appropriately. If the oversampling factor is high, the image will be well focused at the expense of longer processing time. If the oversampling factor is low, processing time will be shorter but the image will considerably lose CNR. Thus, this parameter must be carefully chosen for the  $\omega k$ -SAFT, Wavenumber and  $\omega k$ -CPWC algorithms.

Future works based on this research may evaluate several aspects not considered here. To apply the direct and inverse FFTs required by all algorithms, the NumPy package was used, which uses the PocketFFT, a modified version of the FFTPack. However, there may be more efficient alternatives, such as the FFTW package. Another aspect not considered in this research is parallelism. The frequency-shifting algorithm can be executed in a parallel fashion, since shifting one sample does not impact shifting another different sample (the same is true for linear interpolation). In addition, parallel computation of the FFT has been reported. The evaluated frequency-domain algorithms could take advantage of parallelism in order to have shorter execution times. Another aspect that may be considered is taking advantage of symmetry of the Fourier transform for real signals, which could be used to avoid interpolation on the negative frequency side of the spectra. Since nearest neighbor shifting is computationally more complex than linear interpolation, avoiding shifting of the negative side of the frequency spectra may be much more beneficial for algorithms using frequency shifts, which may considerably lower execution time.

One result not explored in this study is the memory consumption of the algorithms. Since algorithms with frequency shifts did not require zero-padding, memory requirement of these algorithms may be lower than algorithms using linear interpolation, which may be an important aspect if these algorithms are considered for execution with graphical processing units.

## REFERENCES

- ALBULAYLI, M.; RAKHMATOV, D. Phase-shift depth migration for plane-wave ultrasound imaging. In: **2018 40th Annual International Conference of the IEEE Engineering in Medicine and Biology Society (EMBC)**. [S.l.: s.n.], 2018. p. 911–916. ISSN 1558-4615.
- ALOBAIDI, W. M. et al. Applications of ultrasonic techniques in oil and gas pipeline industries: A review. **American Journal of Operations Research**, v. 5, n. 4, p. 274–287, 2015.
- ANDREUCCI, R. **Ensaio por ultrassom**. [S.l.]: Associação Brasileira de Ensaios Não Destrutivos e Inspeção – Abendi, 2011.
- AUSTENG, A. et al. Coherent plane-wave compounding and minimum variance beamforming. In: **2011 IEEE International Ultrasonics Symposium**. [S.l.: s.n.], 2011. p. 2448–2451. ISSN 1948-5727.
- BAI, J.; FENG, X.-C. Fractional-order anisotropic diffusion for image denoising. **IEEE Transactions on Image Processing**, v. 16, n. 10, p. 2492–2502, 10 2007. ISSN 1941-0042.
- BANNOUF, S. et al. Data set reduction for ultrasonic TFM imaging using the effective aperture approach and virtual sources. **Journal of Physics: Conference Series**, IOP Publishing, v. 457, 8 2013.
- BAUCK, J. L. **A Note on Fourier Transform Conventions Used in Wave Analyses**. 2019. 10.31224/osf.io/jyt96.
- BERCOFF, J. et al. In vivo breast tumor detection using transient elastography. **Ultrasound in Medicine & Biology**, v. 29, n. 10, p. 1387 – 1396, 2003. ISSN 0301-5629. Disponível em: <<http://www.sciencedirect.com/science/article/pii/S0301562903009785>>.
- BERCOFF, J.; TANTER, M.; FINK, M. Supersonic shear imaging: a new technique for soft tissue elasticity mapping. **IEEE Transactions on Ultrasonics, Ferroelectrics, and Frequency Control**, v. 51, n. 4, p. 396–409, April 2004. ISSN 0885-3010.
- BERNARD, O. et al. Ultrasound Fourier slice imaging: a novel approach for ultrafast imaging technique. In: **2014 IEEE International Ultrasonics Symposium**. [S.l.: s.n.], 2014. p. 129–132. ISSN 1051-0117.
- BESSON, A. et al. Compressed delay-and-sum beamforming for ultrafast ultrasound imaging. In: **2016 IEEE International Conference on Image Processing (ICIP)**. [S.l.: s.n.], 2016. p. 2509–2513. ISSN 2381-8549.
- BESSON, A. et al. A sparse reconstruction framework for Fourier-based plane-wave imaging. **IEEE Transactions on Ultrasonics, Ferroelectrics, and Frequency Control**, v. 63, n. 12, p. 2092–2106, Dec 2016. ISSN 0885-3010.
- BLITZ, J.; SIMPSON, G. **Ultrasonic Methods of Non-destructive Testing**. 1st. ed. [S.l.]: Springer Netherlands, 1995.

- CALMON, P. Trends and stakes of NDT simulation. **Journal of Nondestructive Evaluation**, v. 31, n. 4, p. 339–341, 12 2012. ISSN 1573-4862.
- CALMON, P. et al. CIVA: An expertise platform for simulation and processing NDT data. **Ultrasonics**, v. 44, p. e975 – e979, 2006. ISSN 0041-624X.
- CANDES, E. J.; WAKIN, M. B. An introduction to compressive sampling. **IEEE Signal Processing Magazine**, v. 25, n. 2, p. 21–30, March 2008. ISSN 1053-5888.
- CHANG, Y.-F.; CHERN, C.-C. Frequency-wavenumber migration of ultrasonic data. **Journal of Nondestructive Evaluation**, v. 19, n. 1, p. 1–10, 3 2000. ISSN 1573-4862. Disponível em: <<https://doi.org/10.1023/A:1006671706818>>.
- CHEEKE, J. D. N. **Fundamentals and Applications of Ultrasonic Waves**. 2nd. ed. [S.l.]: CRC Press, 2012.
- CHONG, Y. **Fourier Series and Fourier Transforms**. 2016. [http://www1.spms.ntu.edu.sg/~ydhong/teaching/09\\_fourier\\_transform.pdf](http://www1.spms.ntu.edu.sg/~ydhong/teaching/09_fourier_transform.pdf). Accessed: 12/05/2020.
- CLAERBOUT, J. F. **Imaging the Earth's Interior**. Oxford, UK, UK: Blackwell Scientific Publications, Ltd., 1985. ISBN 0-86542-304-0.
- COBBOLD, R. S. C. **Foundations of Biomedical Ultrasound**. 1st. ed. [S.l.]: Oxford University Press, 2006. ISBN 978-0195168310.
- COLLINGWOOD, J. C. Nuclear NDT development at Harwell. **NDT International**, v. 20, n. 1, p. 33 – 41, 1987. ISSN 0308-9126.
- CRUZA, J. F.; CAMACHO, J.; FRITSCH, C. Plane-wave phase-coherence imaging for NDE. **NDT & E International**, v. 87, p. 31 – 37, 2017. ISSN 0963-8695. Disponível em: <<http://www.sciencedirect.com/science/article/pii/S0963869517300087>>.
- DAVID, G. et al. Time domain compressive beamforming of ultrasound signals. **The Journal of the Acoustical Society of America**, v. 137, n. 5, p. 2773–2784, 2015. Disponível em: <<https://doi.org/10.1121/1.4919302>>.
- DRINKWATER, B. W.; WILCOX, P. D. Ultrasonic arrays for non-destructive evaluation: A review. **NDT & E International**, v. 39, n. 7, p. 525 – 541, 2006. ISSN 0963-8695. Disponível em: <<http://www.sciencedirect.com/science/article/pii/S096386950600027>>.
- FAN, C. et al. A comparison between ultrasonic array beamforming and super resolution imaging algorithms for non-destructive evaluation. **Ultrasonics**, v. 54, n. 7, p. 1842 – 1850, 2014. ISSN 0041-624X. Disponível em: <<http://www.sciencedirect.com/science/article/pii/S0041624X13003661>>.
- FELDMAN, M. Hilbert transform in vibration analysis. **Mechanical Systems and Signal Processing**, v. 25, n. 3, p. 735 – 802, 2011. ISSN 0888-3270.
- FESSLER, J. A.; SUTTON, B. P. Nonuniform fast Fourier transforms using min-max interpolation. **IEEE Transactions on Signal Processing**, v. 51, n. 2, p. 560–574, 2 2003. ISSN 1053-587X.

FRAZIER, C. H.; O'BRIEN, W. D. Synthetic aperture techniques with a virtual source element. **IEEE Transactions on Ultrasonics, Ferroelectrics, and Frequency Control**, v. 45, n. 1, p. 196–207, 1 1998. ISSN 0885-3010.

GARCIA, D. et al. Stolt's f-k migration for plane wave ultrasound imaging. **IEEE Transactions on Ultrasonics, Ferroelectrics, and Frequency Control**, v. 60, n. 9, p. 1853–1867, Sep. 2013. ISSN 0885-3010.

GOUVEIA, F. Tecnologia nacional para extrair petróleo e gás do pré-sal. **Conhecimento & Inovação**, v. 6, n. 1, p. 30–35, 2010. ISSN 1984-4395.

GUARNERI, G. A. **Identificação de descontinuidades em peças metálicas utilizando sinais ultrassônicos e técnicas de problemas inversos**. Tese (Doutorado) — Universidade Tecnológica Federal do Paraná, 2015.

GUARNERI, G. A. et al. A sparse reconstruction algorithm for ultrasonic images in nondestructive testing. **Sensors**, v. 15, n. 4, p. 9324–9343, 2015. ISSN 1424-8220. Disponível em: <<https://www.mdpi.com/1424-8220/15/4/9324>>.

HANGIANDREOU, N. J. AAPM/RSNA physics tutorial for residents: Topics in US. **RadioGraphics**, v. 23, n. 4, p. 1019–1033, 2003. Disponível em: <<https://doi.org/10.1148/rg.234035034>>.

HOLMES, C.; DRINKWATER, B. W.; WILCOX, P. D. Post-processing of the full matrix of ultrasonic transmit–receive array data for non-destructive evaluation. **NDT & E International**, v. 38, n. 8, p. 701 – 711, 2005. ISSN 0963-8695. Disponível em: <<http://www.sciencedirect.com/science/article/pii/S0963869505000721>>.

HOSKINS, P.; MARTIN, K.; THRUSH, A. **Diagnostic Ultrasound: Physics and Equipment**. 2nd. ed. [S.l.]: Cambridge University Press, 2010.

HU, H. et al. Ultrasonic sparse-TFM imaging for a two-layer medium using genetic algorithm optimization and effective aperture correction. **NDT & E International**, v. 90, p. 24 – 32, 2017. ISSN 0963-8695.

HUNTER, A. J.; DRINKWATER, B. W.; WILCOX, P. D. The wavenumber algorithm for full-matrix imaging using an ultrasonic array. **IEEE Transactions on Ultrasonics, Ferroelectrics, and Frequency Control**, v. 55, n. 11, p. 2450–2462, November 2008. ISSN 0885-3010.

JENSEN, J. A. et al. Synthetic aperture ultrasound imaging. **Ultrasonics**, v. 44, p. 5 – 15, 2006. ISSN 0041-624X. Proceedings of Ultrasonics International (UI'05) and World Congress on Ultrasonics (WCU).

JEUNE, L. L. et al. Adaptive ultrasonic imaging with the total focusing method for inspection of complex components immersed in water. **AIP Conference Proceedings**, v. 1650, n. 1, p. 1037–1046, 2015.

JEUNE, L. L.; ROBERT, S.; PRADA, C. Plane wave imaging for ultrasonic inspection of irregular structures with high frame rates. **AIP Conference Proceedings**, v. 1706, n. 1, p. 020010, 2016. Disponível em: <<https://aip.scitation.org/doi/abs/10.1063/1.4940456>>.

JEUNE, L. L. et al. Plane wave imaging for ultrasonic non-destructive testing: Generalization to multimodal imaging. **Ultrasonics**, v. 64, p. 128 – 138, 2016. ISSN 0041-624X. Disponível em: <<http://www.sciencedirect.com/science/article/pii/S0041624X15002188>>.

JIN, H. et al. Frequency-domain synthetic aperture focusing for helical ultrasonic imaging. **Journal of Applied Physics**, v. 121, n. 13, 2017.

JIN, H. et al. Frequency domain synthetic aperture focusing technique for variable-diameter cylindrical components. **The Journal of the Acoustical Society of America**, v. 142, n. 3, p. 1554–1562, 2017.

JOHNSON, S. G.; FRIGO, M. A modified split-radix FFT with fewer arithmetic operations. **IEEE Transactions on Signal Processing**, v. 55, n. 1, p. 111–119, Jan 2007. ISSN 1941-0476.

KOKOLEV, S. A.; BAZULIN, A. E.; BAZULIN, E. G. Application of linear interpolation for improving the quality of flaw images obtained by the spectral projection method during ultrasonic nondestructive testing. **Russian Journal of Nondestructive Testing**, v. 45, p. 823–837, 12 2009. ISSN 1608-3385.

KRUIZINGA, P. et al. Plane-wave ultrasound beamforming using a nonuniform fast fourier transform. **IEEE Transactions on Ultrasonics, Ferroelectrics, and Frequency Control**, v. 59, n. 12, p. 2684–2691, 12 2012. ISSN 0885-3010.

LATHI, B. P. **Signal Processing and Linear Systems**. 1st. ed. [S.l.]: Oxford University press, 2000.

LEHMANN, T. M.; GONNER, C.; SPITZER, K. Survey: interpolation methods in medical image processing. **IEEE Transactions on Medical Imaging**, v. 18, n. 11, p. 1049–1075, 11 1999. ISSN 1558-254X.

LI, Z.; WANG, J.; LIU, Q. H. Interpolation-free Stolt mapping for SAR imaging. **IEEE Geoscience and Remote Sensing Letters**, v. 11, n. 5, p. 926–929, May 2014. ISSN 1545-598X.

LINGVALL, F.; OLOFSSON, T.; STEPINSKI, T. Synthetic aperture imaging using sources with finite aperture: Deconvolution of the spatial impulse response. **The Journal of the Acoustical Society of America**, v. 114, n. 1, p. 225–234, 2003. Disponível em: <<https://doi.org/10.1121/1.1575746>>.

LINGVALL, F.; STEPINSKI, T. Two-dimensional synthetic focusing using large apertures—deconvolution of the spatial impulse response. **The Journal of the Acoustical Society of America**, v. 110, n. 5, p. 2660–2660, 2001. Disponível em: <<https://doi.org/10.1121/1.4777063>>.

LIU, J.; HE, Q.; LUO, J. A compressed sensing strategy for synthetic transmit aperture ultrasound imaging. **IEEE Transactions on Medical Imaging**, v. 36, n. 4, p. 878–891, April 2017. ISSN 0278-0062.

LU, J.-Y. 2D and 3D high frame rate imaging with limited diffraction beams. **IEEE Transactions on Ultrasonics, Ferroelectrics, and Frequency Control**, v. 44, n. 4, p. 839–856, July 1997. ISSN 0885-3010.

LUKOMSKI, T. Non-stationary phase shift migration for flaw detection in objects with lateral velocity variations. **Insight - Non-Destructive Testing and Condition Monitoring**, v. 56, n. 9, p. 477–482, 2014. ISSN 1354-2575.

LUKOMSKI, T. Full-matrix capture with phased shift migration for flaw detection in layered objects with complex geometry. **Ultrasonics**, v. 70, p. 241 – 247, 2016. ISSN 0041-624X.

MANTHEY, W.; KROEMER, N.; MAGORI, V. Ultrasonic transducers and transducer arrays for applications in air. **Measurement Science and Technology**, v. 3, p. 249–261, 1992.

MARGRAVE, G. F.; LAMOUREUX, M. P. **Numerical Methods of Exploration Seismology: With Algorithms in MATLAB**. [S.l.]: Cambridge University Press, 2019.

MATRONE, G. et al. Ultrasound plane-wave imaging with delay multiply and sum beamforming and coherent compounding. In: **2016 38th Annual International Conference of the IEEE Engineering in Medicine and Biology Society (EMBC)**. [S.l.: s.n.], 2016. p. 3223–3226. ISSN 1558-4615.

MERABET, L.; ROBERT, S.; PRADA, C. 2-D and 3-D reconstruction algorithms in the Fourier domain for plane-wave imaging in nondestructive testing. **IEEE Transactions on Ultrasonics, Ferroelectrics, and Frequency Control**, v. 66, n. 4, p. 772–788, April 2019. ISSN 0885-3010.

MOGHIMIRAD, E. et al. Synthetic aperture ultrasound Fourier beamformation using virtual sources. **IEEE Transactions on Ultrasonics, Ferroelectrics, and Frequency Control**, v. 63, n. 12, p. 2018–2030, Dec 2016. ISSN 0885-3010.

MONTALDO, G. et al. Coherent plane-wave compounding for very high frame rate ultrasonography and transient elastography. **IEEE Transactions on Ultrasonics, Ferroelectrics, and Frequency Control**, v. 56, n. 3, p. 489–506, March 2009. ISSN 0885-3010.

MORAIS, J. M. de. **Petróleo em águas profundas: uma história tecnológica da Petrobras**. [S.l.]: IPEA: Petrobras, 2013.

NAKAMURA, K. **Ultrasonic Transducers: Materials and Design for Sensors, Actuators and Medical Applications**. 1st. ed. [S.l.]: Woodhead Publishing, 2012. ISBN 1845699890.

NASCIMENTO, V. M. do. **Simulação do campo acústico de transdutores ultrassônicos de alta frequência do tipo array anular com e sem espaçamento entre anéis**. Tese (Doutorado) — Universidade Estadual de Campinas, 2013.

NG, A.; SWANEVELDER, J. Resolution in ultrasound imaging. **Continuing Education in Anaesthesia Critical Care & Pain**, v. 11, n. 5, p. 186–192, 08 2011. ISSN 1743-1816. Disponível em: <<https://doi.org/10.1093/bjaceaccp/mkr030>>.

OLOFSSON, T. Phase shift migration for imaging layered objects and objects immersed in water. **IEEE Transactions on Ultrasonics, Ferroelectrics, and Frequency Control**, v. 57, n. 11, p. 2522–2530, 11 2010. ISSN 0885-3010.

PENG, T. et al. Efficiency improvement of total focusing imaging based on sparse array method. In: **2014 IEEE Far East Forum on Nondestructive Evaluation/Testing**. [S.l.: s.n.], 2014. p. 61–65.

PRAGER, J. et al. SAFT and TOFD—a comparative study of two defect sizing techniques on a reactor pressure vessel mock-up. **Journal of Nondestructive Evaluation**, v. 32, n. 1, p. 1–13, 3 2013. ISSN 1573-4862. Disponível em: <<https://doi.org/10.1007/s10921-012-0153-9>>.

PROVOST, J. et al. 3D ultrafast ultrasound imaging in vivo. **Physics in Medicine and Biology**, v. 59, n. 19, p. L1–L13, sep 2014.

QIN, K.; YANG, C.; SUN, F. Generalized frequency-domain synthetic aperture focusing technique for ultrasonic imaging of irregularly layered objects. **IEEE Transactions on Ultrasonics, Ferroelectrics, and Frequency Control**, v. 61, n. 1, p. 133–146, 1 2014. ISSN 0885-3010.

RAILLON, R. et al. Validation of CIVA ultrasonic simulation in canonical configurations. In: **18th World conference on non-destructive testing, Durban, South Africa**. [S.l.: s.n.], 2012.

SANDRIN, L. et al. Shear modulus imaging with 2-D transient elastography. **IEEE Transactions on Ultrasonics, Ferroelectrics, and Frequency Control**, v. 49, n. 4, p. 426–435, April 2002. ISSN 0885-3010.

SCHIAVI, M. T.; HOFFMANN, W. A. M. Cenário petrolífero: sua evolução, principais produtores e tecnologias. **RDBCI: Revista Digital de Biblioteconomia e Ciência da Informação**, v. 13, n. 2, p. 259–278, 5 2015. Disponível em: <<https://periodicos.sbu.unicamp.br/ojs/index.php/rdbci/article/view/2104>>.

SCHIEFLER, N. T. et al. Generation and analysis of ultrasound images using plane wave and sparse arrays techniques. **Sensors**, v. 18, n. 11, 2018. ISSN 1424-8220. Disponível em: <<http://www.mdpi.com/1424-8220/18/11/3660>>.

SCHMERR, L. W. **Fundamentals of Ultrasonic Nondestructive Evaluation: A modeling approach**. [S.l.]: Springer Series in Measurement Science and Technology, 2016. ISBN 3319304615.

SHATTUCK, D. P. et al. Explososcan: A parallel processing technique for high speed ultrasound imaging with linear phased arrays. **Acoustical Society of America Journal**, v. 75, p. 1273–1282, April 1984.

SHULL, P. J. **Nondestructive evaluation: Theory, techniques, and applications**. [S.l.]: CRC Press, 2002. ISBN 0824788729.

SHUNG, K. K.; ZIPPURO, M. Ultrasonic transducers and arrays. **IEEE Engineering in Medicine and Biology Magazine**, v. 15, n. 6, p. 20–30, 11 1996. ISSN 0739-5175.

SILVERMAN, R. H. High-resolution ultrasound imaging of the eye – a review. **Clinical & Experimental Ophthalmology**, v. 37, n. 1, p. 54–67, 2009. Disponível em: <<https://onlinelibrary.wiley.com/doi/abs/10.1111/j.1442-9071.2008.01892.x>>.

SKJELVAREID, M. H. et al. Synthetic aperture focusing of ultrasonic data from multilayered media using an omega-k algorithm. **IEEE Transactions on Ultrasonics, Ferroelectrics, and Frequency Control**, v. 58, n. 5, p. 1037–1048, 5 2011. ISSN 0885-3010.

- Stanford Exploration Project. **Signs in Fourier transforms**. 1998. [Http://sepwww.stanford.edu/sep/prof/pvi/dft/paper\\_html/node18.html](http://sepwww.stanford.edu/sep/prof/pvi/dft/paper_html/node18.html). Accessed: 12/05/2020.
- STEPINSKI, T. An implementation of synthetic aperture focusing technique in frequency domain. **IEEE Transactions on Ultrasonics, Ferroelectrics, and Frequency Control**, v. 54, n. 7, p. 1399–1408, 7 2007. ISSN 0885-3010.
- STOLT, R. H. Migration by Fourier transform. **Geophysics**, v. 43, n. 1, p. 23–48, 1978. Disponível em: <<https://doi.org/10.1190/1.1440826>>.
- SUTCLIFFE, M. et al. Real-time full matrix capture for ultrasonic non-destructive testing with acceleration of post-processing through graphic hardware. **NDT & E International**, v. 51, p. 16 – 23, 2012. ISSN 0963-8695. Disponível em: <<http://www.sciencedirect.com/science/article/pii/S0963869512000850>>.
- THOMSON, R. Transverse and longitudinal resolution of the synthetic aperture focusing technique. **Ultrasonics**, v. 22, n. 1, p. 9 – 15, 1984. ISSN 0041-624X. Disponível em: <<http://www.sciencedirect.com/science/article/pii/0041624X84900556>>.
- WADE, G. **Acoustic imaging: cameras, microscopes, phased arrays, and holographic systems**. 1st. ed. [S.l.]: Plenum Publishing Corp, 1975.
- WELLS, P. N. T.; LIANG, H.-D. Medical ultrasound: imaging of soft tissue strain and elasticity. **Journal of The Royal Society Interface**, v. 8, n. 64, p. 1521–1549, 2011. Disponível em: <<https://royalsocietypublishing.org/doi/abs/10.1098/rsif.2011.0054>>.
- WELVAERT, M.; ROSSEEL, Y. On the definition of signal-to-noise ratio and contrast-to-noise ratio for fMRI data. **PLOS ONE**, Public Library of Science, v. 8, n. 11, p. 1–10, 11 2013. Disponível em: <<https://doi.org/10.1371/journal.pone.0077089>>.
- WESTON, M. et al. Time efficient auto-focussing algorithms for ultrasonic inspection of dual-layered media using full matrix capture. **NDT & E International**, v. 47, p. 43 – 50, 2012. ISSN 0963-8695. Disponível em: <<http://www.sciencedirect.com/science/article/pii/S0963869511001526>>.
- WOO, J. **A short History of the development of Ultrasound in Obstetrics and Gynecology**. 2002. Disponível em: <<http://www.ob-ultrasound.net/history1.html>>.
- WU, H. et al. Ultrasonic array imaging of multilayer structures using full matrix capture and extended phase shift migration. **Measurement Science and Technology**, IOP Publishing, v. 27, n. 4, p. 045401, 3 2016.
- WU, S. et al. Synthetic aperture imaging for multilayer cylindrical object using an exterior rotating transducer. **Review of Scientific Instruments**, v. 86, n. 8, p. 083703, 2015.
- YANG, M. et al. High volume rate, high resolution 3D plane wave imaging. In: **2014 IEEE International Ultrasonics Symposium**. [S.l.: s.n.], 2014. p. 1253–1256. ISSN 1051-0117.
- YANG, Y. et al. Efficient imaging techniques using sub-aperture matrix capture and two-dimensional sparse array. In: **2014 IEEE Far East Forum on Nondestructive Evaluation/Testing**. [S.l.: s.n.], 2014. p. 44–49.

## APPENDIX A – TIME-DOMAIN PROCESSING TECHNIQUES

Although this study focused on frequency-domain techniques for the post-processing of ultrasonic data, time-domain techniques constitute an important class of processing algorithms. The DAS technique is a well-known time-domain method, which reconstructs an image by coherently summing samples of the ultrasonic signals considering the wave propagation time. Several ultrasound scanners have dedicated hardware to implement the DAS technique and provide real-time images of the inspected object. In this chapter of the Appendix, three common time-domain algorithms are presented for reference. Each algorithm corresponds to the sweep, FMC and PWI capture modes.

### A.1 SAFT

The SAFT algorithm is used to process data from sweep inspections. The technique is based on the DAS approach, which reconstructs each point of the image by combining echo signals received by the transducer at different positions (THOMSON, 1984; FRAZIER; O'BRIEN, 1998; LINGVALL et al., 2003; PRAGER et al., 2013). As Figure 5 shows, a transducer can detect signals from nearby flaws. Thus, signals detected by the transducer at a certain position can be verified by echo signals received when the transducer is at a different position.

Figure 47 shows the operation principle of the DAS algorithm, where Figure 47a represents reconstruction of column zero of the image and Figure 47b represents reconstruction of column two of the image. In addition, the figure represents A-scan signals obtained from a sweeping inspection, such as the one illustrated in Figure 15, where  $x_0$ ,  $x_1$ ,  $x_2$ ,  $x_3$  and  $x_4$  represents the various positions at which A-scan signals were acquired by the transducer.

At location  $x_0$ , the A-scan signal from the transducers has a typical characteristic of an echo signal originated from a flaw, which could indicate a flaw inside the object at this location. However, this information is not verified by any other measurement made by the transducer at other locations. For instance, during reconstruction of column 0 of the image, the A-scan signal recorded by the transducer at  $x_0$  has a peak, highlighted by a green triangle. If this peak is due to a flaw present at location  $x_0$ , the A-scan signal recorded at location  $x_1$

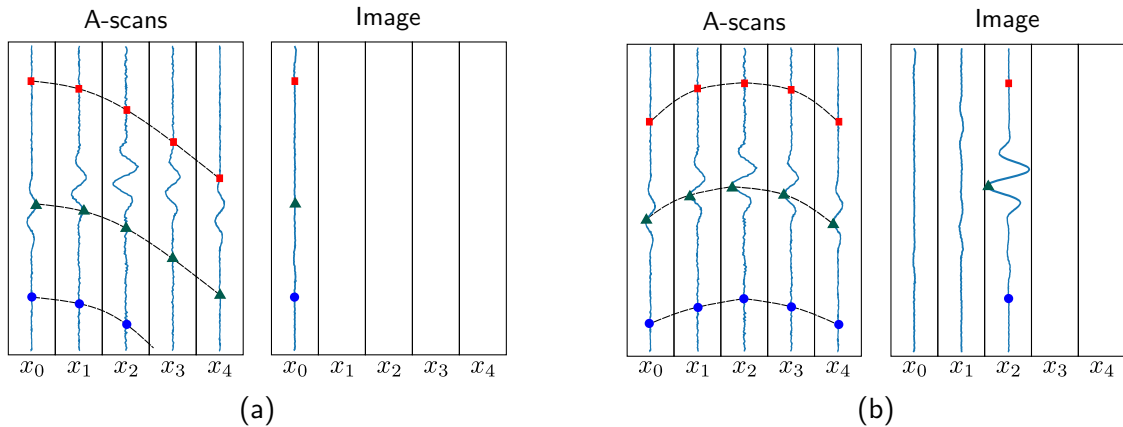


**Figure 47: Basic concept of the DAS algorithm for image reconstruction from A-scan signals. The algorithm reconstructs the image pixel by pixel, by combining samples of the echo signals obtained from the transducer at different locations. Each column of the A-scans matrix corresponds to one A-scan signal obtained by the transducer at a different location. The image matrix represents the reconstructed image. (a) Reconstruction of column 0 of the image results in the summation of incoherent samples and produces a signal with low amplitude, whereas (b) reconstruction of column 2 of the image results in summation of coherent samples and produces a signal with high amplitude.**

would show a peak; however, with a *delay* with respect to the peak detected at  $x_0$ . However, this does not happen, and the samples at adjacent positions, also highlighted by a green triangle, do not show oscillations, which does not indicate a flaw at  $x_0$ . On the other hand, reconstruction of column 2 of the image shows a flaw that is verified by other measurements made by the transducer. For instance, the peak value of the flaw at location  $x_2$  is seen at other A-scan signals, with a delay with respect to the position  $x_2$ .

Following this concept, summing samples that contain information about the same point on the object generates a high amplitude signal if the signals are coherent and a low amplitude signal if the signals are incoherent. The DAS algorithm consists of forming each point of the image from the delay-and-sum of samples from the A-scan signals that contribute to that point. In addition, the DAS technique can improve signal-to-noise ratio (SNR). Noise comes mainly from the electronic acquisition system (MONTALDO et al., 2009) and produces random fluctuations on the A-scan signals. Coherent summation of the signals cancel these random fluctuations and can improve the SNR of the reconstructed signals. This is shown in Figure 47b, where the oscillations on the reconstructed signal are much larger than the noise, in contrast to the A-scan signal without processing.

The delay applied to the samples for summation is related to the location of the points on the image, to the position of the transducer and to the wave velocity. Figure 48 shows the distance  $d_{t,o}$  between the transducer at location  $(x_t, 0)$  and a point on the object located at  $(x_o, z_o)$ . The wave emitted by the transducer travels a distance  $d_{t,o} = \sqrt{(x_t - x_o)^2 + z_o^2}$  until it reaches point  $(x_o, z_o)$ . If there is an echo signal at this location, the echo will travel

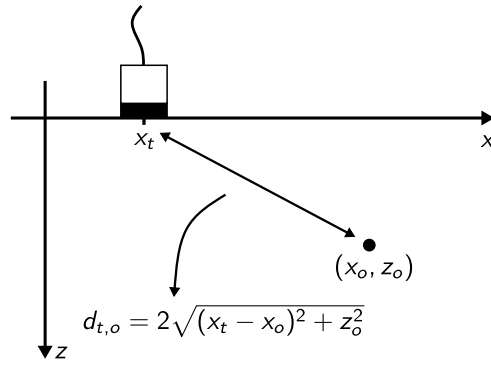


**Figure 48: Distance between the transducer and a point on the object.**

the same distance until it reaches the transducer and, thus, the total distance traveled by the wave is  $d = 2d_{t,o}$ . The wave's propagation time will be given by:

$$\tau_{t,o} = \frac{2\sqrt{(x_t - x_o)^2 + z_o^2}}{c}, \quad (43)$$

where  $c$  is the wave propagation velocity on the object. Thus, if  $s(x_t, t)$  is the A-scan signal of the transducer at location  $x_t$ , sample  $s(x_t, \tau_{t,o})$  contains information about location  $(x_o, z_o)$  of the object. To reconstruct the image  $o$  at location  $(x_o, z_o)$ , samples of the A-scan signals obtained by the transducer at the several locations are summed:

$$o(x_o, z_o) = \sum_{i=0}^{N-1} s(x_i, \tau_{i,o}), \quad (44)$$

where  $N$  represents the number of steps by the transducer. Generally, the propagation time between the transducer at location  $x_t$  and an arbitrary point on the object is given by:

$$\tau(x_t, x, z) = \frac{2\sqrt{(x_t - x)^2 + z^2}}{c}, \quad (45)$$

and an image of the object at an arbitrary location  $(x, z)$  is given by:

$$o(x, z) = \sum_{i=0}^{N-1} s(x_i, \tau(x_i, x, z)). \quad (46)$$

Equations 45 and 46 constitute the basic principle for the DAS method and the SAFT algorithm, shown in Algorithm 5. Its execution requires as input the points on the object where the image is desired (vectors  $x$  and  $z$ , of size  $N_x$  and  $N_z$ ; respectively), the raw ultrasonic data (matrix  $s$ , of size  $(N_t, N_{x_t})$ ), the positions at which the transducer performed the inspection (vector  $x_t$ , of size  $N_{x_t}$ ), the wave speed (scalar  $c$ ) and the sampling period of the A-scan signals (scalar  $t_s$ ). The output of the algorithm is the reconstructed image of the internal structure of the object (matrix  $o$ , of size  $(N_z, N_x)$ ).

---

**Algorithm 5** Pseudocode for the SAFT algorithm.
 

---

**Require:**  $x$  (a vector of size  $N_x$ ),  $z$  (a vector of size  $N_z$ ),  $s$  (a matrix of size  $(N_t, N_{x_t})$ ),  $x_t$  (a vector of size  $N_{x_t}$ ),  $c$  (a scalar),  $t_s$  (a scalar)

**Ensure:**  $o$  (a matrix of size  $(N_z, N_x)$ )

- 1:  $o = \text{zeros}(N_z, N_x)$  ▷ Initializes the output matrix with zeros
  - 2: **for**  $i = 0, 1, \dots, N_z - 1$  **do**
  - 3:   **for**  $j = 0, 1, \dots, N_x - 1$  **do**
  - 4:     **for**  $k = 0, 1, \dots, N_{x_t} - 1$  **do**
  - 5:        $\tau \leftarrow 2\sqrt{(x_t[k] - x[j])^2 + z[i]^2}/c$
  - 6:        $\tau_{\text{id}x} = \text{round}(\tau/t_s)$
  - 7:        $o[i, j] \leftarrow o[i, j] + s[\tau_{\text{id}x}, k]$
  - 8:     **end for**
  - 9:   **end for**
  - 10: **end for**
- 

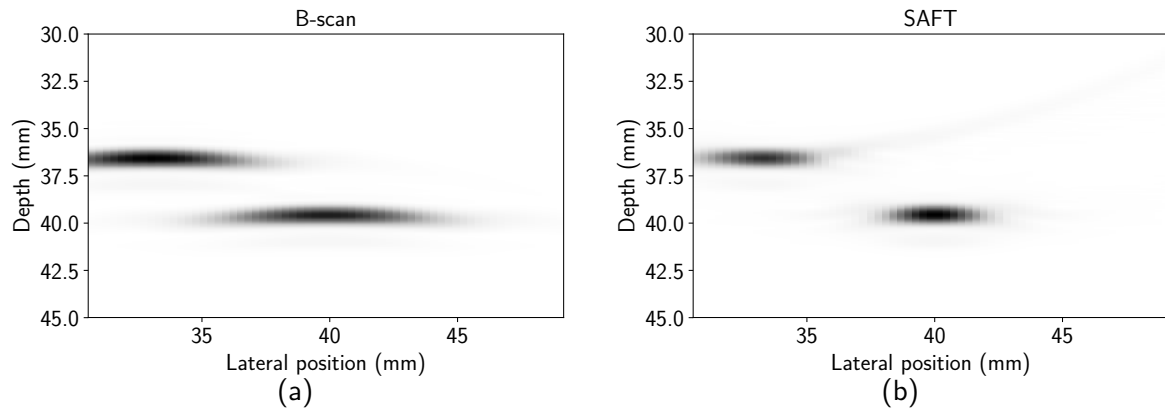


**Figure 49: (a) B-scan image and (b) image obtained with the SAFT algorithm. After processing, the flaws appear more concentrated on their respective locations.**

The algorithm consists of looping through all image points and, for each point, looping for every position the transducer acquired echo signals. For each such position, the propagation time is computed, transformed into an index and the corresponding sampled is summed to the image point.

Figure 49 shows a B-scan image obtained from a sweeping simulation on the specimen indicated in Figure 18. From the B-scan image, indicated in Figure 49a, it is possible to identify two flaws on the specimen, which appear with a hyperbolic aspect. However, after processing of the A-scan signals with the SAFT algorithm, the flaws appear more concentrated on their respective locations, as shown in Figure 49b.

## A.2 TFM

The TFM algorithm is used to process data from an FMC and it is also based on the DAS technique. Image reconstruction from the FMC data set is similar to image reconstruction with the SAFT method. The main difference is that the FMC contains ultrasonic echo signals

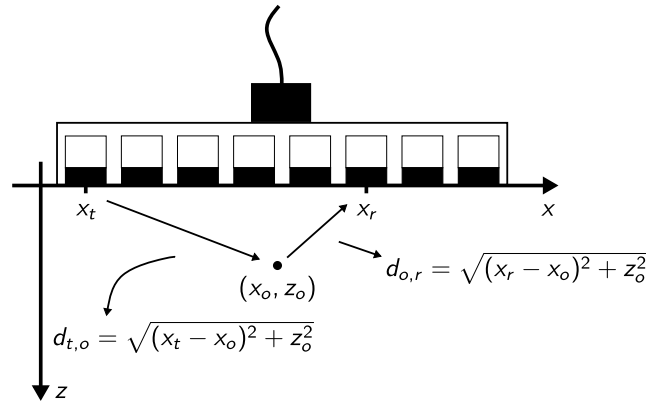
for all combinations of emitters and receivers of the linear array transducer, condensed in a 3-D matrix. In the FMC acquisition scheme, each element of the transducer emits an ultrasonic pulse, while all elements receive echo signals. This process obtains a B-scan image for each element that emitted a pulse. By processing and combining the data from all elements that emitted a pulse, it is possible to obtain a single image with higher resolution (HOLMES et al., 2005; JENSEN et al., 2006; FAN et al., 2014).

Figure 50 shows the distance traveled by the wave on the FMC acquisition method. First, an element of the transducer at position  $x_t$  emits an ultrasonic pulse that propagates through the object with velocity  $c$  and reaches a point  $(x_o, z_o)$ , after traveling a distance  $d_{t,o} = \sqrt{(x_t - x_o)^2 + z_o^2}$ . If there is a reflector at this position, the wave is reflected and reaches another element of the transducer, at a position  $x_r$ , after traveling a distance  $d_{r,o} = \sqrt{(x_r - x_o)^2 + z_o^2}$ . After an emission by one element, the ultrasonic pulse is received by another element after a time  $\tau$  is given by:

$$\tau(x_t, x_r, x, z) = \frac{\sqrt{(x_t - x)^2 + z^2} + \sqrt{(x_r - x)^2 + z^2}}{c}. \quad (47)$$

If  $s(x_{(T,R)}, t)$  is the echo signal from the A-scan corresponding to emission of element  $T$  and reception by element  $R$ , the sample  $s(x_{(T,R)}, \tau(x_t, x_r, x, z))$  contains information about point  $(x, z)$  of the object. As in the SAFT algorithm, a point on the object can be reconstructed from the summation of the samples of each receiving element. However, each element is also an emitter. Thus, the image at a location  $(x, z)$  on the object can be reconstructed by combining all receiving and emitting from the  $N$  elements (JENSEN et al., 2006):

$$o(x, z) = \sum_{j=0}^{N-1} \sum_{i=0}^{N-1} s(x_{(j,i)}, \tau(x_j, x_i, x, z)). \quad (48)$$



**Figure 50: Distance between an emitter, a receptor and a point on the object, for the FMC acquisition method.**

---

**Algorithm 6** Pseudocode for the TFM algorithm.
 

---

**Require:**  $x$  (a vector of size  $N_x$ ),  $z$  (a vector of size  $N_z$ ),  $s$  (a matrix of size  $(N_t, N_{x_t}, N_{x_t})$ ),  $x_t$  (a vector of size  $N_{x_t}$ ),  $c$  (a scalar),  $t_s$  (a scalar)

**Ensure:**  $o$  (a matrix of size  $(N_z, N_x)$ )

```

1:  $o = \text{zeros}(N_z, N_x)$  ▷ Initializes the output matrix with zeros
2: for  $i = 0, 1, \dots, N_z - 1$  do
3:   for  $j = 0, 1, \dots, N_x - 1$  do
4:     for  $u = 0, 1, \dots, N_{x_t} - 1$  do
5:       for  $v = 0, 1, \dots, N_{x_t} - 1$  do
6:          $\tau \leftarrow \left( \sqrt{(x_t[u] - x[j])^2 + z[i]^2} + \sqrt{(x_t[v] - x[j])^2 + z[i]^2} \right) / c$ 
7:          $\tau_{\text{idx}} = \text{round}(\tau / t_s)$ 
8:          $o[i, j] \leftarrow o[i, j] + s[\tau_{\text{idx}}, u, v]$ 
9:       end for
10:    end for
11:  end for
12: end for

```

---

A pseudo-code for the TFM algorithm is shown in Algorithm 6. The execution of the TFM algorithm requires as input the points on the object where the image is desired (vectors  $x$  and  $z$ , of size  $N_x$  and  $N_z$ ; respectively), the FMC data set (matrix  $s$ , of size  $(N_t, N_{x_t}, N_{x_t})$ ), the position of each element of the transducer (vector  $x_t$ , of size  $N_{x_t}$ ), the wave speed (scalar  $c$ ) and the sampling period of the A-scan signals (scalar  $t_s$ ). The output is an image of the object (matrix  $o$ , of size  $(N_z, N_x)$ ).

The algorithm loops for each point of the image and, for each point, the algorithm loops for all emitters and for all receivers. For each receiver, the propagation time is computed, converted into an index and the corresponding sample is accumulated on the image point.

Figure 51 shows a comparison between the B-scan image obtained from an FMC, as well as the reconstructed images obtained from the SAFT and TFM algorithms, with ultrasonic data from the simulation on the specimen shown in Figure 18. The B-scan image, shown in Figure 51a, corresponds to the image obtained with A-scan data from the diagonal of an FMC, which represents a sweeping inspection. This B-scan image can be processed by the SAFT algorithm, which reconstructs the image shown in Figure 51b. The last image, displayed in Figure 51c, shows the image reconstructed with the TFM algorithm. As Figure 51 shows, it is difficult to identify flaws on the object from the B-scan image obtained with the linear array transducer. After processing the B-scan image with the SAFT algorithm, the location of the flaws become more precise. The FMC data set processed with the TFM algorithm also reconstructs an image in which the location of the flaws is more accurate, with a lower amount of artifacts.

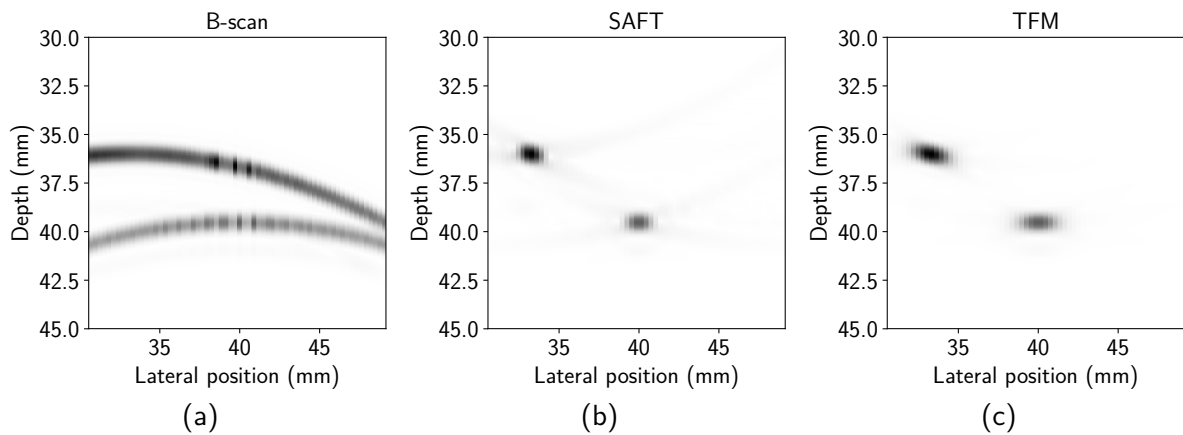


**Figure 51: (a) B-scan image generated with A-scan data from the diagonal of an FMC, (b) B-scan image processed with the SAFT algorithm and (c) image reconstructed with the TFM algorithm. Location of flaws are unclear from the B-scan image, whereas the image obtained with the SAFT algorithm show the flaws more precisely, albeit some artifacts. The FMC data processed with the TFM algorithm reconstructs an image with few artifacts and the flaws can be more accurately located.**

Although the TFM is considered as the standard for FMC processing, the algorithm presents a high computational cost. Alternative algorithms based on the TFM have been proposed to reduce its computational cost, as well as the data volume of an FMC. One of the proposed techniques is the use of sparse matrices, where only a subset of the elements of the transducer are used for transmission and reception, reducing the volume of data (PENG et al., 2014; YANG et al., 2014b; HU et al., 2017; BANNOUF et al., 2013). In the work developed by Peng et al. (2014), the authors showed that the use of only 1/4 of the elements from a linear array can generate results with performance metrics similar to images generated by processing the full data set. Reduction on the number of elements has also been extended for 3-D imaging with 2-D phased array transducers, in the work proposed by Yang et al. (2014b). Moreover, it is possible to determine the optimal set of elements that must be used to produce a better beam pattern. Bannouf et al. (2013) developed an algorithm that determines the optimal set of elements based on restrictions imposed on the desired beam pattern, obtaining a reduction of 4 times on processing time and on volume of data. In the work developed by Hu et al. (2017), genetic algorithms were applied to determine the best layout for emitting and receiving elements, obtaining a computational gain up to 4 times on image reconstruction.

Initially, the TFM was developed for inspections on plane surfaces. However, its adaptation to irregular (or complex) surfaces has been investigated. In the work developed by Jeune et al. (2015), the authors proposed an adaptation of the TFM algorithm for immersion testings with complex surfaces. Their approach consists of first detecting the surface of the object, applying the TFM algorithm in a second step. The results obtained showed that the method is robust for different surfaces, allowing the detection of flaws on test pieces.

### A.3 CPWC

In plane-wave acquisitions, all elements of the transducer are excited such that the waves emitted by each element interfere to result in a single wavefront. Since the resulting plane-wave does not have focus, several plane-waves with different angles can be emitted into the medium, to acquire different views from the same target. The several images obtained from each emission can then be processed and combined, leading to a final image with higher contrast and resolution. Initial applications of PWI considered the incoherent compounding of the partial images, in order to increase the signal-to-noise ratio (SNR). However, *coherent* plane-wave compounding has shown better results, and has been adopted as the standard tool to process plane-wave acquisition data (MONTALDO et al., 2009).

The CPWC algorithm employs the DAS method to reconstruct one image for each wave emitted into the object. Images reconstructed with waves emitted at different steering angles can then be compounded to result in a single image. Figure 52 shows the distance traveled by a plane-wave, since its origin, to a point  $(x_o, z_o)$  on the object and back to the surface. After emission of the wave, the time  $\tau$  required for the echo signals to reach a receiving element, located at  $x_r$ , is given by (MONTALDO et al., 2009):

$$\tau(\theta, x_r, x_o, z_o) = \frac{z_o \cos \theta + x_o \sin \theta + \sqrt{(x_r - x_o)^2 + z_o^2}}{c}, \quad (49)$$

where  $\theta$  is the angle of the emitted plane-wave and  $c$  is the wave velocity. If  $s(\theta, x_r, t)$  is the echo signal of element  $x_r$  from emission with steering angle  $\theta$ , a single image can be obtained for each plane-wave emission and all the reconstructed images can then be compounded into a single image:

$$o(x, z) = \sum_{j=0}^{M-1} \sum_{i=0}^{N-1} s(\theta_j, x_i, \tau(\theta_j, x_i, x, z)), \quad (50)$$

where  $N$  is the number of transducer elements and  $M$  is the number of emitted plane-waves.

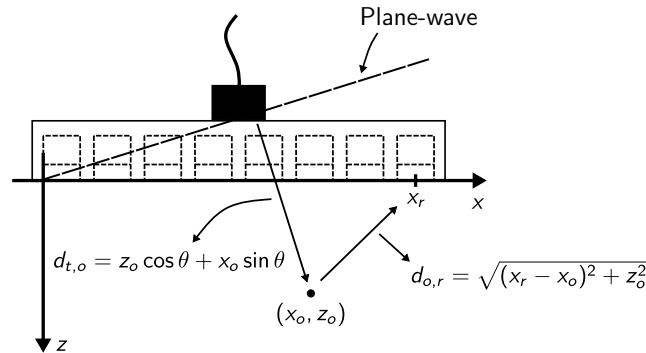


**Figure 52: Distance between the plan-wave, a receptor and a point on the object, for the plane-wave acquisition method.**

---

**Algorithm 7** Pseudocode for the CPWC algorithm.
 

---

**Require:**  $x$  (a vector of size  $N_x$ ),  $z$  (a vector of size  $N_z$ ),  $s$  (a matrix of size  $(N_t, N_\theta, N_{x_t})$ ),  $x_t$  (a vector of size  $N_{x_t}$ ),  $\theta$  (a vector of size  $N_\theta$ ),  $c$  (a scalar),  $t_s$  (a scalar)

**Ensure:**  $o$  (a matrix of size  $(N_z, N_x)$ )

```

1:  $o = \text{zeros}(N_z, N_x)$  ▷ Initializes the output matrix with zeros
2: for  $k = 0, 1, \dots, N_\theta - 1$  do
3:   for  $i = 0, 1, \dots, N_z - 1$  do
4:     for  $j = 0, 1, \dots, N_x - 1$  do
5:       for  $u = 0, 1, \dots, N_{x_t} - 1$  do
6:          $\tau_{\text{fwd}} \leftarrow \frac{z[i] \cos(\theta[k]) + x[j] \sin(\theta[k])}{c}$ 
7:          $\tau_{\text{bwd}} \leftarrow \frac{\sqrt{(x_t[u] - x[j])^2 + z[i]^2}}{c}$ 
8:          $\tau_{\text{idx}} \leftarrow \text{round}((\tau_{\text{fwd}} + \tau_{\text{bwd}})/t_s)$ 
9:          $o[i, j] \leftarrow o[i, j] + s[\tau_{\text{idx}}, \theta[k], u]$ 
10:      end for
11:    end for
12:  end for
13: end for

```

---

Algorithm 7 shows a pseudocode for the implementation of the CPWC algorithm. The CPWC algorithm requires as input the points on the object where the image is desired (vectors  $x$  and  $z$ , of size  $N_x$  and  $N_z$ ; respectively), the PWI data set (matrix  $s$ , of size  $(N_t, N_\theta, N_{x_t})$ ), the position of each element of the transducer (vector  $x_t$ , of size  $N_{x_t}$ ), the set of angles used for inspection (vector  $\theta$ , of size  $N_\theta$ ), the wave propagation velocity (scalar  $c$ ) and the sampling period of the A-scan signals (scalar  $t_s$ ). The output is the compounded image obtained, representing the internal structure of the inspected object (matrix  $o$ , of size  $(N_z, N_x)$ ).

The algorithm consists in looping for each angle, each point of the image and each element of the transducer. For each element, the propagation times are computed and converted into an index. The corresponding samples are then summed to the image point.

Figure 53 compares the B-scan image and the image reconstructed with the CPWC algorithm, with data from the simulated specimen (Figure 18). For testing, a set of 21 angles was used, with an initial angle of  $-10^\circ$ , a final angle of  $10^\circ$  and a step of  $1^\circ$ . Thus, the final image was obtained from the compounding of the 21 partial images reconstructed from each angle. For the PWI inspection, the B-scan image was defined as the A-scan signals from the wave with steering angle of  $\theta = 0^\circ$ . As Figure 53a shows, the B-scan image produced by the plane-wave acquisition is similar to the image obtained from the FMC acquisition, where the internal structure of the object is unclear. However, after processing of the PWI data set with the CPWC algorithm, location of the flaws contained in the object can be determined more precisely, as shown in Figure 53b.

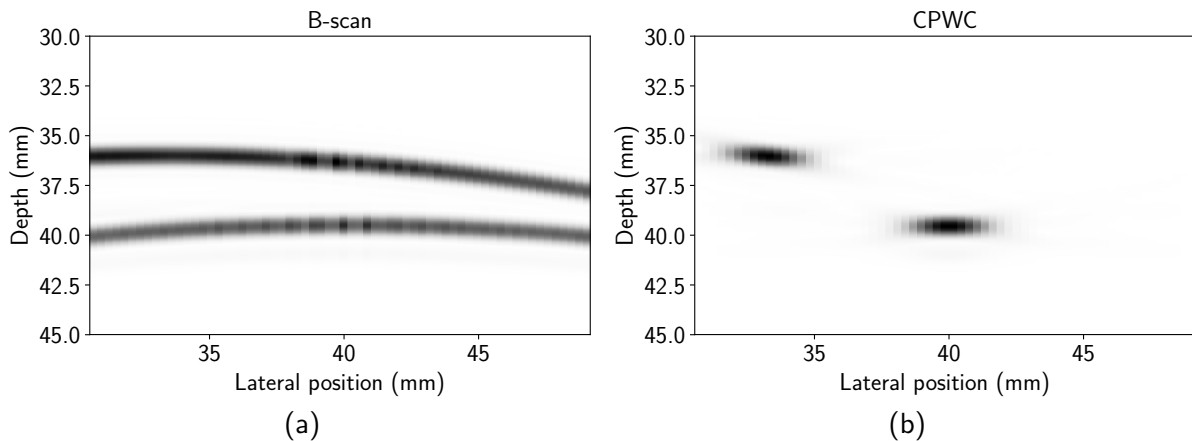


**Figure 53: (a) B-scan image and (b) image obtained with the CPWC algorithm. The B-scan image, defined as the image obtained for an emission angle of  $\theta = 0^\circ$ , is difficult to interpret. After processing and compounding the set of 21 images, the flaws can be more accurately determined.**

PWI has been reported in the literature as a good alternative to the FMC acquisition method (MONTALDO et al., 2009; JEUNE et al., 2016b). Montaldo et al. (2009) have studied usage of PWI and CPWC in medical imaging as an alternative to the standard multifocus imaging. The authors showed that, in general, PWI is able to attain images with the same quality as multifocus imaging, using 10 times less emissions, which translates to a reduction in data volume and in a higher frame rate. Achieving higher frame rates whilst maintaining image quality has allowed faster 3-D imaging, which has led to new studies in the medical field (PROVOST et al., 2014; YANG et al., 2014a). For NDT, the CPWC algorithm has been applied for ultrasound inspections by Jeune et al. (2016b). The authors adapted the CPWC algorithm for immersion testings and multimodal imaging. In their study, they compared PWI with the standard FMC technique, concluding that PWI is able to produce images with quality aspects similar to those produced by FMC, with a threefold reduction on emissions and data volume.

Further reduction in data volume and increase in frame-rate has been actively researched. Recent studies have evaluated the effects on the reduction of transducer elements used during the reception of echo signals. In the work developed by Schiefler et al. (2018), the authors proposed to use PWI with a lower number of receiving elements, using interpolation to estimate the missing data. They applied this for medical ultrasound imaging and concluded that usage of 65 elements out of a 128-element transducer generates image quality metrics similar to the images generated by usage of the full set of elements.

Several algorithms for ultrasonic imaging have also been studied and adapted to PWI. The delay-multiply and sum (DMAS), originally developed for radar, was adapted to multifocal medical imaging and later applied to PWI. Matrone et al. (2016) showed that the

DMAS adapted to PWI can lead to a three-fold reduction in emissions and thus, a three-fold increase in frame-rate in medical imaging. Algorithms based on signal statistics, such as the minimum variance beamformer, were also adapted to PWI (AUSTENG et al., 2011).

Plane-wave image reconstruction has also been studied with compressed sensing. In the study conducted by David et al. (2015), the authors reconstructed complex images of point reflectors with a single plane-wave emission. In the work developed by Besson et al. (2016a), the authors proposed ultrasonic image reconstruction as a discrete inverse problem. They were able to obtain images with quality metrics similar to conventional methods; however, in addition to using only a single plane-wave, they used only a subset of the elements of the transducer. Although these methods have shown promising results, the algorithms developed often required adjustments which could depend on the image to be reconstructed, preventing its use to practical applications. Execution time has also been a restriction, since these algorithms rely on optimization of complex objective functions and image reconstruction can take hours (LIU et al., 2017).

## APPENDIX B – EFFECT OF OVERSAMPLING ON STOLT’S MIGRATION

In Section 5.4, two similar experiments produced very different results. When the ROI contained only SDHs, algorithms using piecewise linear interpolation had the oversampling factor increased until the CNR of the reconstructed image matched the CNR of images obtained with algorithms using frequency shifts. In this case, with the same CNR, the oversampling factor indicates which algorithm has a shorter execution time. However, when the ROI contained the bottom of the imaged object, high values of the oversampling factor for algorithms using piecewise linear interpolation were required in order to match the CNR of the images produced by algorithms using frequency shifts. In these cases, the execution time for algorithms using frequency shifts was always lower.

The reason for these results may be related to the frequency content of each image. Figure 54 shows the magnitude of the reconstructed spectrum of a single flaw and the magnitude of the reconstructed spectrum of the bottom of the object, along with the images obtained from these spectra. The reconstructed spectra are from simulation of a sweeping inspection with a monostatic transducer, using the CIVA software (see Section 2.1.5 for details on the CIVA simulator). Figure 54a shows the reconstructed spectrum when the A-scan signals contain a single flaw, and the image obtained from this spectrum is shown in Figure 54b. Figure 54c shows the reconstructed spectrum when the A-scan signals contain only the bottom of the object, and the image obtained from this spectrum is shown in Figure 54d. As Figure 54 shows, the coefficients of the spectrum of the flaw span a wider range of frequencies, whereas the coefficients of an image containing the bottom of the object are more concentrated on a more narrow range of frequencies.

The effect of varying the oversampling factor during the reconstruction of the image containing the single flaw is shown in Figure 55. Figure 55a shows the magnitude of the spectrum reconstructed when the oversampling factor is 13.94. The image obtained from this spectrum is shown in Figure 55b. The flaw is reconstructed with no apparent artifacts on the image. Lowering the oversampling factor to 6.97 produces the spectrum shown in Figure 55c. This spectrum is clearly different from the spectrum of Figure 55a. However, as Figure 55d shows, the image obtained from the spectrum reconstructed from an oversampling factor of 6.97 is similar to the image obtained from reconstruction with an oversampling factor of

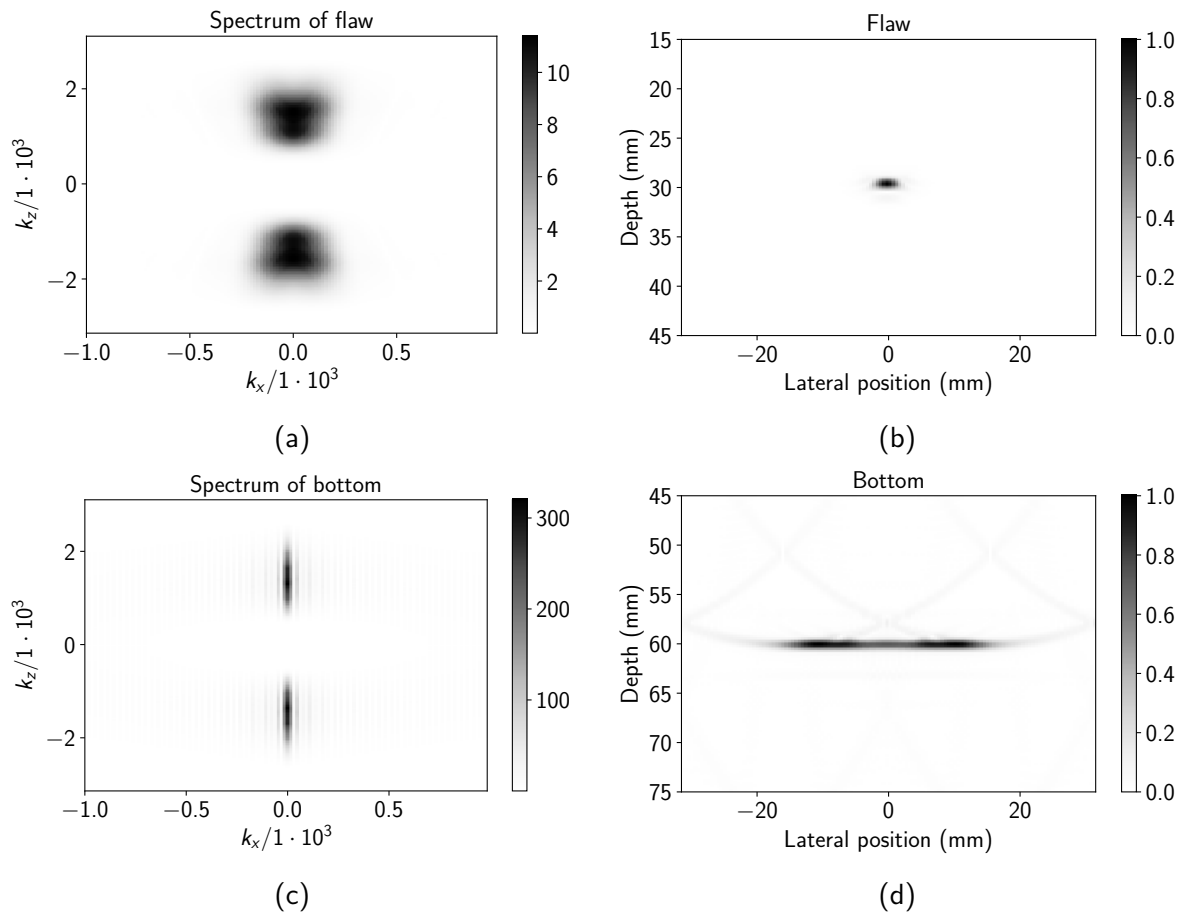


**Figure 54:** (a) Magnitude of the reconstructed spectrum from A-scan signals containing a single flaw and (b) the resulting image, (c) magnitude of the reconstructed spectrum from A-scan signals containing only the bottom of the object and (d) the resulting image.

13.94. Lowering the oversampling factor further down to 3.49 produces a spectrum which its magnitude is shown in Figure 55e. This spectrum seems to be even more distorted if compared to the spectrum shown in Figure 55a; however, the image obtained, shown in Figure 55f, is still similar to the image shown in Figure 55b.

The effect of varying the oversampling factor during the reconstruction of the image containing the bottom of the object is shown in Figure 56. As Figure 56 shows, reconstruction of the image from the spectrum of the bottom is much more sensitive to the oversampling factor. Decreasing oversampling factor from 13.94 to 3.49 produces an image where the bottom of the object appears to be misplaced. This strongly affects the CNR of the reconstructed image, since the misplaced signal will be considered as noise.

The spectra of the flaw and bottom, as reconstructed by the NNS- $\omega k$ -SAFT algorithm, are shown in Figure 57. In this case, even without using an oversampled FFT, the spectra are reconstructed similar to the spectra obtained with the  $\omega k$ -SAFT algorithm with an oversampling factor of 13.94. Hence, the NNS- $\omega k$ -SAFT algorithm is more advantageous reconstructing images with flaws which are more sensitive to interpolation errors, while the

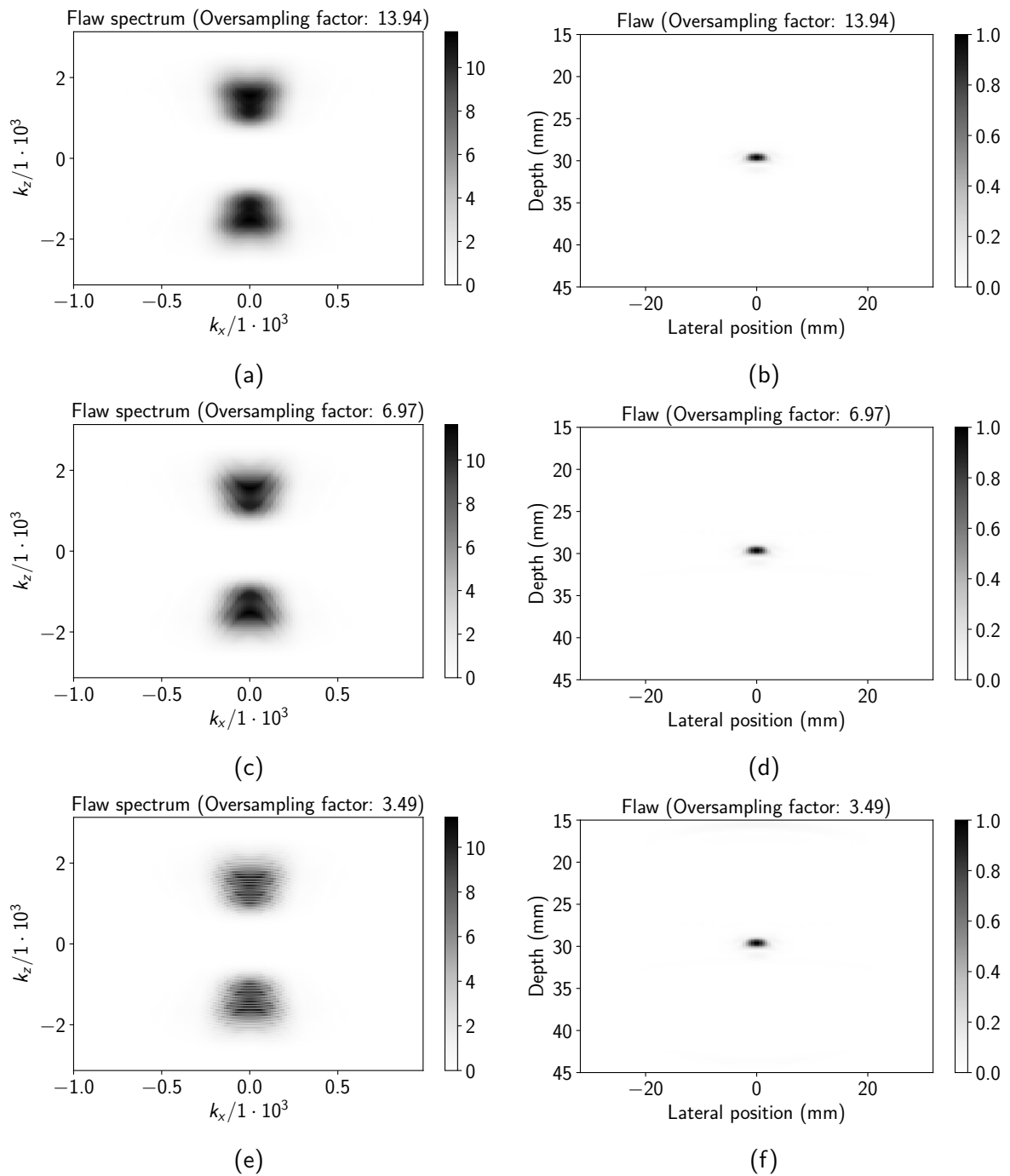


**Figure 55: Spectrum of the flaw reconstructed with (a) an oversampling factor of 13.94 and (b) reconstructed image, (c) an oversampling factor of 6.97 and (d) reconstructed image, (e) an oversampling factor of 3.49 and (f) reconstructed image.**

$\omega k$ -SAFT algorithm may be more advantageous reconstructing images with flaws which are less sensitive to interpolation errors.

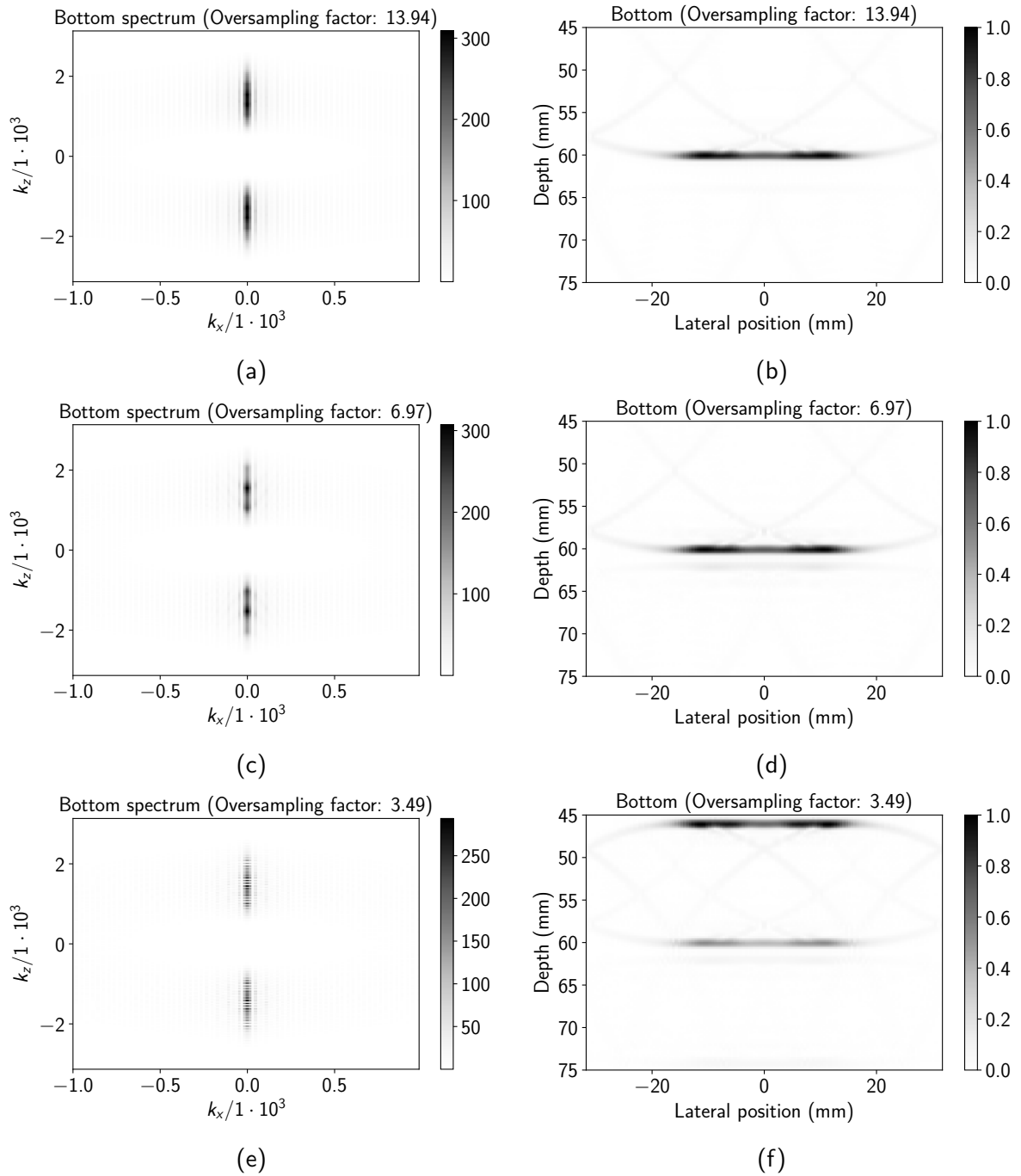


**Figure 56: Spectrum of the bottom reconstructed with (a) an oversampling factor of 13.94 and (b) reconstructed image, (c) an oversampling factor of 6.97 and (d) reconstructed image, (e) an oversampling factor of 3.49 and (f) reconstructed image.**

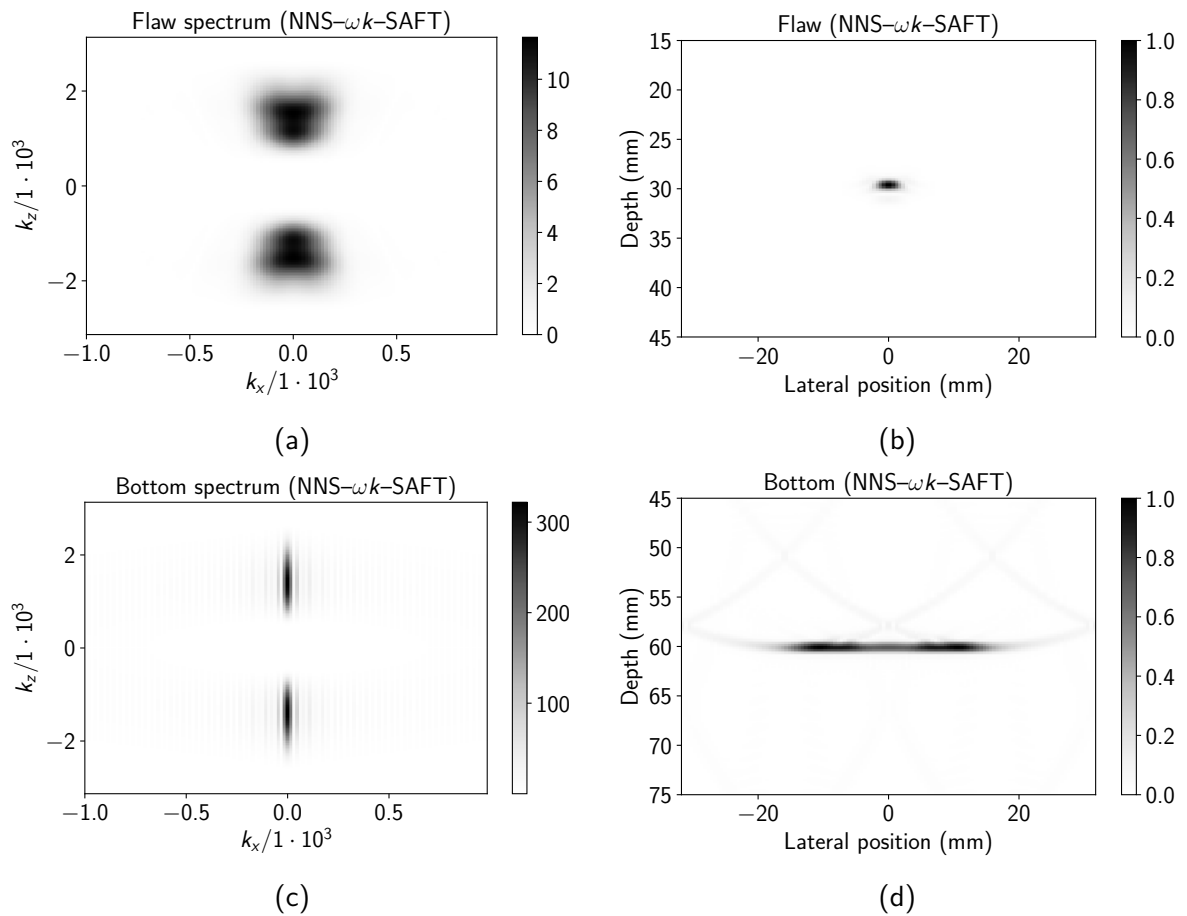


**Figure 57: (a) Magnitude of the reconstructed spectrum from A-scan signals containing a single flaw and (b) the resulting image, (c) magnitude of the reconstructed spectrum from A-scan signals containing only the bottom of the object and (d) the resulting image. The spectra were reconstructed with the NNS- $\omega k$ -SAFT algorithm.**